Anja Murud Gahre
Ragnhild Hembre Haug

Dynamic response of steel plates subjected to combined blast and impact loading

Master's thesis in Mechanical Engineering
Supervisor: Vegard Aune and Benjamin Stavnar Elveli
June 2020

Master's thesis

NTNU
Norwegian University of
Science and Technology

Anja Murud Gahre
Ragnhild Hembre Haug

Dynamic response of steel plates subjected to combined blast and impact loading

NTNU

Norwegian University of
Science and Technology

Department of Structural Engineering
Faculty of Engineering
NTNU – **Norwegian University of Science and Technology**

MASTER THESIS 2020

SUBJECT AREA:	DATE:	NO. OF PAGES:
Computational Mechanics	June 18th 2020	74

TITLE:

Dynamic response of steel plates subjected to combined blast and impact loading

Dynamisk respons av stålplater utsatt for kombinert støt- og eksplosjonslast

BY:

Anja Murud Gahre

Ragnhild Hembre Haug

SUMMARY:
This thesis investigates the behaviour of thin steel plates subjected to a combination of ballistic impact and blast loading. Both experimental and numerical studies were conducted. All plates had a thickness of 0.8 mm. Three different steel materials of various strength and ductility were examined. Tensile tests were performed on material specimens in order to obtain a constitutive relation. All experiments were conducted at the Structural Impact Laboratory (SIMLab), at the Department of Structural Engineering, Norwegian University of Science and Technology (NTNU). The ballistic experiments were conducted using the gas gun facility, while the blast loading was conducted in the SIMLab Shock Tube Facility (SSTF). APM2 bullets were used for ballistic perforation. The hole was imposed in the middle of the plate. Plates with pre-formed holes of the same dimensions as the cross-section of the projectiles were also subjected to blast loading. Two firing pressures were used. Additionally, blast loading experiments were performed on plates without holes of one steel grade, for five firing pressures.

Lagrangian simulations were conducted in LS-DYNA and compared to experimental observations for validation. The final part of the numerical work consisted of parametric studies on the fracture parameter and the strain rate sensitivity constant.

It was found that the crack propagation during blast loading was strongly dependent on the initial cracks and damage from ballistic impact. High strength and low ductility proved less resistant to blast loading after ballistic impact, compared to the more ductile, strain-hardening materials. Pre-existing damage from ballistic perforation was more detrimental to the plates' structural response than pre-formed holes. Numerical studies were able to predict the crack initiation to some degree, but the crack propagation was overestimated. As expected, simplifying the boundary conditions proved to reduce the deformations of the plates. However, this was found necessary as a compromise between accuracy and computational cost to be able to carry out the numerical studies with the computer resources available during this thesis.

RESPONSIBLE TEACHER: Vegard Aune

SUPERVISOR(S): Vegard Aune and PhDc Benjamin Stavnar Elveli

CARRIED OUT AT: Department of Structural Engineering, NTNU

Institutt for konstruksjonsteknikk
Fakultet for ingeniørvitenskap
NTNU – **Norges teknisk-naturvitenskapelige universitet**

MASTEROPPGAVE 2020

FAGOMRÅDE:	DATO:	ANTALL SIDER:
Beregningsmekanikk	18. juni 2020	74

TITTEL:

Dynamisk respons av stålplater utsatt for kombinert støt- og eksplosjonslast

Dynamic response of steel plates subjected to combined blast and impact loading

UTFØRT AV:

Anja Murud Gahre

Ragnhild Hembre Haug

SAMMENDRAG:
Denne oppgaven undersøker oppførselen til tynne stålplater, utsatt for en kombinasjon av støt- og eksplosjonslast. Både eksperimentelle og numeriske studier ble utført. Alle platene var av tykkelse 0.8 mm. Tre ulike stålkvaliteter med forskjellig styrke og duktilitet ble brukt. Strekktester ble utført på materialprøver for å etablere materialmodeller. Alle eksperimentene ble utført ved Structural Impact Laboratory (SIMLab), på institutt for konstruksjonsteknikk, Norges Teknisk-Naturvitenskapelige Universitet (NTNU). Ballistikk eksperimentene ble utført i gasskanonen, mens eksplosjonsforsøkene ble utført i SIMLab Shock Tube Facility (SSTF). AMP2 kuler ble brukt for ballistisk perforering. Kulehullet ble påført i midten av platen. Plater med forhåndsformede hull, med samme dimensjoner som tverrsnittet til prosjektilet, ble også utsatt for eksplosjonslast. To avfyringstrykk ble brukt. I tillegg ble eksplosjonslaster med fem intensiteter satt på plater uten hull for én stålkvalitet.

Lagrange-modeller ble brukt til numeriske studiet i LS-DYNA og sammenliknet med eksperimentelle observasjoner for validering. Den siste delen av det numeriske arbeidet innebar parameterstudier på bruddparameteren og parameteren for beskrivelse av materialers følsomhet for tøyningsrate.

Det ble funnet at bruddpropagering under eksplosjonslast var sterkt avhengig av den initielle sprekkdannelsen og skaden fra ballistisk perforering. Høy styrke og lav duktilitet ble funnet til å være mindre motstandsdyktig mot påfølgende eksplosjonslast sammenliknet med mer duktile, arbeidsherdende materialer. Allerede eksisterende skade fra prosjektilets perforering var mer destruktivt for platenes strukturelle respons enn boret hull. Numeriske studier var i stand til å forutsi bruddinitiering til en viss grad, men overdrev bruddpropageringen. Som forventet førte simplifiserte randbetingelser til mindre deformasjoner. Dette ble imidlertid funnet som et nødvendig kompromiss mellom nøyaktighet og beregningstid, slik at det skulle være mulig å gjennomføre de numeriske studiene med de tilgjengelige beregningsverktøyene i løpet av denne masteren.

FAGLÆRER: Vegard Aune

VEILEDER(E): Vegard Aune og PhDc Benjamin Stavnar Elveli

UTFØRT VED: Institutt for konstruksjonsteknikk, NTNU

Department of Structural Engineering
FACULTY OF ENGINEERING SCIENCE AND TECHNOLOGY
NTNU – Norwegian University of Science and Technology

MASTER'S THESIS 2020

for

Anja Murud Gahre and Ragnhild Hembre Haug

Dynamic response of steel plates subjected to combined blast and impact loading

1. INTRODUCTION

Protection of vital infrastructure against blast or impact loading has received a lot of attention in recent years. However, the literature is rather scarce when it comes to studies on the combined effect of blast and impact loading. This is often the case in real scenarios where hazardous fragments may be accelerated by the blast wave. It is known from experience that the combined effect of blast and fragment impact may be more severe than the effect of the blast or impact alone. Despite these observations, such loading scenarios are not covered by design codes and few studies are available in the open literature. Computational methods are now available to predict both the loading and structural response in these extreme loading situations, and experimental validation of such methods is necessary in the development of safe and cost-effective protective structures. In this study blast experiments will be performed on thin steel plates, and the data will be used for validation of some frequently used computational methods involving blast and impact loading.

2. OBJECTIVES

The main objective of the research project is to develop a better understanding of how thin steel plates behave under combined blast and impact loading, and to validate to which extent this can be predicted using computational tools. Special focus is placed on the influence of material properties and fragment penetration on the performance of blast-loaded plates.

3. A SHORT DESCRIPTION OF THE RESEARCH PROJECT

The main topics in the research project will be as follows;

1. A literature review should be conducted to understand the blast load phenomenon, the combined effect of blast and impact loading, constitutive and failure modeling of steel plates exposed to extreme loadings, and explicit finite element methods.
2. The steel plates are manufactured from cold-rolled sheets of type Docol 600DL, Docol 1000DP and Docol 1400M. Material tests will be carried out to obtain the mechanical properties of these materials and used to calibrate relevant constitutive relations.
3. Both ballistic tests and shock tube tests will be used to obtain combined blast and impact loading. The ballistic tests will be used to impact the plates with small-arms projectiles, before the same plates are exposed to blast loading in the shock tube. The shock tube tests will be used to investigate typical dynamic responses and failure modes of plates exposed to blast and impact loading.
4. Digital Image Correlation (DIC) and laser scanning will be used to measure the 3D transverse displacement fields of the plates in the experiments.
5. Non-linear FE numerical simulations of the ballistic and shock tube experiments will be performed, and the numerical results shall be compared and discussed based on the experimental findings.

Supervisors: Vegard Aune (NTNU), Benjamin Stavnar Elveli (NTNU)

The thesis must be written according to current requirements and submitted to the Department of Structural Engineering, NTNU, no later than June 11th, 2020.

NTNU, January 15th, 2020

Vegard Aune
Associate Professor

Abstract

This thesis investigates the behaviour of thin steel plates subjected to a combination of ballistic impact and blast loading. Both experimental and numerical studies were conducted. All plates had an exposed area of 300 mm x 300 mm and a thickness of 0.8 mm. Three different steel materials of various strength and ductility were examined. In order to obtain a constitutive relation, tensile tests were performed on specimens cut from 0°, 45° and 90° of the rolling direction of the plates. All experiments were conducted at the Structural Impact Laboratory (SIMLab), at the Department of Structural Engineering, Norwegian University of Science and Technology (NTNU). The ballistic experiments were conducted using the gas gun facility, while the blast loading was generated in the SIMLab Shock Tube Facility (SSTF). APM2 bullets were used for ballistic perforation. One configuration of ballistic impact was tested, where the hole was imposed in the middle of the plate. Plates with pre-formed holes of the same dimensions as the cross-section of the projectiles were also subjected to blast loading.

This enabled comparison of the dynamic response for plates with ballistic perforation and plates with machined holes when exposed to blast waves. Two firing pressures were used. Additionally, blast loading experiments were performed on plates without holes of one steel grade, for five firing pressures.

Uncoupled explicit non-linear finite element simulations were conducted in LS-DYNA. The loading was applied in two stages. After perforation of the projectile, the blast loading was applied using idealized pressure-time curves. Solid elements were chosen in an attempt to describe crack initiation and propagation. It was therefore found necessary to utilize symmetry and simplified boundary conditions to reduce computational time. The effect of modelling the plate with fixed sides, opposed to using a fully clamped assembly, was investigated for plates without holes. Then, the combination of impact and blast loading was modelled, and compared to experimental observations for validation. The final part of the numerical work consisted of parametric studies on the fracture parameter and the strain rate sensitivity constant.

It was found that the crack propagation during blast loading was strongly dependent on the initial cracks and damage from ballistic impact. High strength and low ductility proved less resistant to blast loading after ballistic impact, compared to the more ductile, strain-hardening materials. Pre-existing damage from ballistic perforation was more detrimental to the plates' structural response than pre-formed holes. Numerical studies were able to predict the crack initiation to some degree, but the crack propagation was overestimated. As expected, simplifying the boundary conditions proved to reduce the deformations of the plates. However, this was found necessary as a compromise between accuracy and computational cost to be able to carry out the numerical studies with the computer resources available during this thesis.
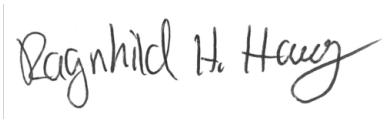
Acknowledgements

Trondheim, June 18th, 2020

Ragnhild Hembre Haug

Anja Murud Gahre

Contents

1 Introduction

1.1 Background and Motivation

The threat of accidents causing explosions is ever present in various industries such as oil, gas and other chemical production. Recent years have also seen an increasing trend of man-made and intentional acts of terrorism against urban environments. This has become a threat that needs to be taken into account. Globalisation and technical advances mean that information is easily spread and gathered. Instructions on the manufacturing of improvised explosive devices (IEDs) has become accessible to the public, and their mobility and huge potential for damage has led to an increase in attacks against civilians with explosives as the weapon of choice[1].

In a close-range explosion, the blast wave will likely be accompanied by fragments, which will impact the structure prior to, simultaneously or after the blast loading. This will depend on the distance between the target and the point of detonation. Fragments typically impact the target prior to the blast wave, when the distance between the target and the point of detonation increases within the close-range domain[2]. Bullets and artillery shells may also inflict preexisting damage to the structure. This might severely reduce the capacity of the construction as well as alter its structural response to the blast loading[3]. Despite this, the combined scenario of both impact and blast is often not included in design codes, with few studies openly available. Taking this combined effect into account makes the blast-resistant design challenging and complicated, compared to traditional protective designs focusing on either the impact or blast loading alone.

For design purposes or aesthetic reasons, the structures might also be perforated at the outset. Historically, massive, and hardened structures have been designed with protection against impact and blast loading. However, civilian structures are often lightweight and flexible, leaving them less protected. With the increased threat, the structural response for light-weight and flexible structures under extreme loading conditions with considerable deformations, has become an area of increased importance. Steel is often used in such structures because of its high strength and ductility at a relatively low cost.

Due to the increase in terrorist attacks, effective and reliable protection of critical civilian infrastructure has become an important issue[4]. The research in the field of blast and impact effects on structures has attracted a rise in interest in later years to understand the underlying physics more comprehensively. Given the complexity of the two fields alone, accounting for the combined effect of fragments and blast loading, the problem becomes highly complicated. Full-scale testing is rarely, if ever, a possibility. Numerical simulations could therefore be utilized to gain further insight and save costs. Experiments can be used to validate numerical models, for which reliability is of high importance in design.

1.2 Previous Work

As mentioned, the separate fields of impact and blast loading are active fields of research. Studies on combining these are fairly scarce in literature, however some work has been done on aluminium and steels plates with different designs of pre-formed holes and slits. The consideration

1

of combined impact and blast loading is however rather scarcer. Hald[5] started to examine the combined effects of ballistic impact and blast loading on steel plates in his master's thesis at SIMLab at NTNU in 2019.

A brief introduction to some of the previous work related to this thesis will be presented in the following. The studies presented are considered the most relevant for this thesis.

Pre-formed holes and slits can be imposed on structures to resemble the impact from fragments or projectiles preceding blast loading. Rakvåg et al.[6] used 0.7 mm thick Docol 600 steel plates with pre-formed holes as idealised perforations from impact loading. The plates were tested at two pressures and no failure was observed. It was pointed out that a perforation by a fragment will leave sharper cracks and greater damage than the pre-formed holes. The shape of the holes, as well as the size, was found to be significant for the deflection of the plates. Circular holes experienced the least plastic strains and loss of capacity. An increase in perforation area also led to a decrease in permanent deflection. Both Lagrangian and coupled numerical simulations in LS-DYNA were carried out. Results were in good agreement with the experimental observations but were not capable of predicting accurate deflections around the holes.

Pre-formed slits have also been applied to 1.5 mm aluminium plates by Granum et al.[7]. Blast loading was applied in the SSTF at NTNU. The slits were manufactured by wire erosion which resulted in a width of less than 1 mm. The material description was found by inverse modeling in Abaqus, and Explicit, uncoupled FEA in Abaqus/Explicit was able to capture the deformation and failure of the plate. A later article by the same authors investigated the effect of heat treating the aluminium and changing the numbers of slits alongside their orientations[8]. It was found that changing the slits changed the crack patterns and failure modes of the plates, impacting its capability to endure blast loading. Heat treatment affected the blast resistance of the plates, but not the failure modes. Heat treatment that provided high strength, but low ductility had a lower load bearing capacity than heat treatment that gave lower strength but higher ductility. A numerical study was also carried out here, with the same method seen in the previous study and was able to capture the experimental results accurately.

Aune et al.[9] examined the dynamic response of 0.8 mm Docol 600 steel plates with and without pre-formed slits. Using several firing pressures in the SSTF, the plates experienced a range of structural responses, from inelastic deformation to total failure at the supports. The influence of pre-formed holes on the dynamic response and failure aspects of the plates were given special consideration. Fluid-structure interaction (FSI) effects were investigated by comparing pressure histories in tests with rigid plates to those with flexible plates. In general, perforated plates experienced larger deformations compared to flexible plates without holes. Numerical simulations were conducted in EUROPLEXUS, where crack propagation was found to be recreated with a high level of accuracy. Plate deformations were overestimated numerically because of the uncoupled approach. It was also found that modelling the fully clamped boundary conditions was essential to replicate experimental results.

Kristiansen and Sigstad[10] studied the dynamic response of blast loaded Docol 1400 steel plates with and without pre-formed holes. The plates were blast loaded in the SSTF. Four different plate geometries were used, with the total area of the pre-formed holes kept constant. The deformable plates had a thickness of 0.8 mm, while the rigid plates were 3 mm thick. Structural response of the plates was compared to similar previously conducted studies on Docol 600, and

it was concluded that the increased strength did not compensate for lower work hardening and lower ductility in view of blast resistance. Lagrangian simulations were carried out in ABAQUS and EUROPLEXUS, and coupled Eulerian-Lagrangian were conducted in EUROPLEXUS. The numerically obtained displacements closely resembled those obtained experimentally. Predicting fracture accurately was found to be challenging, particularly for the plates with multiple holes. The coupled model and the computational fluid dynamics (CFD) model was found to describe the fluid sub-domain very accurately. It was seen, both experimentally and numerically, that the pressure built up on the perforated plates was unevenly distributed.

Hald[5] conducted experimental and numerical studies on 0.8 mm steel plates of type Docol 600 and Docol 1400 subjected to combined ballistic impact and blast loading. Plates with circular pre-formed holes were also studied numerically. Three different configurations for the ballistic impact were used, all subjected to the plates using APM2 bullets with initial velocities of around 900 m/s. The plates were then loaded by a blast wave in the SSTF. The initial cracking from the impact was found to further propagate in the blast experiments, suggesting that pre-existing damage is detrimental to the structural response in view of blast resistance. High ductility and strain hardening were also found to be preferred over high strength in view of blast resistance. Hald emphasized the complexity in describing the combined effect of ballistic impact and blast loading but was able to capture the behaviour to some extent in the numerical models in Abaqus. Overall, it was concluded that the combined effects of impact and blast loading cannot be ignored or simplified too greatly.

Elveli et al.[11] investigated the combined effects of ballistic impact and blast loading on steel plates for Docol 600 and Docol 1400. APM2 bullets were used whilst the plates were later exposed to blast loading in the SSTF. Numerical simulations were run in ABAQUS and compared with the experimental results. Special focus was placed on the effects of pre-damage from impact on the cracking of the plate during blast loading. It was found that crack propagation was strongly dependent on existing crack initiation and damage. Lower ductility and higher strength proved less resistant to the blast wave. The numerical results were found to be in good agreement with the experimental discoveries.

Osnes et al.[12] carried out studies on laminated glass subjected to impact and blast loading. Experiments were conducted on plates without any damage, with pre-drilled holes and holes from the impact of a 7.62 mm APM2 bullet. It was found that the damage to the interlayer was severely increased with the amount of pre-imposed damage. Upon the arrival of an incoming blast wave the interlayer may rupture completely, allowing the pressure and fragments to enter the building. The glass also broke into larger pieces of fragments when pre-damaged, imposing an enlarged threat to the people around. Therefore, it is highly recommended to consider fragment impact in the design of blast-protecting windows.

Kong et al.[13] investigated the response of a multi-layer protective structure when subjected to the fragments and pressure wave from an exploding metal casing filled with TNT charge (MCTC). Stiffened thin plates, as used in the study, can be damaged dramatically from impacting fragments. For a thick structure, such as concrete walls, the localised damage from impacting fragments does not alter the global response during blast loading to the same degree as for a thin structure. Perforations on the stiffened plates acted as a mean of crack initiation, which connected with each other when subjected to blast loading. The experimental results from the

study showed acceptable agreement with the numerical simulations in ANSYS Autodyn and several design suggestions were made.

Del Linz et al. [14] performed an experimental and numerical study on reinforced concrete slabs of varying thickness between 100-200 mm. The slabs were impacted by an explosion at a stand-off distance of 2.1 m triggered by approximately 9 kg of TNT, with steel ball bearings replicating shrapnel loading. Numerical models were created using LS-DYNA. A maximum crater depth of 25 mm was observed in addition to some cracks connecting the craters. This was indicated to be superficial and the specimens would still hold sufficient capacity. Agreement between numerical and experimental results varied for each test, but the penetration depth and the level of damage around impact were found to be realistic for the numerical predictions.

1.3 Thesis Outline

This thesis will be a continuation of the work by Hald[5], investigating the dynamic response of thin steel plates subjected to ballistic impact prior to the blast loading. The experiments will be performed on steel plates of 0.8 mm thickness. Three different steels will be used, to vary both the material strength and ductility. Half of the plates are first shot with a rifle in the gas gun facility at SIMLab at NTNU, to create a hole in the centre of the plates. The other half have pre-formed holes with a similar diameter as the diameter of the projectile's cross-section. After the ballistic tests, the plates undergo the same blast loading in the SSTF. As a result of the separate loading steps, it is possible to address the response of the plates, including failure modes and crack initiation before the blast loading. Special focus will therefore be placed on the influence of projectile penetration and material properties on the performance of blast loaded plates. In addition, blast experiments are performed on plates without holes but of the same dimensions. Material tests will be conducted to obtain the mechanical properties of the steels under consideration and used for calibration of constitutive models. These models will be input in non-linear finite element simulations of the ballistic impact and blast loading of the plates in LS-DYNA. The objective will be to validate to what extent the loading scenarios can be predicted using computational tools. Provided that the numerical models predict reliable results, these models will also be used to obtain a better insight into the blast resistance of the plates.

2 Material Testing

This section presents the material tests for Docol 600 DL (D600), Docol 1000 DP (D1000) and Docol 1400 M (D1400). The purpose of the material tests was to define each material in terms of its mechanical properties and then calibrate the material models. The tests would provide characterisation of the materials, as well as the basis of the material modelling in the computational analysis of the component tests.

2.1 Materials

The three different steels were all manufactured by Swedish Steel Ltd (SSAB) and are commonly used in automotive industry. Docol 600 DL and Docol 1000 DP are dual phase steels, while Docol 1400 M is a martensitic steel. All three steels were cold rolled and annealed. Cold rolling is a process where a sheet of steel is further compressed into the desired thickness and shape at lower temperatures ranging typically between 60 °C and 180 °C[15].

As steel hardens after cold rolling due to plastic hardening, it is common to anneal the material to soften it. Annealing is a heat treatment of the material, where it is heated and kept at a high temperature for a preferred time before it is subsequently cooled down[16]. The manufacturer provides the following mechanical properties of the steel grades in Table 2.1.

Table 2.1: Typical values of the mechanical properties from the manufacturer's data sheet.[17] [18].

Steel grade	Yield Strength Range [MPa]	Tensile Strength Range [MPa]	Minimum Elongation [%]
Docol 600 DL	280-360	600-700	20
Docol 1000 DP	700-950	1000-1200	7
Docol 1400 M	1150-	1500-1700	3

2.2 Uniaxial Tension Tests

All tests were conducted on specimens cut from the cold rolled 0.8 mm sheets used in this thesis. The test specimens were flat dog-bone samples with the geometry shown in Figure 2.1a. The strain gauge area had a length of 70 mm and a width of 12.5 mm.
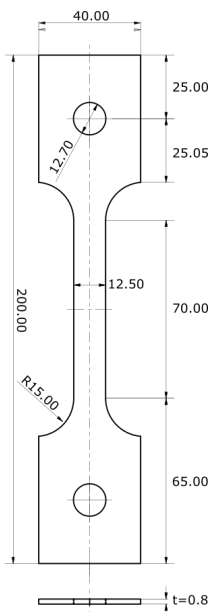
(a) Geometry of the dog-bone specimen.   **(b)** Experimental set up of the tensile tests.

Figure 2.1

Each material was tested 3 times in 3 directions; 0°, 45° and 90° relative to the rolling direction of the sheet. This made a total of 27 tests, where each specimen's width and thickness were measured at 3 different places at the strain gauge area. The same order was used so that the measurement of the thickness, t_1, was measured on the same place as the width, w_1, and so on. The measurements were conducted with the micrometre, Micromar 40 EW, shown in Figure 2.1b. Its error limit is 4 µm and the resolution is 0.001 mm [19]. These measurements are listed in Table .1 in Appendix A.

The tensile tests were preformed with a Zwick/Roell Z030 tensile machine at a loading rate of 2.1 mm/min, resulting in an equivalent strain rate of $5 \cdot 10^{-4} \text{s}^{-1}$. The equivalent strain rate was found using Equation (1).

$$\dot{\epsilon} = \frac{v(t)}{L_0}, \tag{1}$$

where $\dot{\epsilon}$ is the strain rate, $v(t)$ is the velocity in mm/s, and the initial strain gauge length, L_0, is 70 mm. This strain rate ensured that it was a quasi-static test. In the quasi-static domain, the load duration is far longer than the time the structure takes to respond to the load. Consequently, the structural response is only dependent on the structure's stiffness and the peak load [20].

The specimen was horizontally fixed and held in place with a bolted connection through the two holes of the specimen. In addition, there were shims on each side of the specimen to clamp it tight and avoid local buckling in the vicinity of the bolt holes. The importance of the shims was verified in test D600_0_3 which was run without shims, resulting in local buckling around the bolt hole. Because some of the test specimens of the D1400 material were slightly warped, all tests were pre-tensioned at 100 N to straighten out the specimen before applying the load. The tensile machine measured the loads with its load cell at 2 Hz. Furthermore, the tests were all painted with a speckle pattern that allowed for two-dimensional digital image correlation (2D-DIC), which will be discussed in the following section.

2.3   Two-Dimensional Digital Image Correlation (2D-DIC)

Digital image correlation (DIC) is an optical method for measuring movement in a specimen through the use of a camera taking images during the test. A DIC post-processing software is then needed to track blocks of pixels from the resulting images. To enable the software to find and successfully trace these blocks without aliasing, it is important that the specimen's surface is random and unique, which is why a speckle pattern is painted on the surface of each specimen [21].

An in-house DIC software, called eCorr, was used for post-processing [22]. When creating a mesh that will track the deformation pattern to create a deformation field, a suitable mesh and mesh size must be selected. In this thesis, only Q4 elements were used. Large elements are CPU efficient and less susceptible to gray-scale noise, but small elements give a better description of the displacement field. Gray-scale noise is the main source of error in the DIC and varies from camera to camera. For displacements the typical resolution is 0.1 pixels. The strain resolution is as low as 10^{-4}, and it is possible to measure strains of up to 200 % [22]. For 2D-DIC only one camera is required, and it is important that it points straight at the specimen, and that the surface is

plane.

Figure 2.2 shows the set up in eCorr for extracting strains. A vector of initial length of 60 mm acted as a virtual extensometer, tracking the elongated length for each frame. In order to obtain the pixels/mm relation, a vector was placed over the width in the middle of the specimen. As the length in mm was known, the pixels/mm relation was calculated. The corresponding load data was obtained directly from the load cells. Post-processing these data sets gave the change in length, ΔL, and corresponding load data for all 27 tests. This was used to calculate the engineering strains and stresses up to the point of diffuse necking.
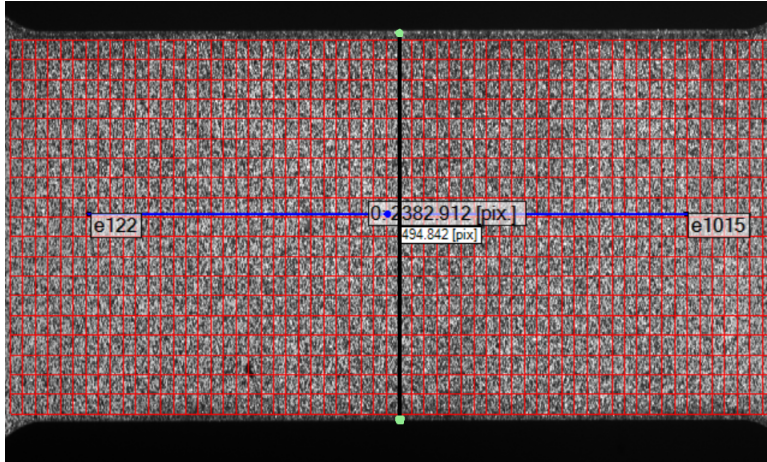
Figure 2.2: Picture of the mesh of the dog bone test with the extensometer vector and vector for obtaining pixels/mm relation. The extensometer is blue, whilst the vector is black with green dots at the ends.

The engineering strains and stresses were calculated using the following expressions

$$S = \frac{F}{A_s} \quad \text{and} \quad e = \frac{\Delta L}{L_0} \tag{2}$$

F is the load, A_s is the cross sectional area at the beginning of the test, ΔL is the change of length of the extensometer and L_0 is the initial length of the extensometer.

2.4 Results

Post-processing the experimental data from the tension tests using 2D-DIC produced the plots in Figure 2.3. The plots and post-processing were made with the code in Listing 4 in Appendix B.
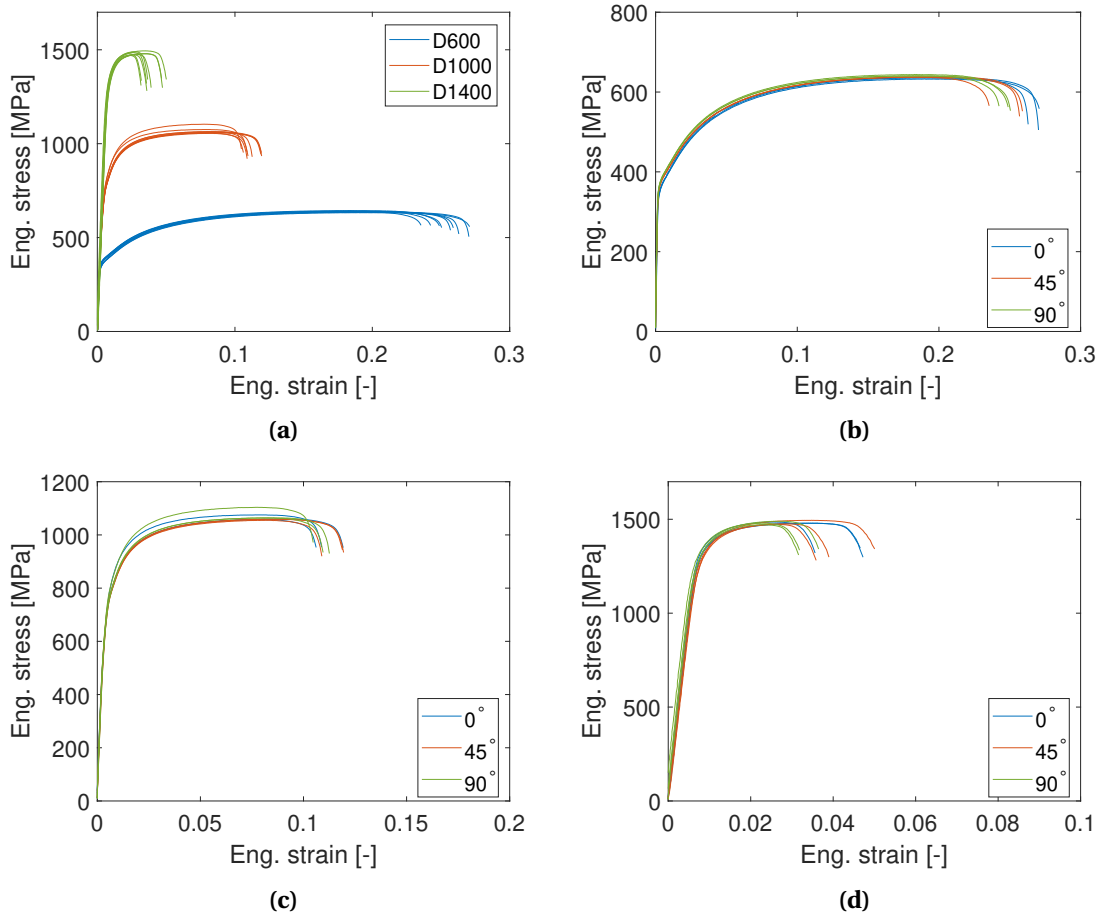
Figure 2.3: Engineering stress-strain curves for all uniaxial tensile tests: (a) all tests, (b) D600, (c) D1000 and (d) D1400.

The difference in stress level and elongation to fracture can be observed from Figure 2.3a for the three different materials when undergoing quasi-static testing. There seemed to be minor differences in strength related to rolling direction, except for two tests in the D1000 series. This indicates that an assumption of isotropic behaviour is valid. However, all materials show some deviation in elongation to fracture. The elongation varied both within the samples with same orientations and between samples with different orientations, most evidently for D1000 and D1400. The rolling direction seemed to be the most ductile for D600, followed by 45° and 90° to the rolling direction.

Studies on Docol 600 and Docol 1400 were conducted by Gruben et al. [23] on 1.0 mm and 1.8 mm thick plates, and tests on Docol 600 were performed by Rakvåg et al. [6] on 0.7 mm plates and by Holmen et al. [24] on 0.8 mm plates. Kristiansen and Sigstad [10] studied Docol 1400 plates of 0.8 mm thickness. These studies found that the steels generally exhibit satisfactory isotropic behaviour. Anisotropy is therefore considered beyond the scope of this thesis.

Hald [5] concluded that the strain hardening of D600 is significantly higher than that of D1400, due to the ferrite in the dual-phase steel. The strain to fracture was considerably lower for D1400 than D600, as D600 is a more ductile material. The results from the material tests support these

8

observations. Due to its composition and reported properties in Section 2.1, the material D1000 was expected to lie in between the two other steel qualities in strength and ductility. The experiments confirm this with respect to both yield strength and strain to fracture.

3   Material Model

3.1   Model Assumptions

The steels are expected to behave as elastic-thermoviscoplastic materials. This means that the steels will experience small elastic strains as well as strain and strain-rate hardening and thermal softening in the plastic domain. It is expected that the material will undergo large plastic deformations due to the blast loading, mainly failing as a result of ductile fracture. The Cockcroft-Latham (C-L) fracture criterion will be used to model fracture. The transition from idealised elastic to plastic behaviour is assumed to be governed by the Hershey high-exponent yield criterion. To describe the hardening and softening of the material it is assumed that these can be expressed explicitly as a function of strain, strain-rate, and temperature. The assumption of thermoviscoplasticity is assumed to be valid due to the relatively small elastic strains compared to the plastic strains[25]. Even though cold rolled metal sheets can exhibit anisotropy, the material is assumed to be isotropic in both the elastic and plastic domain, as discussed in Section 2.4.

3.2   Constitutive Model

The modified Johnson-Cook material model (MJC) was used to describe the behaviour of the materials. The equivalent stress is given as

$$\sigma_{eq} = (\sigma_0 + R(p))(1 + \dot{p}^*)^c (1 - (T^*)^m) \tag{3}$$

To establish this relation, a yield criterion, work hardening, thermal softening and strain rate dependency had to be determined. Then, all the contributions could be combined to obtain Equation (3). The yield function is given by

$$f = \varphi(\sigma) - \sigma_Y \leq 0 \tag{4a}$$

$$\varphi(\sigma) = \sqrt[a]{\frac{1}{2}((\sigma_I - \sigma_{II})^a + (\sigma_{II} - \sigma_{III})^a + (\sigma_I - \sigma_{III})^a)} \tag{4b}$$

where $\sigma_{eq} = \varphi(\sigma)$ is the equivalent stress and σ_Y is the flow stress. The principal stresses (σ_I, σ_{II} and σ_{III}) are defined in descending order whilst the parameter a controls the shape of the yield surface. The Hershey high-exponent yield criterion[26] is a generalised isotropic and pressure independent criterion, and is obtained by setting $a = 6$. Logan and Hosford[27] found this to give a good approximation for body-centred cubic materials.

The two most commonly used hardening laws are the Power law and the Voce rule, which are given respectively as

$$R(p) = Bp^n \quad \text{and} \quad R(p) = \sum_{i=1}^{n} Q_i(1 - \exp(-C_i p)) \tag{5}$$

where B, Q_i and C_i are calibrated values and p is the plastic strain. For this thesis, a three term Voce rule was chosen, as one term and two term Voce were found to be insufficient to obtain an accurate representation of the hardening curve.

As mentioned in Section 3.1, the material behaviour will also be dependent on viscoplasticity or, in other words, strain rate sensitive. The yield surface is expanded to include a strain rate dependent stress term σ_v, which represents the viscous stress. This gives

$$f(\sigma_{ij}) = \varphi_{ij} - \sigma_{eq} \quad \text{and} \quad \sigma_{eq} = \sigma_0 + R(p) + \sigma_v(\dot{p}^*), \tag{6}$$

which indicates that the stress is allowed to move outside the yield surface. Thus, the following needs to be introduced:

$$f \leq 0 \Rightarrow elastic \tag{7}$$

$$f > 0 \Rightarrow plastic \tag{8}$$

Equations (7) and (8) imply that the material behaves elastically when the yield function is less than or equal to zero and plastically above zero. The yield function can then be written as

$$\sigma_{eq} = (\sigma_0 + R(p))(1 + \dot{p}^*)^c \tag{9}$$

The dimensionless plastic strain rate can be expressed as

$$\dot{p}^* = \frac{\dot{p}}{\dot{p}_0} \tag{10}$$

where $\dot{p}_0$ is the reference strain rate.

To account for thermal softening of the material, $(T^*)^m$ was introduced into the constitutive equation, where

$$T^* = \frac{T - T_0}{T_m - T_0} \tag{11}$$

and m can be calibrated from tension tests. However, this parameter was taken from the literature in this thesis [23]. T is the temperature, T_0 is the ambient temperature, and T_m is the melting temperature. For further reading on thermal softening, the reader is referred to Aune [28].

The Voce hardening terms will be calibrated based on the quasi-static material tests, using the true strain, ε, true stress, σ_t and true plastic strain, p, up to the point of diffuse necking. The expressions are given by [23]

$$\varepsilon = s(1 + e) \quad \text{and} \quad \sigma_t = \ln(1 + e) \quad \text{and} \quad p = \varepsilon - \frac{\sigma_t}{E} \tag{12}$$

where s is the engineering stress and e is the engineering strain.

3.3 Failure Criterion

For a complete material model, a failure criterion must be included to describe the degradation of the material. Cockcroft and Latham[29] (C-L) proposed a simple failure criterion based on plastic work per unit volume. The equation is given as

$$D = \frac{W}{W_c} = \frac{1}{W_c} \int_0^p < \sigma_I > dp, \tag{13}$$

where σ_I is the major principal stress, D is the accumulated damage, p is the equivalent plastic strain and W_c is the amount of work the material will have experienced at fracture. Failure is assumed to occur when $D = 1$. The criterion is convenient in its simplicity, as only one damage parameter, which is obtained from a uniaxial tension test, is required for calibration. Dey et al.[30] showed that the one-parameter C-L criterion performed equally well as the five parameter Johnson-Cook fracture criterion in an LS-DYNA simulation on perforation of steel plates. The robustness of the C-L criterion is also proved for blast loaded panels[28] [31]. Further reading on the criterion can be found in e.g Børvik et al.[32] and Kane et al.[33].

3.4 Material Parameter Identification

In order to calibrate the material parameters, one sample of each material was chosen. The samples were deemed representative for both the work hardening and the range of elongation where initiation of necking occurred for the tests. The most extreme values on either side were avoided. D600: 0° test 1, D1000: 45° test 1 and D1400: 45° test 2 were used for the calibration.

The true plastic strain and stress data from the experiments, up until necking, were fitted to the Voce hardening rule in Equation (3). This was conducted using the curve fit tool in MATLAB which uses a least square fit. In addition, a point at high plastic strain was added to the data. This was done five times for the same value of plastic strain but with five different stress values. An example of the fitted curves is given for D1000 in Figure 3.1. This worked as additional constraints on the curve fit, in an attempt to estimate localised necking at the same strain as in the experimental test. The curve fit corresponding to the most accurate prediction of localised necking was used, as long as the fit also represented the hardening accurately. As mentioned, three term Voce was required to achieve sufficient accuracy. The material parameters from the fit were used as input for the quasi-static simulation of the dog-bone specimen in LS-DYNA. Figure 3.2 shows the geometry of the specimen and the data extraction points.
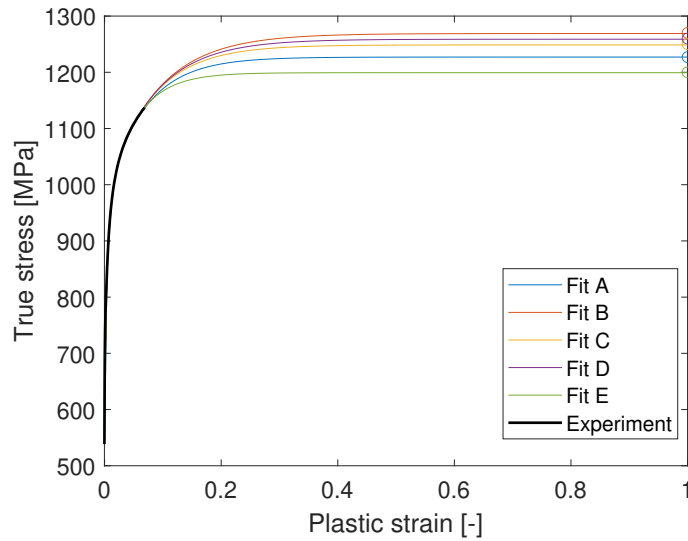
Figure 3.1: D1000: True plastic strain up until necking with 5 manually added points at the end to constrain the last part of the fit.
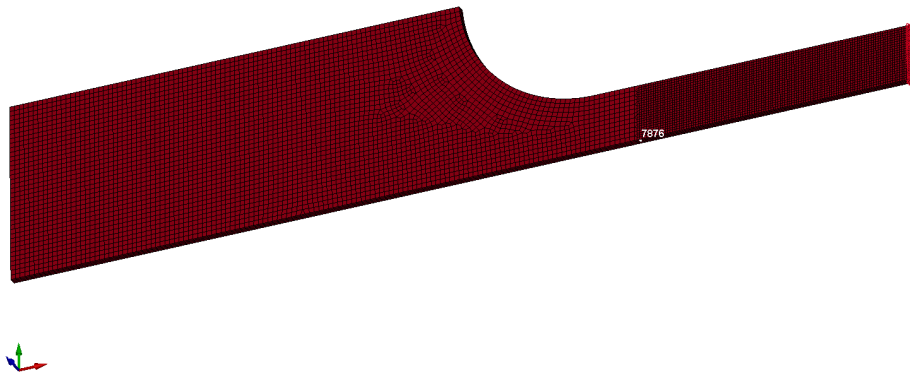
Figure 3.2: The model of the dog bone specimen in LS-DYNA. The node with number 7876 was used for the extraction of the displacement data. The set of nodes marked in red was used for extraction of force data. This model had an element size of 0.267 mm.

The force and displacement data were then processed to plot the engineering stress-strain curves from the numerical simulations. The calibration process resulted in the material parameters presented in Table 3.2, which provided the best fit up to fracture. Material parameters were calibrated based on the mesh size in Figure 3.2, which corresponded to three elements over the thickness.

The material constant c can be calibrated by conducting material tests at different strain rates,

but was for the purpose of this thesis taken from literature for Docol 600 and Docol 1400 [23]. The c-value for Docol 1000 was chosen as the mean value of D600 and D1400, with its validity being discussed in Section 5.4. The material constants taken from the literature are presented in Table 3.1. The calibrated hardening terms and other material parameters are shown in Table 3.2.

Table 3.1: Material constants taken from literature [23].

E	ν	ρ	c_p	χ	T_r	T_m
[GPa]	[-]	[kg/m^3]	[J/kgK]	[-]	[K]	[K]
210.0	0.3	7850	452	0.9	293	1800

Table 3.2: Model parameters for the modified Johnson-Cook model for Docol 600, Docol 1000 and Docol 1400.

Material	A	Q_1	C_1	Q_2	C_2	Q_3	C_3	a	c	m	$\dot{p}_0$
	[MPa]	[MPa]	[-]	[MPa]	[-]	[MPa]	[-]	[-]	[-]	[-]	[s^{-1}]
D600	338.8	102.9	51.6	205.0	19.0	2268.9	0.315	6	0.01	1	$5.0 \cdot 10^{-4}$
D1000	540.4	164.5	1963.1	259.5	147.1	256.4	16.1	6	0.007	1	$5.0 \cdot 10^{-4}$
D1400	1023.0	165.6	5010.4	165.6	480.1	178.1	122.8	6	0.004	1	$5.0 \cdot 10^{-4}$
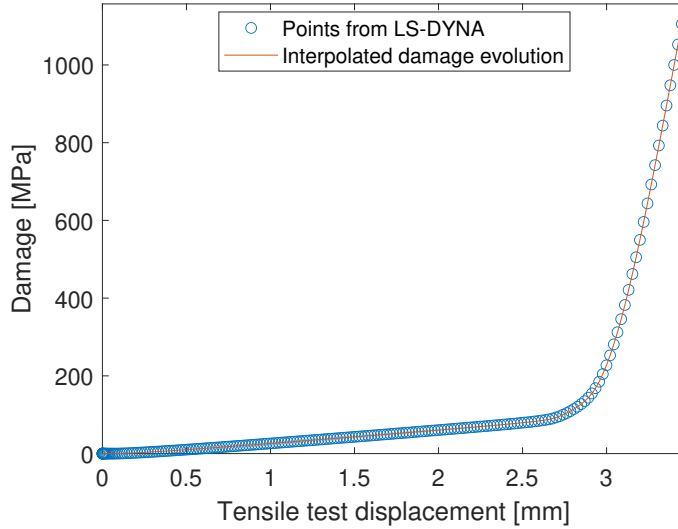
Figure 3.3: Linear interpolation of damage data from LS-DYNA over the simulation time. The blue circles represent the data from LS-DYNA, while the orange line represents the interpolated points between the LS-DYNA data points.

The fracture parameter W_c was extracted from the element exposed to the largest damage in the simulations of the tensile tests in LS-DYNA. The values between these points were obtained with linear interpolation, using 200 points in time as shown in Figure 3.3. To find the fracture parameter, it was decided to investigate fracture at the same elongation and the same stress level as fracture in the experiment. The damage was then extracted at the corresponding point in time from the simulations. Figure 3.4a illustrates the stress-strain curve from the simulation, without

fracture. The extracted fracture parameters are marked on the damage curve as red circles for strain and blue squares for stress. There is a large difference between these two fracture parameters as the increment in damage is exponential. The resulting stress-strain curves for the two simulations with different values of W_c for the D1000 tensile test are presented in Figure 3.4b.
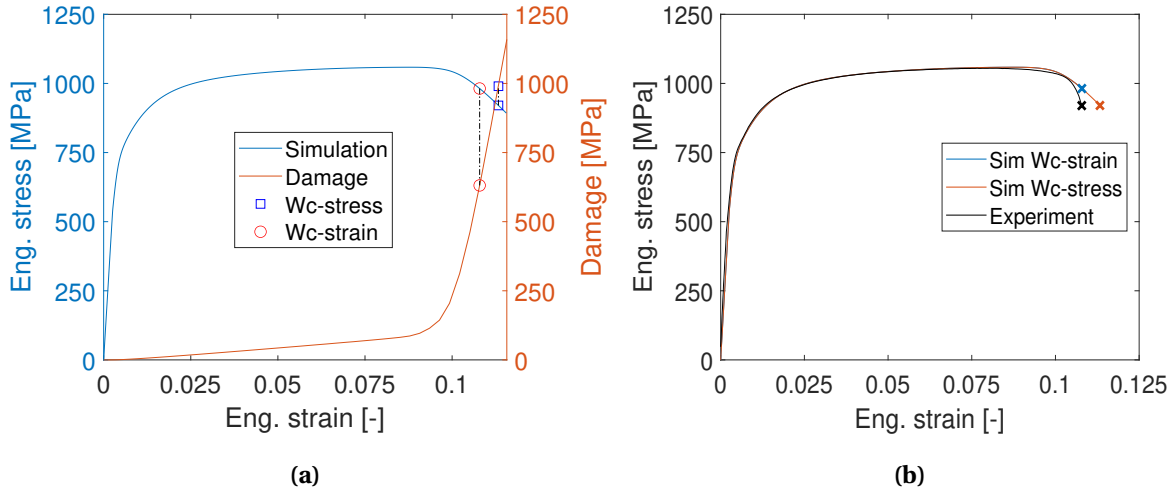
Figure 3.4: Properties of the damage parameter: (a) shows the engineering stress-strain curve and the development of the Cockcroft-Latham parameter W_c over time. The blue squares represent choosing the parameter at the same stress level as the failure of the experiment, whilst the red circles represent choosing the parameter at the same strain as the experiment. (b) shows the resulting engineering stress-strain curves of the uniaxial tests with the two different values of W_c in blue and orange. The experimental data can be seen in black. The point of fracture is marked an ×.

The W_c parameter was taken from the time corresponding to the elongation to fracture in the experiment. The sudden fracture resulted in a total strain and necking most resembling the experiment. Therefore, the fracture strain was used to calibrate the W_c parameter for all the materials. The values are shown in Table 3.3 for a mesh with three elements over the thickness.

Table 3.3: C-L fracture parameters W_c found using inverse modelling of the quasi-static material tests in LS-DYNA.

Material	W_c [MPa]
D600	565
D1000	631
D1400	487

Figure 3.5 shows that the stress-strain curve of the simulation of each material lies within the range of the experimental tests. This built confidence that the material parameters are representative for the material behaviour. It is worth noting that the fracture parameter is, in addition to being highly mesh sensitive, greatly affected by the extraction point. Therefore, a small variation in fracture strain will cause a large variation in the C-L parameter. This is clearly shown in Figure 3.4a as the parameter skyrockets after initialisation of necking.
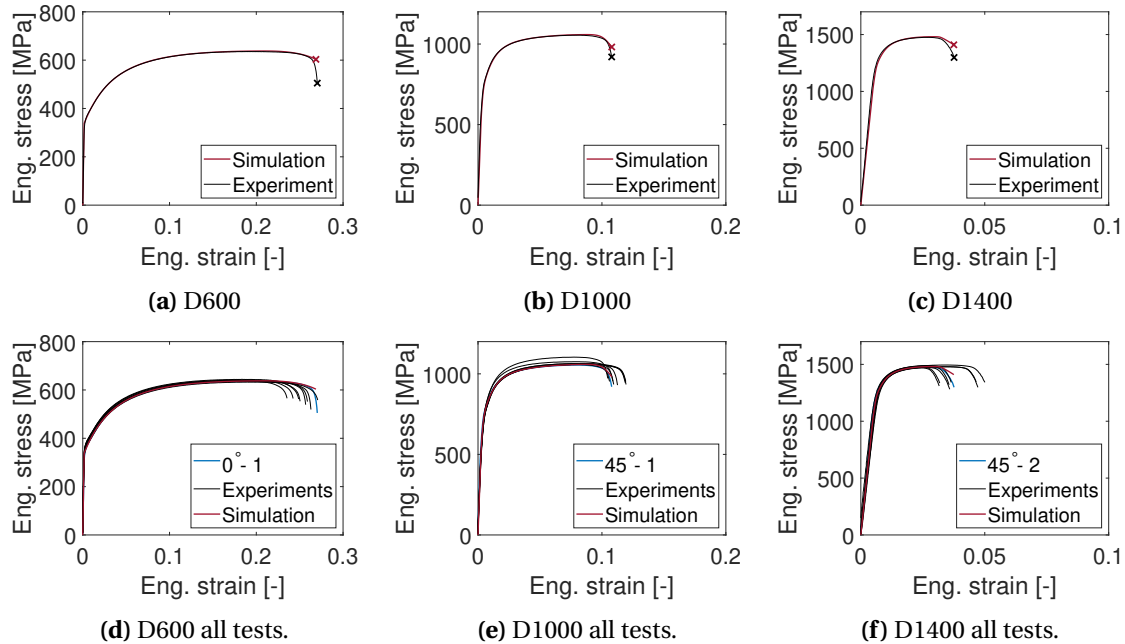
Figure 3.5: Comparison of the experimental stress-strain curve with the numerical simulation of the tensile test in LS-DYNA: (a), (b) and (c) illustrates how well the computational results compare to the experimental results, while (d), (e) and (f) shows all the experimental tensile tests. The chosen test for finding material parameters is marked in green for each material and the simulations are also shown to be within the range of all the experimental tests.

4   Experimental Tests

4.1   Ballistic Impact

The aim of the ballistic tests was to create holes of similar diameters as those on the plates with pre-cut circular holes. Moreover, due to the projectile perforation, these plates will have pre-existing damage when exposed to blast loading.

4.1.1   Experimental Setup

The experiments were conducted in the SIMLab gas gun facility at the Department of Structural Engineering at NTNU. The set-up of the test rig and the details of the 7.62 mm armor piercing bullets (APM2) are shown in Figure 4.1. Instead of firing from the gas gun itself, the bullets were fired from a smooth bore Mouser rifle mounted in the rig. For further information on the set up and attributes of the bullets, the reader is referred to Børvik et al [32].

The rifle was fixed in position for all the tests, therefore the desired point of impact was obtained by manually moving the steel plates. The position of the midpoint in the plates was also manually obtained by utilising the bolt holes corresponding to the clamping assembly. The plates are of dimensions 625 mm x 625 mm x 0.8 mm. The geometry of the plates can be seen in Figure
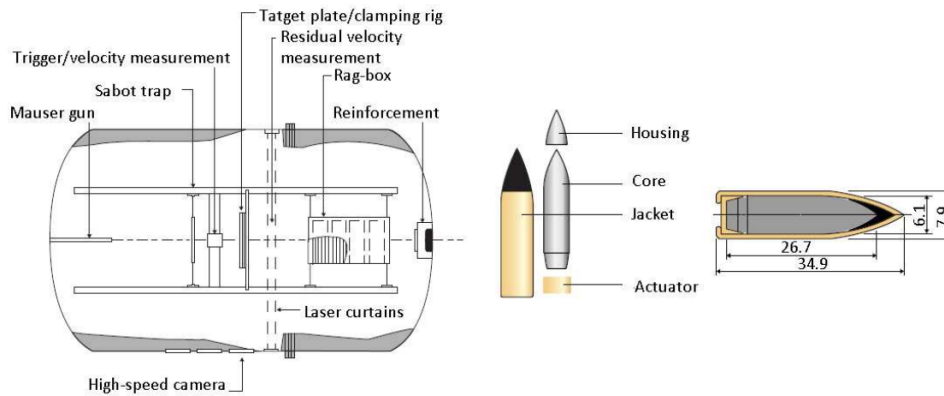
Figure 4.1: The experimental set up in the ballistic rig (left) and the dimensions and composition of the APM2 projectile (right). Dimensions are in mm [32].

4.2.
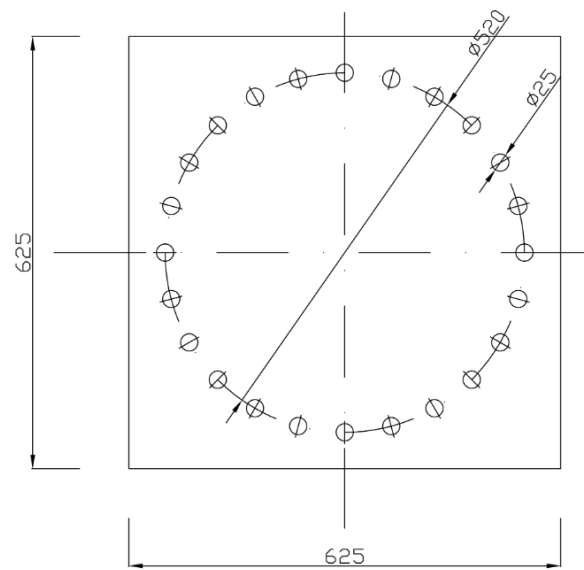
Figure 4.2: Machine drawing of the geometry of the steel plates used in the ballistic tests.

The experiments were filmed using Phantom v2511 high speed cameras which allowed for measurements of the initial and residual velocities of the projectiles, as well as providing high resolution pictures of the impact.

In total, nine plates were fired upon by a single shot in the centre. Three plates of each of the three materials used in this thesis were fired upon with a firing velocity just above 900 m/s to ensure that the damage is restricted to local damage of the plate around the hole, and limiting the global deformation. Consequently, compared to the plates with pre-cut circular holes, the plates of this configuration also contained some initial cracks and local damage.

16

4.1.2 Experimental Results

The results from the ballistic impact tests are presented as images of the perforation events, as well as a table of the initial and residual velocities of the projectiles denoted v_i and v_r respectively. In addition, pictures of the perforation holes from the front and back are given for one test of each material.

Table 4.1 shows the initial and residual velocities of the projectile for all the nine tests. The difference between the residual and initial velocities is also included in the table. It can be observed that this difference is relatively small, in the range of 1-2 %. The small differences in initial and residual velocities indicate that global deformations are negligible. This is an important assumption for this thesis as the purpose is to investigate the dynamic response of plates with holes caused by ballistic impact and pre-formed holes for different materials when exposed to blast loading.

Table 4.1: Initial and residual velocities of projectiles.

Material	Test	v_i	v_r	Difference
		m/s	m/s	%
D600	1	916.9	902.6	1.56
	2	915.9	902.1	1.51
	3	926.9	913.6	1.43
D1000	1	910.3	894.1	1.78
	2	928.7	913.6	1.63
	3	916.9	899.6	1.89
D1000	1	928.5	912.0	1.78
	2	918.6	903.7	1.62
	3	931.8	918.6	1.42

Pictures from the front and back of the perforation holes for one test of each material are presented in Figure 4.3. Figures showing all the tests can be seen in Appendix C. The figures are sorted by material, i.e., in the order D600, D1000 and D1400.

(a) D600 front   **(b)** D1000 front   **(c)** D1400 front

(d) D600 back   **(e)** D1000 back   **(f)** D1400 back

(g) D600 back   **(h)** D1000 back   **(i)** D1400 back
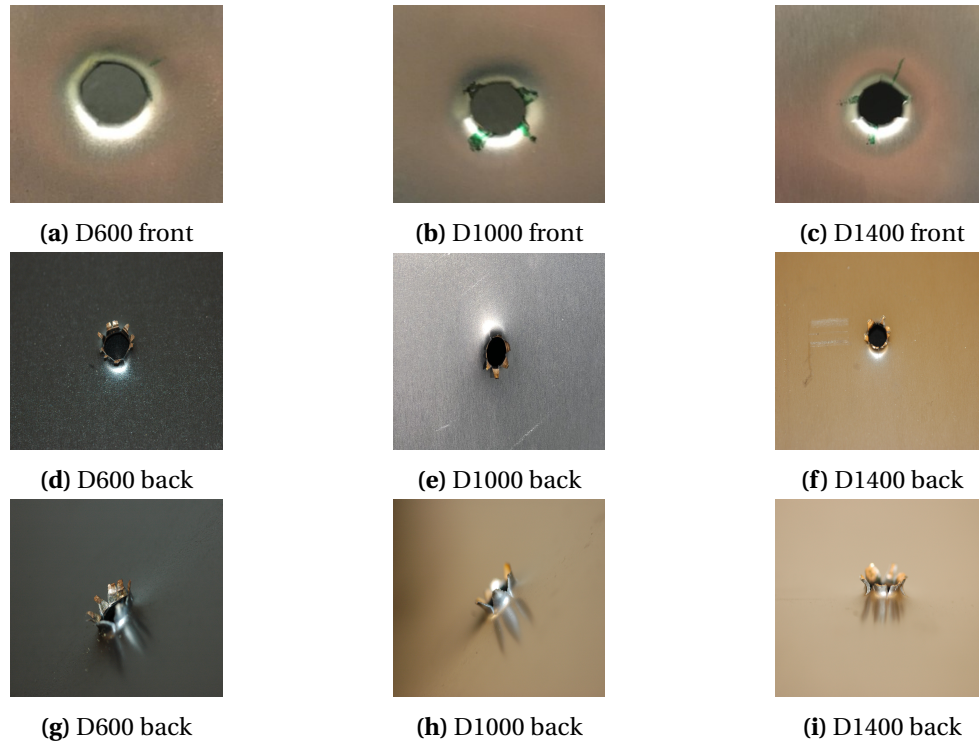
Figure 4.3: Resulting fractures of the plates after ballistic impact.

The dominant failure mode of all the materials was petalling. Petalling occurs when the plate material is pushed ahead of the projectile tip, deforming the material in a bulge at the back of the plate. The tensile strength of the material will eventually be exceeded and a star-shaped crack is formed. As the projectile continues its movement, the sectors are being pushed back, forming petals as so to allow the projectile to pass through. This failure mode is typical for thin, ductile steel plates[34].

It is observed that D1400 experienced more prominent cracking at the base of the petals than D600. This might be because D1400 is characterized by high strength and less ductility. Furthermore, it appears that D600 received slightly more local deformation than D1000 and D1400. The response of D1000 resembles that of D1400, but with somewhat less cracking at the base of the petals.

The majority of the projectiles were observed to have no significant pitch or jaw prior to impact. The perforation process was similar within all the experiments. An exception is D1000-3, for which the resulting petals have a slightly different shape than any of the other perforation tests. This can be seen in Figure .2, which is included in Appendix C. This could be due to the projectile having a minor pitch or jaw at impact. Hald[5] found that projectiles impacting with a pitch peels off a part of the plate whilst passing through the material. This test was not used for the blast experiments. A time-lapse of the perforation event for the six plates, that would later be used for the blast experiments in the shock tube, is shown in Figure 4.4. The projectiles impacting D1400 seem to have a slight pitch, but this appears to have a negligible effect on the petal formations. The figure can be seen in Figure .3 in Appendix C. D600 received slightly more local deformation than D1000 and D1400, which could be due to it being more ductile and therefore allowing more

deformation before the tensile strength is overcome.

(a) D600-1   **(b)** D1000-1   **(c)** D1400-2

(d) D600-2   **(e)** D1000-2   **(f)** D1400-3
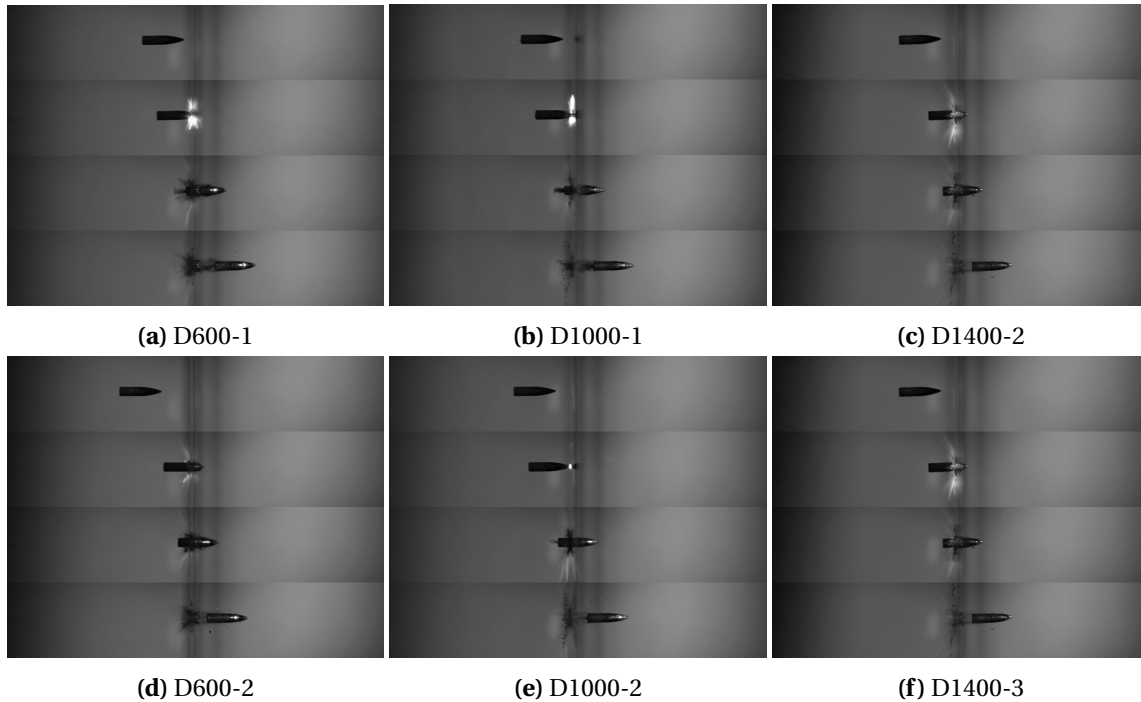
Figure 4.4: Picture sequence of ballistic impact of the plates. The images are taken with a high speed camera.

4.2 Blast Loading

4.2.1 Experimental Setup and Test Programme

The blast loads were applied in the SIMLab Shock tube Facility (SSTF), at the Department of Structural Engineering, NTNU. A brief introduction to the SSTF follows, but for further information the reader is referred to Aune et al. [35]. It is found that the SSTF resembles the loading of a far-field explosive detonation, and its performance was evaluated against European and international standards. Figure 4.5 depicts a schematic overview of the shock tube, which can be divided into the following sections; the driver, the firing, the driven and the tank section.
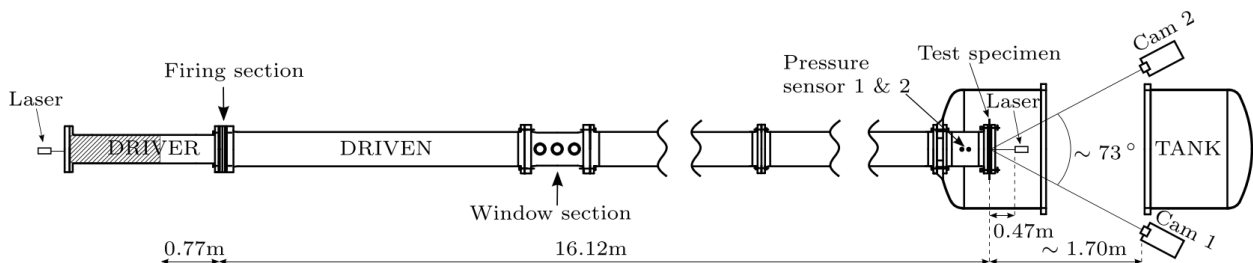
Figure 4.5: Schematic view of the shock tube. Picture is taken from Aune et al. [35]

The driver section is a high-pressure chamber, separated from the low-pressure chamber called the driven section. The firing section works as a barrier between the driver and driven, by using several diaphragms in-between intermediate chambers. The test starts by filling compressed air into the driver section until the desired pressure level. Controlled venting of the firing chamber will then initiate rupture of the diaphragms, resulting in a blast wave travelling along the tube until it impacts the test specimen mounted at the end of the driven section. The plate was mounted in the clamping assembly, consisting of M24 bolts and two massive steel plates with a square hole of 300 mm x 300 mm in the middle. Leaving the 0.8 mm plate with a pressure acting over the blast exposed area. Aune et al. [35] further showed that the incoming blast wave is planar. Figure 4.6a depicts the tank and the stereo setup of the high-speed cameras, while the three other sections are visible in Figure 4.6b. The properties of the blast wave was determined by the length of the driver section and diaphragms controlling the firing pressures. The same driver length of 0.77 m was used for all the experiments, but the use of diaphragms varied with the firing pressures. In this study firing pressures of 5, 15, 25, 35, and 60 bar were used. Before the pressure wave impact the plate its intensity was sampled by the two sensors closest to the plate; Sensor 1 and Sensor 2, seen in Figure 4.5, where Sensor 1 was positioned closest to the plate.

(a)   (b)
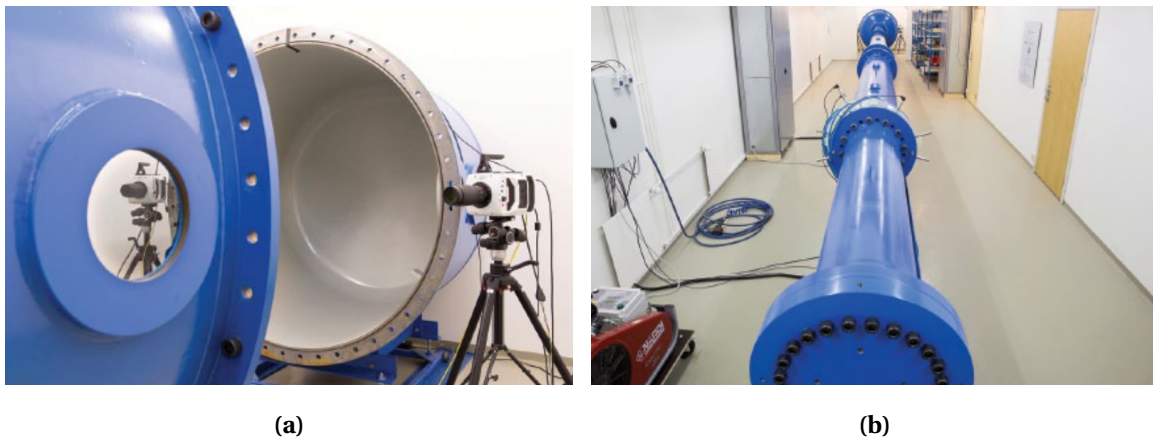
Figure 4.6: Pictures of shock tube taken from Aune et al. (2016) [35]: (a) the tank and the high speed cameras, and (b) the entire facility seen from the driver section.

The mounted plate is seen in Figure 4.8a. The high-speed cameras operated with a sampling rate of 37 kHz, and was synchronized to the pressure measurements at Sensor 1. In addition, the pressure data was sampled at 500 kHz. All plates were oriented the same way as for the ballistic tests, with the rolling direction in vertical direction.

Figure 4.7 illustrates the geometry of the plates with preformed holes. The squared area in the middle is the area that would be exposed to the incoming blast wave. The geometry of the ballistic impacted plates is presented in Figure 4.2 in Section 4.1.1. The test programme is summarized in Table 4.2. Each test is numbered based on the material_configuration_firing pressure. D6_C1_25 is therefore Docol 600, with a pre-formed circular hole in the centre and 25 bars of firing pressure. D10 and D14 are Docol 1000 and Docol 1400, respectively. B represents the plates that have been fired at with a rifle, C pre-formed holes, and D whole plates without holes. In
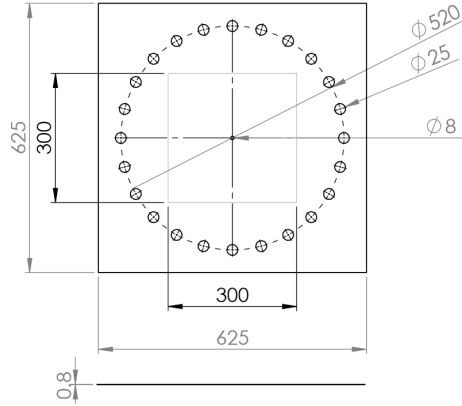
Figure 4.7: Geometry of the steel plates with preformed holes. The blast exposed area of 300 mm x 300 mm is indicated with grey solid lines.

addition to the steel plates tested for this thesis, data for massive steel plates were taken from Aune[28] for comparison. These are denoted as R_firing pressure for each given pressure.

Table 4.2: Test matrix of the blast loading experiments.

Firing pressure [bar]			
5	D10_D_05	-	-
15	D10_D_15	-	-
25	D10_D_25	D6_C1_25 D10_C1_25 D14_C1_25	D6_B1_25 D10_B1_25 D14_B1_25
35	D10_D_35	D6_C1_35 D10_C1_35 D14_C1_35	D6_B1_35 D10_B1_35 D14_B1_35
60	D10_D_60	-	-

4.2.2 Three-Dimensional Digital Image Correlation (3D-DIC)

All plates were first painted white before a black speckle pattern was applied, similar to that discussed in Section 2.3. This was done on the back side of the plate, which was visible for the high speed cameras shown in Figure 4.6a. The speckle pattern enabled post-processing with 3D-DIC in the in-house software eCorr[22]. Two high-speed cameras were used in a stereo vision setup to measure the full-field out-of-plane deformation of the plate when subjected to the blast loading. To calibrate the two cameras, to know which pixels correspond to the same position in both cameras, a cylinder with a checkered pattern was used as seen in Figure 4.8b. The cylinder

21

was placed at three different positions along the shock tube opening to accurately calibrate the entire plate. The cylinder had a small mark that is visible for both cameras that was used as a known common point in the calibration.

<div align="center">(a)   (b)</div>
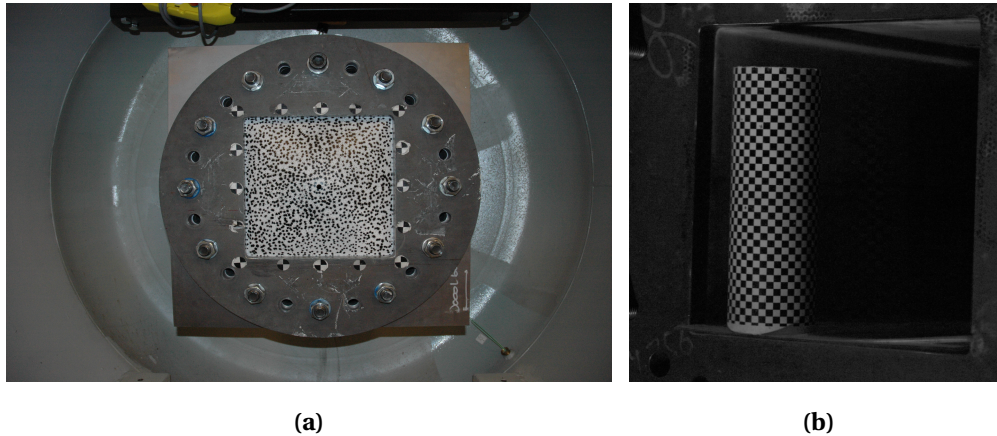
Figure 4.8: Plate and calibration: (a) plate with speckle pattern in the blast exposed area (seen from inside the tank), and (b) cylinder used for calibration of 3D-DIC in eCorr (seen from the high-speed cameras).

It was used FEM-based 3D-DIC in eCorr, where the plates were meshed with Q4 elements. The mesh is illustrated in Figure 4.9, indicating also where both deformation profiles and the reference point for deformation were collected. For the whole plates, without any holes, the profiles were sampled at the middle of the plate, at the positions of the blue line in Figure 4.9b. The yellow marker is the reference point for the out-of-plane deformation. The centre of the plate was found by finding the mesh centre. Note that if the mesh centre was not at one node, the closest possible point was used. The deformation of the plates that have holes was collected to the right of the holes instead, seen in Figure 4.9a. A square of size 3 x 3 elements was deactivated around the hole. This corresponds to approximately 18.1 mm from the centre. Meshing over a hole could lead to distorted elements, since the DIC program would have interpreted the plate as whole, which was clearly not the case. Also, small crack propagation around the whole could affect the results. Deactivation of the centre elements would still allow for investigation of the global deformation of the plates, which is what is primarily interesting from the 3D-DIC analyses in this thesis. Moreover, the entire rig moved during the test, whereas the cameras were fixed on the floor. To account for the rig movement, a subset was collected at the clamping frame for each test. The subset sampled the rigid body movement, which was subtracted from the plate deformation. It can be seen in Figure 4.9b as a green square with a dot in the centre on the left of the clamping frame. Other subsets were checked to ensure the chosen one is representative of the rig movement.
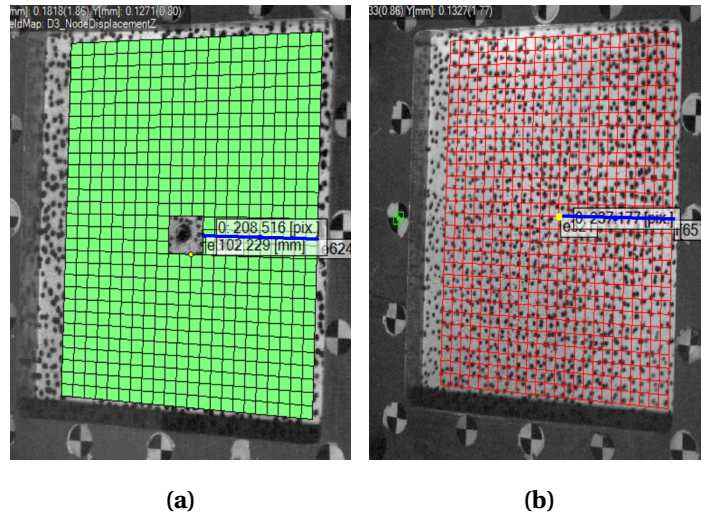
Figure 4.9: Vectors and nodes for data collection of profile deformation and point-wise deformation: (a) plates with holes, and (b) whole plates. Note that he mesh is deactivated around the hole and that the green marker to the left measures rigid body movement of the entire facility.

4.3   Laser Scanning

Furthermore, each plate was laser scanned before and after the blast with a ROMER Absolute Arm 7525SI laser scanner with a system scanning accuracy of 0.063 mm[36]. It created a point cloud of the plate in 3D, that was post-processed with the Matlab script in Listing 3 in Appendix B, to remove unnecessary points, such as the frame of the rig. This provided a basis to compare permanent deformations in the plates and a reference to evaluate the performance of the 3D-DIC measurements.

4.4   Experimental Results

4.4.1   Pressure Curves

Figure 4.10 contains the pressure histories at Sensor 1, while Table 4.3 provides the peak incident and reflected pressures measured at Sensor 1. The corresponding measurements for the rigid plates in Aune[28] are also included for comparison. For all the pressure data, the time axis was adjusted so that the time is zero when the pressure wave reaches Sensor 1, which is located 24.5 cm upstream the plate and the closest sensor.
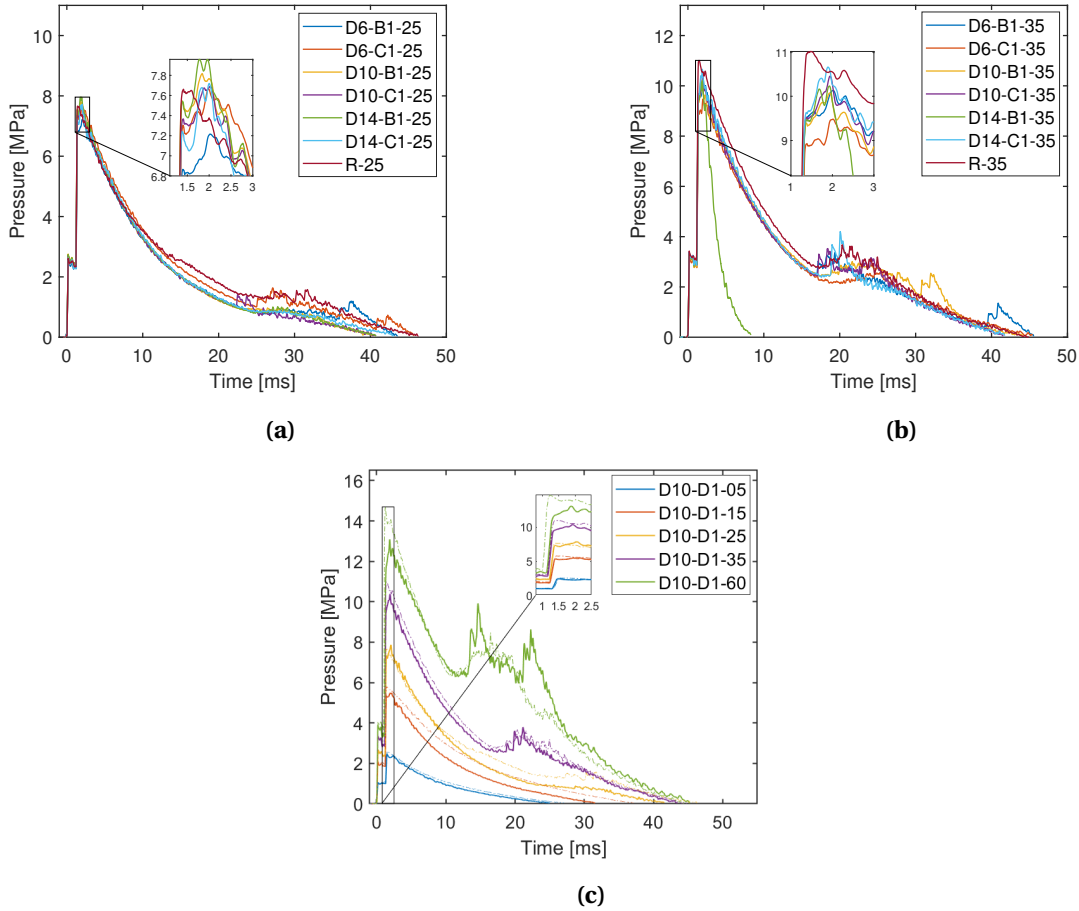
Figure 4.10: Pressure data from the Sensor 1 located 24.5 cm upstream from the clamped plates in the SSTF: (a) tests with 25 bar firing pressure, (b) tests with 35 bar firing pressure, and (c) whole flexible plates and massive plates (dotted lines).

It is observed some minor variations in both the firing pressure and the incoming pressure (Table 4.3). The magnitude of the peak incident pressures were 2.9 bar and 3.3 bar for firing pressures of 25 bar and 35 bar, respectively. The incoming pressure at Sensor 1 varied less and the range was 0.2 bar for 25 bar and 0.22 bar for 35 bar. As expected, variations in the incoming pressure will result in variations also in the peak reflected pressure. Except for tests D6_B1_25 and D6_C1_35, the incident pressures shows good agreement for similar firing conditions. This builds confidence towards that the pressure histories obtained on the rigid steel plates (R tests) can be used as an estimate for the loading in simulations neglecting fluid-structure interaction effects. The deviations in peak pressures for tests D6_B1_25 and D6_C1_35 is probably related to the fact that the firing pressures which also showed lower magnitudes in this tests. It is also interesting to note that the reflected peak pressure seems to increase with increasing strength of the material.

Table 4.3: Pressure data from Sensor 1 in the experimental tests. The corresponding measurements for the rigid plates in Aune[28] are also included for comparison. Δp_{so} and Δp_r are the percentage deviation of each experiment's incoming and reflected pressures, respectively, to that of the rigid plates. t_s is the calculated time from when the pressure wave hits the plate until stabilization of the deformation of the plate, as marked in Figure 4.12.

Test	Firing pres. [bar]	Incoming pres. $p_{so,max}$ [bar]	Δp_{so} [%]	Reflected pres. $p_{r,max}$ [bar]	Δp_r [%]	t_s [ms]
R_25	27.2	2.78	-	8.05	-	-
D6_C1_25	24.9	2.83	1.80	7.81	-2.98	1.04
D6_B1_25	23.9	2.71	-2.5	7.33	-8.9	1.18
D10_C1_25	24.2	2.85	2.5	7.82	-2.85	1.43
D10_B1_25	24.3	2.91	4.7	8.10	0.62	1.40
D14_C1_25	24.1	2.77	-0.36	8.05	0.00	1.59
D14_B1_25	24.3	2.89	4.0	8.19	1.74	1.62
R_35	37.1	3.65	-	11.3	-	-
D6_C1_35	34.9	3.43	-6.0	9.65	-14.6	0.96
D6_B1_35	36.9	3.59	-1.6	10.3	-8.84	1.08
D10_C1_35	36.7	3.61	-1.1	10.8	-4.42	1.08
D10_B1_35	36.9	3.54	-3.0	10.3	-8.84	1.13
D14_C1_35	37.8	3.55	-2.7	11.2	-0.88	1.40
D14_B1_35	37.0	3.62	-0.82	10.6	-6.19	-
R_05	5.19	1.16	-	2.71	-	-
D10_D_05	5.19	1.09	-6.0	2.62	-3.32	1.72
R_15	14.9	2.22	-	6.04	-	-
D10_D_15	15.2	2.24	0.9	5.70	-5.33	1.56
R_25	27.2	2.78	-	8.05	-	-
D10_D_25	24.0	2.85	2.5	8.04	-0.12	1.27
R_35	37.1	3.65	-	11.3	-	-
D10_D_35	37.6	3.54	-3.0	10.6	-6.19	1.19
R_60	59.7	4.34	-	15.4	-	-
D10_D_60	61.9	4.21	-3.0	13.5	-12.3	1.05

In Figure 4.10, the pressure histories from Sensor 1 are plotted for all plates as well as the pressure data from tests with massive plates by Aune[28]. It should be noted that the data in Table 4.3 was taken from the raw pressure data from the experiments, while the pressure curves were filtered using a moving mean average approach[37]. This was to make the curves easier to visually inspect. Recall that the curves are shifted in time so that the blast wave arrives at Sensor 1 at $t = 0$. This point is seen as the the first sudden peak in pressure. This will also be used for synchronization of the displacement data and the pressure data. Figure 4.10c shows the pressure-time histories of the D10_D1 plates compared to the tests on massive steel plates. The whole flexible plates induced a small reduction in reflected pressure which seemed to increase with the firing pressure. This was also found by Aune[28]. The exception was D10_D_25. D10_D_15 and D10_D_25 experienced a reduced pressure almost throughout the positive phase. Aune[28] also experienced this and stated the reason as unknown. The shape of the reflected pressure

was more rounded for the deformable plates compared to the rigid, and the peak pressure occurred after Sensor 1 initially picked up the reflected wave. This was a results of the deflection of the plates, and is probably due to effects of Fluid-structure interaction (FSI). That is, the deformation of the plate alters the pressure acting on it [38]. In general, a large deformation yields a large FSI effect [39] [40]. As the massive plates should exhibit close to no FSI-effects, the reduced reflected pressure for the flexible whole plates also indicate an effect of FSI present in the experiments.

The pressure curves presented in Figure 4.11 suggest that no significant difference can be seen in the pressure magnitude during the positive phase between whole and the two types of perforated plates. This is also supported by Figures 4.10a and 4.10b where the pressure curves, at least before the secondary reflection wave, are very similar. The secondary reflection wave is the second sudden increase in pressure after the pressure drop succeeding the peak reflected pressure. These become more evident for larger firing pressures, readily seen from Figure 4.10c. Figure 4.10b shows the noticeable drop in pressure for D14_B1_35. This is because the plate failed completely and the air was allowed to pass freely into the tank.
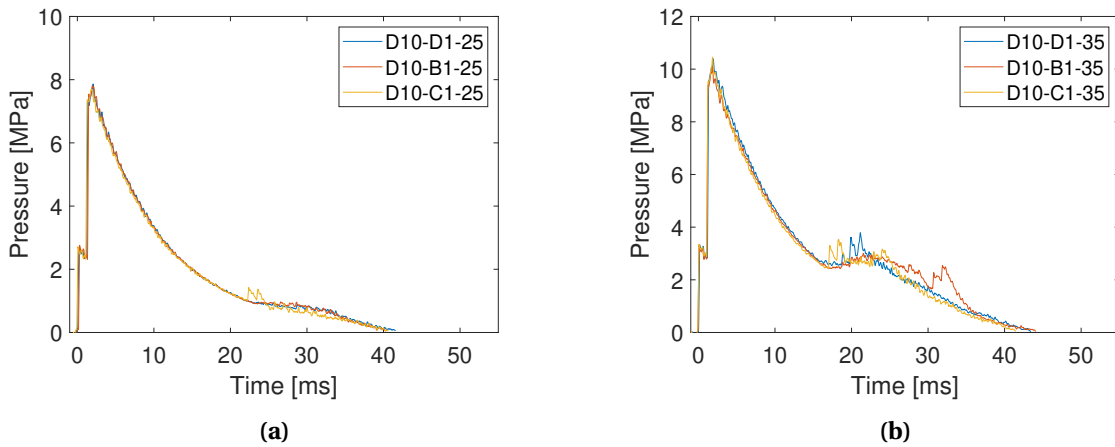
Figure 4.11: Pressure data for Docol 1000: (a) pressure data for D, C and B configurations for 25 bars of firing pressure, and (b) shows the same pressure data for tests with firing pressure of 35 bars.

4.4.2 Loading Regimes

Different strain rates may result in different loading regimes, which are divided into three categories; quasi-static, impulsive, and dynamic regimes. If the loading is applied and removed before the structure has time to deform, it is classified as impulsive. The time the structure takes to start deforming is decided by its natural frequency [20]. The quasi-static domain is the opposite of the impulsive; the loading's duration is far longer than the time the structure takes to respond to the load. The structural response in the impulsive domain is only dependent on the magnitude of the load impulse. For the quasi-static, the response is only dependent on the structure's stiffness and the peak reflected pressure. Between the two, the dynamic regime exists, as the loading time is similar to the structural response time. As opposed to the other regimes, the dynamic regime is dependent on the loading rate. In general, the different regimes

are distinguished by the relations in Equation (14) [20].

$$\text{Impulsive}: \omega_n t_d < 0.4$$
$$\text{Dynamic}: 0.4 < \omega_n t_d < 40 \tag{14}$$
$$\text{Quasi} - \text{static}: \omega_n t_d > 40$$

where t_d is the duration of the positive phase and ω_n is the natural frequency. In this thesis, only thin square plates have been considered, which have a fundamental natural frequency that can be found in Equation (15) [41], where thin plate theory is assumed, as well as isotropy and homogeneity. Furthermore, it is assumed that each side is simply supported.

$$\omega_{mn} = \frac{2\pi^2}{a^2}\sqrt{\frac{D}{\rho t}}, \tag{15}$$

where

$$D = \frac{Et^3}{12(1-\nu)}$$

and a is the side length of the plate, ρ is the density of the material and t is the thickness of the plate. E is the Young's modulus and ν is Poisson's ratio. A square steel plate with side lengths of 300 mm and thickness of 0.8 mm will therefore have a fundamental natural frequency of 275.5 rad/sec. The same plate, only fully clamped will have a natural frequency of 502.3 rad/sec [41].

The loading regime seemed to be within the dynamic region, as the pressure curve lasted for approximately 40 ms for each plate, which gives $\omega_n t_d = 11.0$ for simply supported plates, and $\omega_n t_d = 20.1$ for fully clamped plates. Simply supported plates are introduced here because it is expected that the fully clamped boundary condition is too strict, although the plates are indeed bolted and clamped during the experiments. The plates' deformations seemed to stabilize around a level of deformation before the pressure load was removed, as seen in Figures 4.13 and 4.14. At this level it only oscillates, and the load does not affect the deformation, apart from the oscillations. If the time where the stabilization of deformation is chosen as the duration of the loading, in stead of the entire positive phase, the response may be considered in the impulsive regime. This is known as the saturated impulse [42]. The last column in Table 4.3 gives t_s, i.e., the time it takes from the point where the plate first experiences the pressure wave until the stable deformation was reached. Figure 4.12 depicts the pressure curve of sensor 1 and the loading experienced by the plate for D6_B1_25, in combination with the measured reference point deformation of the plate from 3D-DIC. The point of maximum deformation is indicated with a diamond marker, and the point where the deformation stabilizes is marked with ×. From this, it is evident that the structural response is less affected by the blast wave after only a short loading time. t_s ranges from 1.04 ms to 1.72 ms. Assuming a simply supported plate, $\omega_n t_d$ is now in the range 0.28 to 0.47. With the definition from Equations (14), the loading was mostly within the impulse regime. In contrast, the experiments of Aune [28] with C-4 explosives and Docol 600, the loading had passed before the response of the plate begun. In conclusion, the loading regimes in this thesis are balancing between dynamic and impulse, and it is clear that the loading influence the response until the point of maximum deformation.
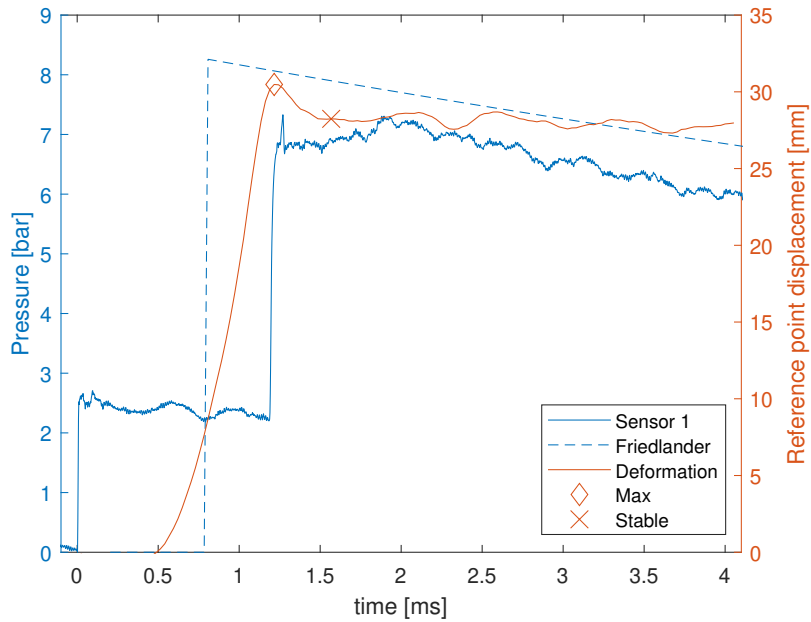
Figure 4.12: The pressure for sensor 1 of D6_B1_25 is shown in blue, and the loading experienced by the plate is shown in blue dashed lines. The orange line shows the deformation of the reference point. The 'diamond' marks the time of the maximum deformation, and the × marks the time of stabilization of the deformation.

4.4.3 Deformation Measurements

Because the plates are thin, mostly membrane forces are expected which will yield out-of-plane deformations described in this section. The 3D-DIC was used to extract deformations at the chosen reference point described in Figure 4.9a in Section 4.2.1. In Figure 4.13 the reference point deformations can be seen for the plates of configuration B and C. Similar to the pressure measurements in Section 4.4.1, the time axis for the deformation histories was adjusted so that the time is zero when the pressure wave reaches Sensor 1. The deformations were plotted from time zero and for the following 4 ms. If a plate experienced large fracture or total failure, the time was marked with a black cross, and the rest of the deformation removed from that point in time.

From Figure 4.13a, it can be seen that the reference point deformations are very similar for the plates with the same firing pressure. The deformation is slightly higher for D6_B1_25 than for D6_C1_25, which could be due to it already being slightly deformed from the perforation. It is harder to compare D6_C1_35 and D6_B1_35 because the latter experience failure. Up until failure they have a very similar deformation. The same can be said for D10_B1_25 and D10_C1_25 in Figure 4.13b. D10_B1_35 failed before the maximum deformation was reached, and so did D14_B1_25, D14_B1_35, and D14_C1_35. Furthermore, the D600 plates undergo smaller elastic deformations compared to the D1000 plates and the D1400 plates. The oscillations of the D1400 plates have the highest amplitude, which is consistent with the findings of Elveli et al.[11].

The reference point defined in Figure 4.9b in Section 4.2.1 was used to sample points for whole

28
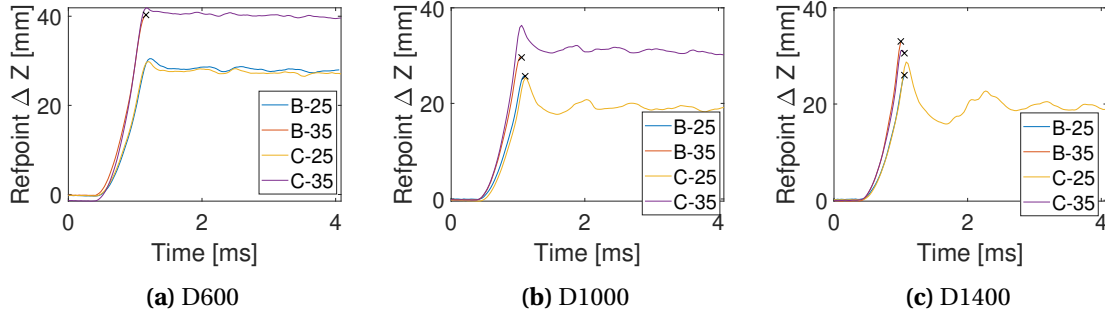
Figure 4.13: Reference point deformation for plates of B and C configuration for each material.

plates. None of the whole plates experienced any fracture, and the plots can be seen in Figure 4.14.
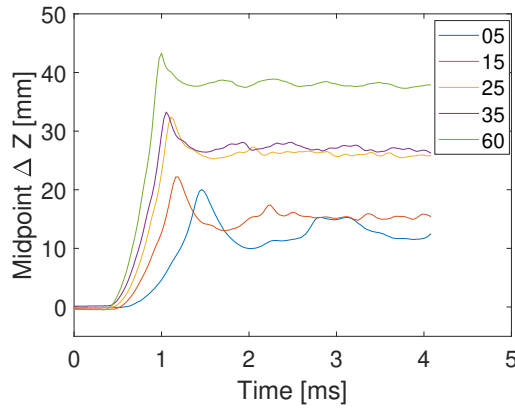
Figure 4.14: Midpoint displacements of whole plates of Docol 1000 DP

As expected, the lower the pressure, the longer time it takes to travel to the plate. The elastic rebound of the plates becomes smaller as the firing pressure increased. This was also found by Aune[28]. The maximum midpoint deformations are more similar than could be expected for D10_D_25 and D10_D_35. The same tendency is seen for D10_D_05 and D10_D_15, though not as pronounced. Some of the effect could be contributed to differences in the pressure waves. The reflected pressure of D10_D_05 and D10_D_15 deviates from that of the massive plates by $-3.32\,\%$ and $-5.33\,\%$, respectively, as seen in table 4.3. For D10_D_25 and D10_D_35 the deviations are $-0.12\,\%$ and $-6.19\,\%$, respectively. Furthermore, the coarseness of the DIC mesh could have hindered sampling at the exact centre of the plate, which could have lead to e.g. D10_D_35 being read slightly off-centre, leading to a lower deformation. It is also possible that the DIC is inaccurate. There are however, strong evidence that the latter is not the case, as a similar pattern is seen for the whole plates in the point clouds from the laser scanner in Section 4.4.5. It should be mentioned that the deformation profiles were not always symmetrical about the hole in the plates. This can be seen from Figure 4.19 which shows the deformation of a plate in the z-direction for different time steps. Therefore, extracting the reference point deformation from the point in Figure 4.9b was a choice that might affect the comparison of the results from the numerical simulations. The same holds for the deformation profiles. The difference in

29

deformation was investigated by choosing various points around the hole as reference points. For the whole plates a few points were chosen as the midpoint. The deformation deviated to a small degree, no more than 3 mm. Therefore the extraction method in 4.9 in Section 4.2.2 was consistently used, for which the highest deformation was most commonly obtained.

The deformation profiles at the vectors defined in Figure 4.9 are extracted at different times. They were plotted at the maximum deformation of the plate, and the time as close as possible to 90 %, 75 %, 60 %, and 40 % of the maximum deformation. The only exception is the plate D14_B1_35, which experienced complete failure, and instead of maximum deformation, the last deformation before failure was used. As the DIC was only sampled at 37 kHz, some of the plotted deformations may be slightly higher or lower than exactly the given percentage of maximum deformation. The exact times, for which the profiles are found, are however reported in the deformation plots. The profiles for D600 can be found in Figure 4.15, D1000 in Figure 4.16, and D1400 in Figure 4.17. As the loading increased until the maximum deformation was reached, the lowest time in the plots corresponds to the lowest deformation, the highest time to the highest deformation, and so on. The Matlab script used to generate the plots can be found in the appendix in Listing 1.

(a) D6_C1_25

(b) D6_C1_35

(c) D6_B1_25

(d) D6_B1_35
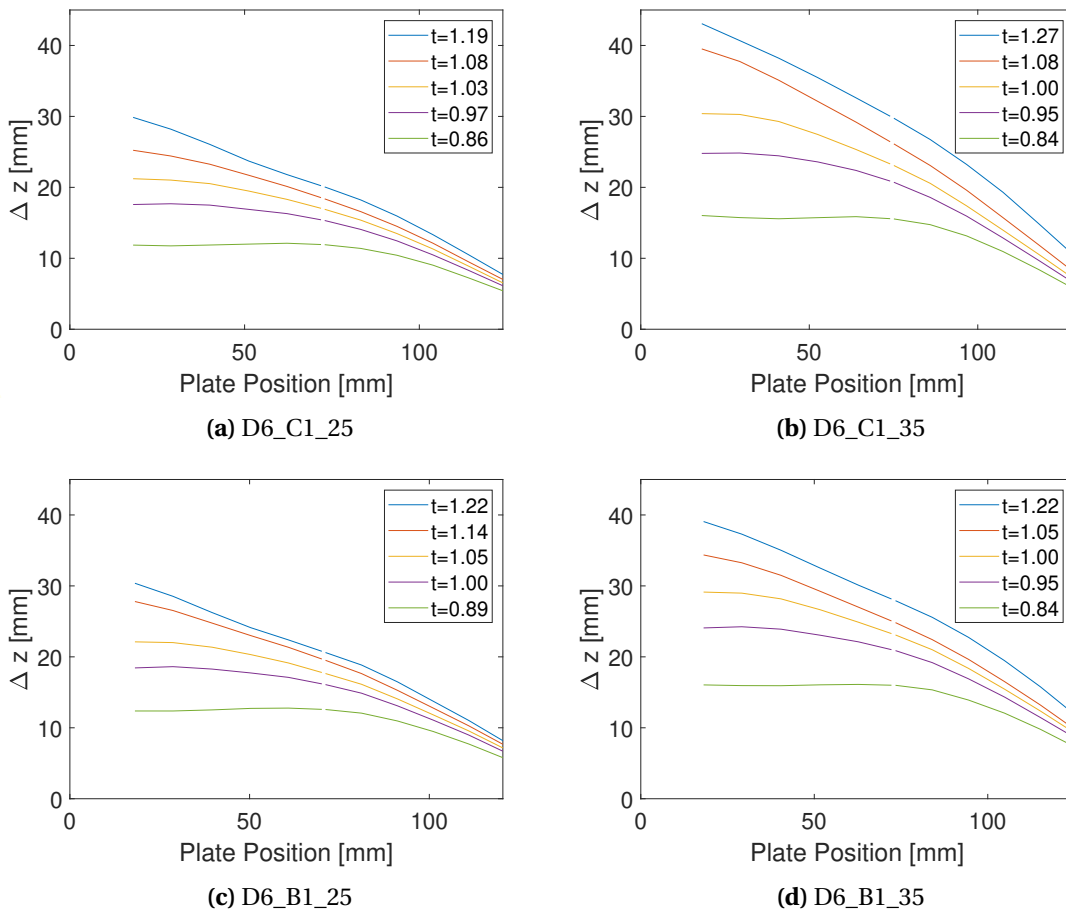
Figure 4.15: D600 deformation profiles of half the plate from the centre of the plate. The green profile is at 40 % of maximum deformation, purple at 60%, yellow at 75 %, red at 90 % and blue at 100 %. The legends give the sampling time in milliseconds.

The deformation profiles for half the plates of D600 in Figure 4.15 are of similar shape to a global dome. Furthermore, it is seen that for the same material and firing pressure, but different configuration, the global deformation is very similar. The peak deformations of D6_C1_25 and D6_B1_25 are almost identical, and the same goes for the plates at 35 bar. The same trend is observed for Docol 1000 in Figure 4.16. However, the D1000 plates' profiles are less like a global dome compared to D600, as the curve is less smooth for D1000.
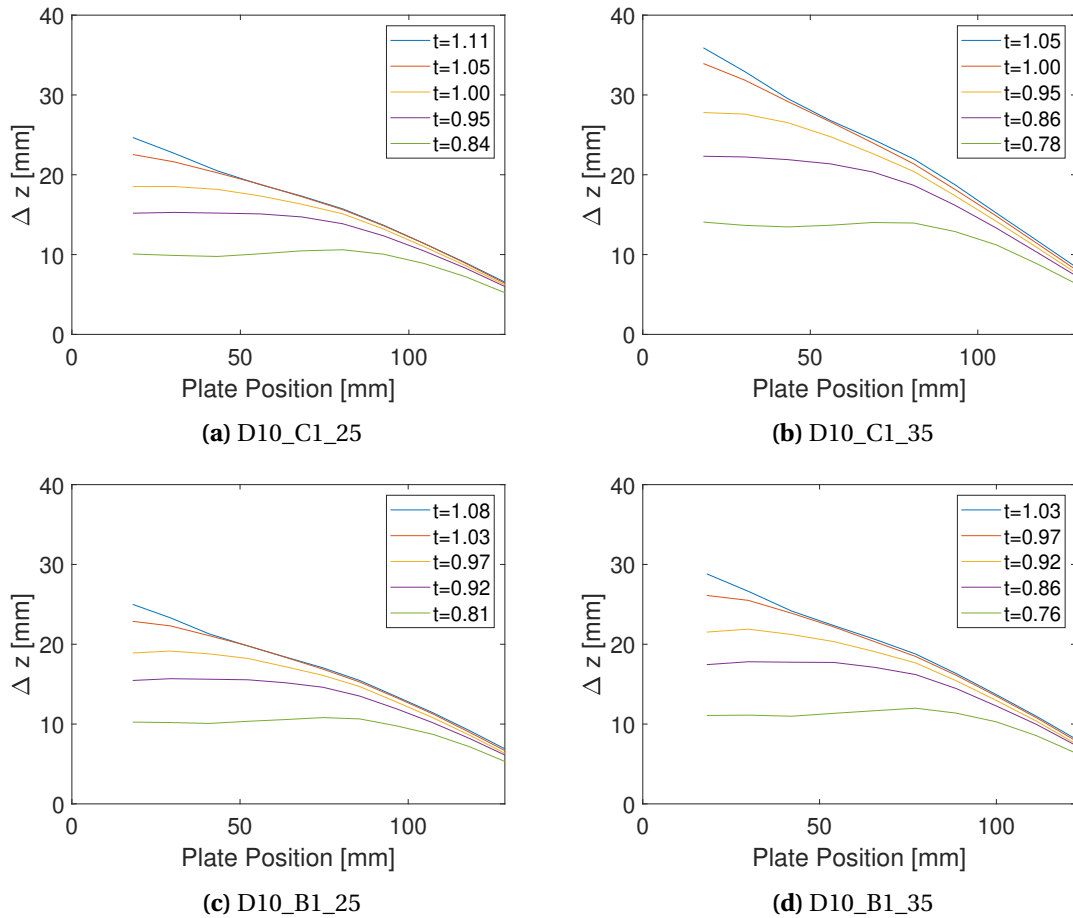
Figure 4.16: D1000 profiles of half the plate from the centre of the plate. The green profile is at 40 % of maximum deformation, purple at 60%, yellow at 75 %, red at 90 % and blue at 100 %. The legends give the sampling time in milliseconds.

The deformation profiles of Docol 1400 can be seen in Figure 4.17. Here, it is evident that deformation profiles are even less like a global dome compared to the Docol 1000 profiles.

(a) D14_C1_25

(b) D14_C1_35

(c) D14_B1_25

(d) D14_B1_35
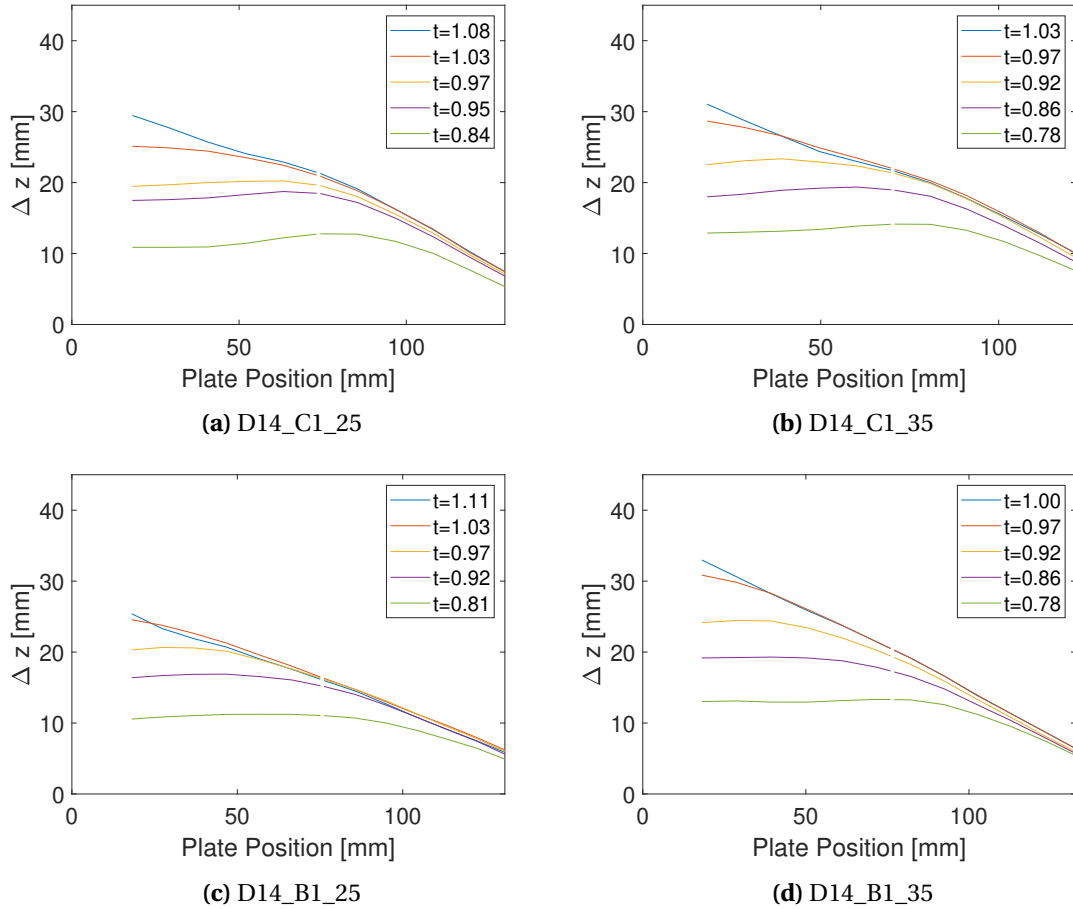
Figure 4.17: D1400 profiles of half the plate from the centre of the plate. The green profile is at 40 % of maximum deformation, purple at 60%, yellow at 75 %, red at 90 % and blue at 100 %. The legends give the sampling time in milliseconds.

The same procedure was used to find the deformation profiles of the whole plates as described above. The result is seen in Figure 4.18. Here, it is seen that a higher pressure yield a higher deformation, and that the pressure wave takes longer to induce maximum deformation for the lower pressures than the higher pressures.

(a) D10_D_05   **(b)** D10_D_15   **(c)** D10_D_25

(d) D10_D_35   **(e)** D10_D_60
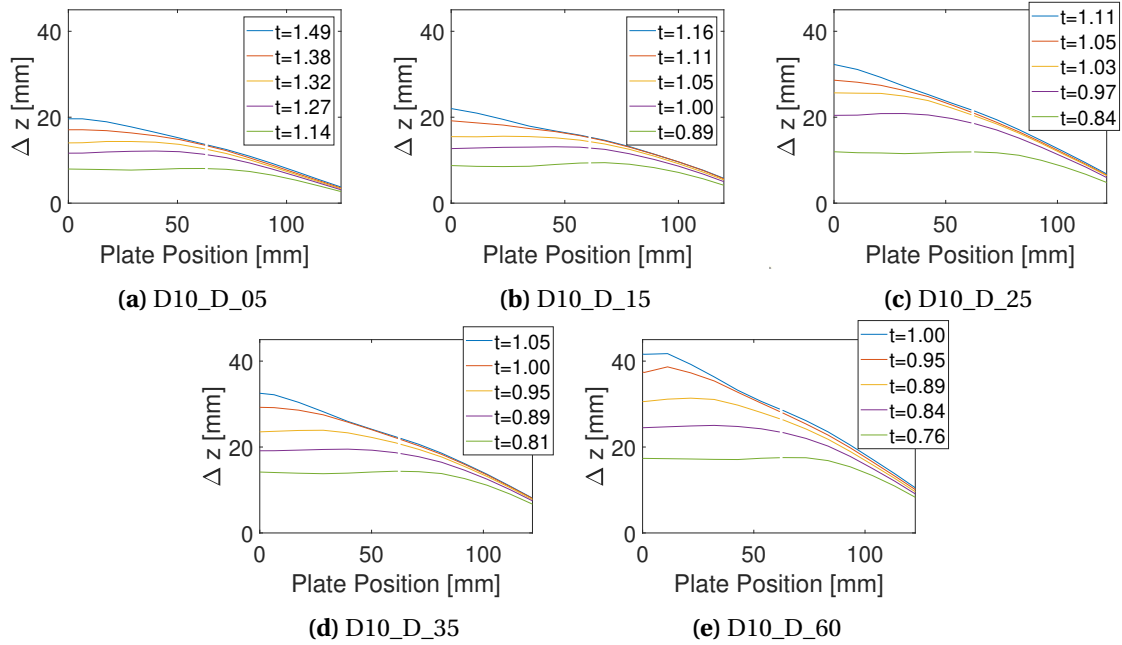
Figure 4.18: D1000 whole plate deformation profiles of half the plate from the centre of the plate. The green profile is at 40 % of maximum deformation, purple at 60%, yellow at 75 %, red at 90 % and blue at 100 %. The legends give the sampling time in milliseconds.

4.4.4 Plastic Hinge

A plastic hinge is created when the plastic moment, M_p, is exceeded and a plastic deformation occurs by rotation[43]. A travelling plastic hinge, as opposed to a stationary plastic hinge, moves over an area as the loading increases. In a material that work hardens, the plastic moment increases with the rotation[43]. In the following Figure 4.19, an example of the travelling plastic hinges of the plates are observed. In the sequence, the plastic hinge can be seen travelling from the four corners of the plate and in towards the centre of the plate, creating the 'X' described in the following section.
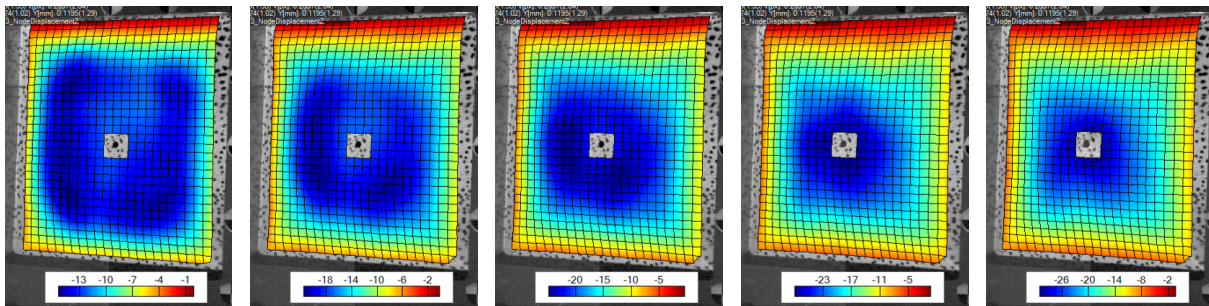
(a) 40 % of max def at t = 1.03 ms.   **(b)** 60 % of max def at t = 0.97 ms.   **(c)** 75 % of max def at t = 0.92 ms.   **(d)** 90 % of max def at t = 0.86 ms.   **(e)** 100 % of max def at t = 0.78 ms.

Figure 4.19: Travelling plastic hinge development of D14_C1_35. Each of the five figures are at 40 %, 60%, 75 %, 90 % and 100 % of the maximum deformation.

33

Jones[44] showed that a material with low material hardening would produce plastic hinges with more deformation than a material with considerable hardening. A perfectly plastic material would produce a sharp, localized deformation at the plastic hinge, whereas a work hardening material would spread out the deformation over the area of the plate. It can be seen from the deformation profiles in Figures 4.15, 4.16, 4.17 and 4.18 that the plastic hinges, represented by the bends in the curves are more pronounced for D14 than for D10, and more for D10 than for D6. Furthermore, the hinges are also more distinct at higher firing pressures. For ease of comparison of the plastic hinges of the materials, Figure 4.20 is included.
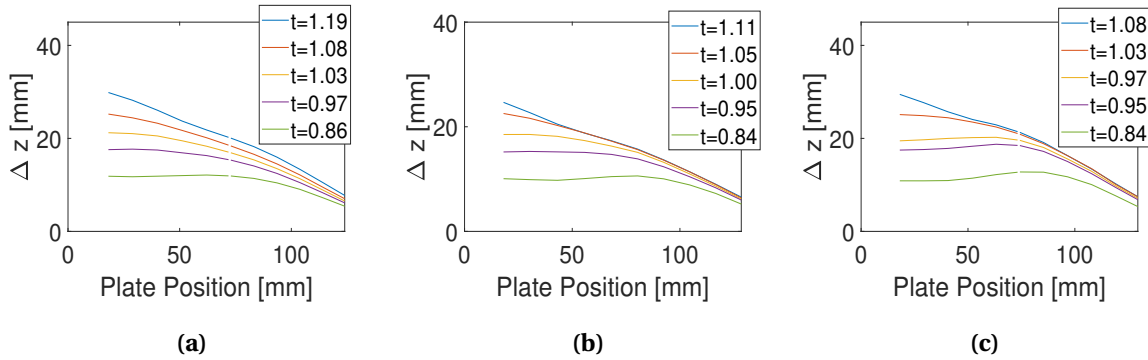
Figure 4.20: Comparison of the deformation profiles of the different materials, all undergoing 25 bars firing pressure and of C configuration: (a) D6_C1_25, (b) D10_C1_25, and (c) D14_C1_25.

4.4.5 Point Clouds

The point clouds generated with the laser scanner are imported into Matlab with the code in Listing 2, and unnecessary points on the edge from the frame is removed with the script in Listing 3. The results can be seen in Figure .9 in Appendix F. All data from the point clouds are in mm.

(a) D6_C1_25   **(b)** D10_C1_25   **(c)** D14_C1_25

(d) D6_B1_25   **(e)** D10_B1_25   **(f)** D14_B1_25

(g) D6_C1_35   **(h)** D10_C1_35   **(i)** D14_C1_35

(j) D6_B1_35   **(k)** D10_B1_35
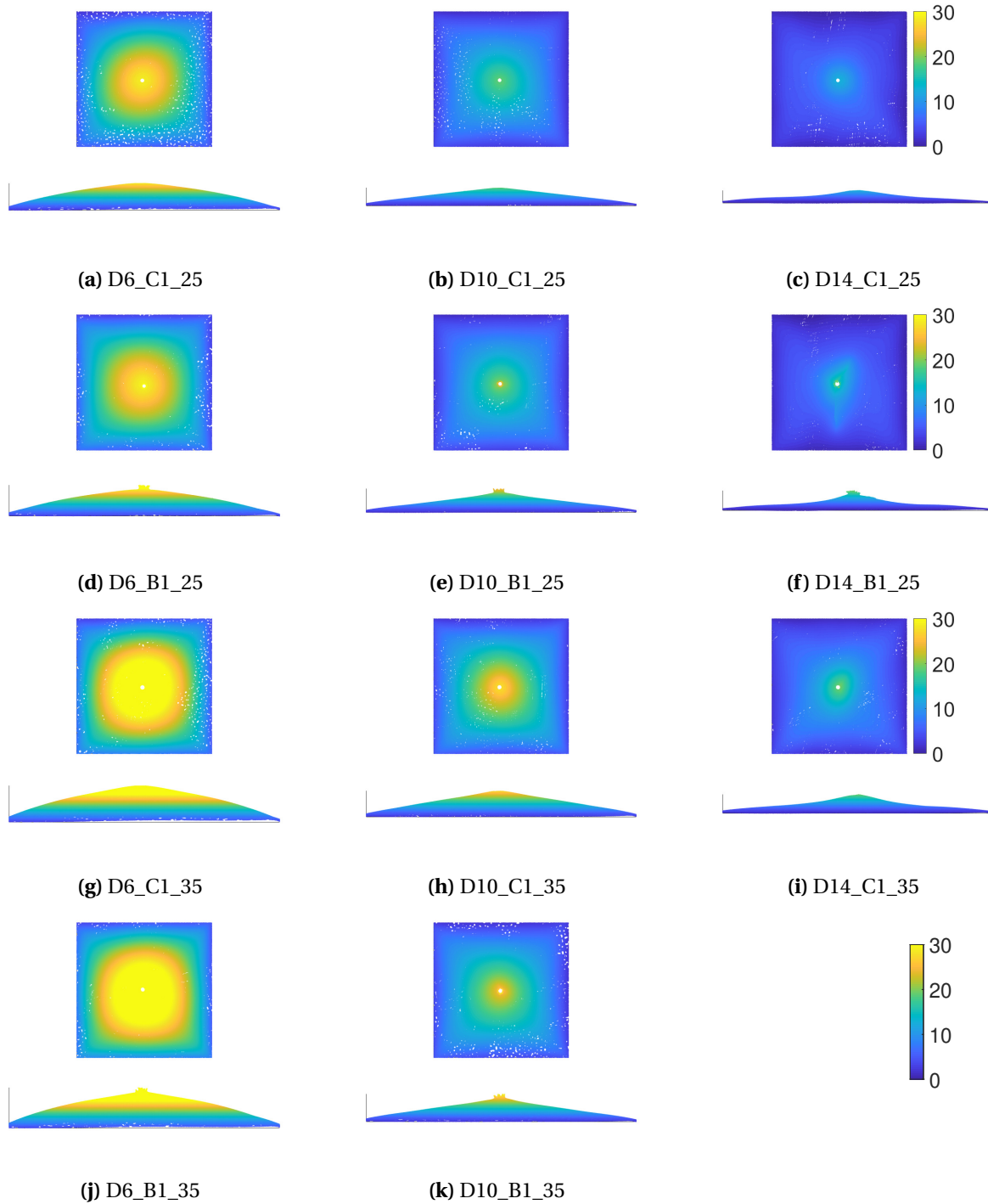
Figure 4.21: Point clouds of perforated plates after being subjected to blast loads. The measurements on the colour bars are in mm.

It is clear from the point clouds for holes with plates in Figure 4.21 that the permanent deformation is increasing with higher pressures. This is also seen in Figure 4.22, where whole plates of D10 with different pressures are compared. Furthermore, Figure 4.21 confirms that the permanent global deformation is lower for the steels with the highest martensitic content so that

D600 has the highest deformation followed by D1000, and D1400 with the lowest deformation. Also, the trend seen for the deformation profiles is confirmed here; the permanent deformation is also more like a global dome for D600 than for D1000 and D1400. For D1400, the deformation mostly occur at the path from the corner of the plate to the centre of the plate, which is seen as an 'X' of lighter shade of blue in figures 4.21c, 4.21f and 4.21i.

(a) D10_D_05   **(b)** D10_D_15

(c) D10_D_25   **(d)** D10_D_35   **(e)** D10_D_60
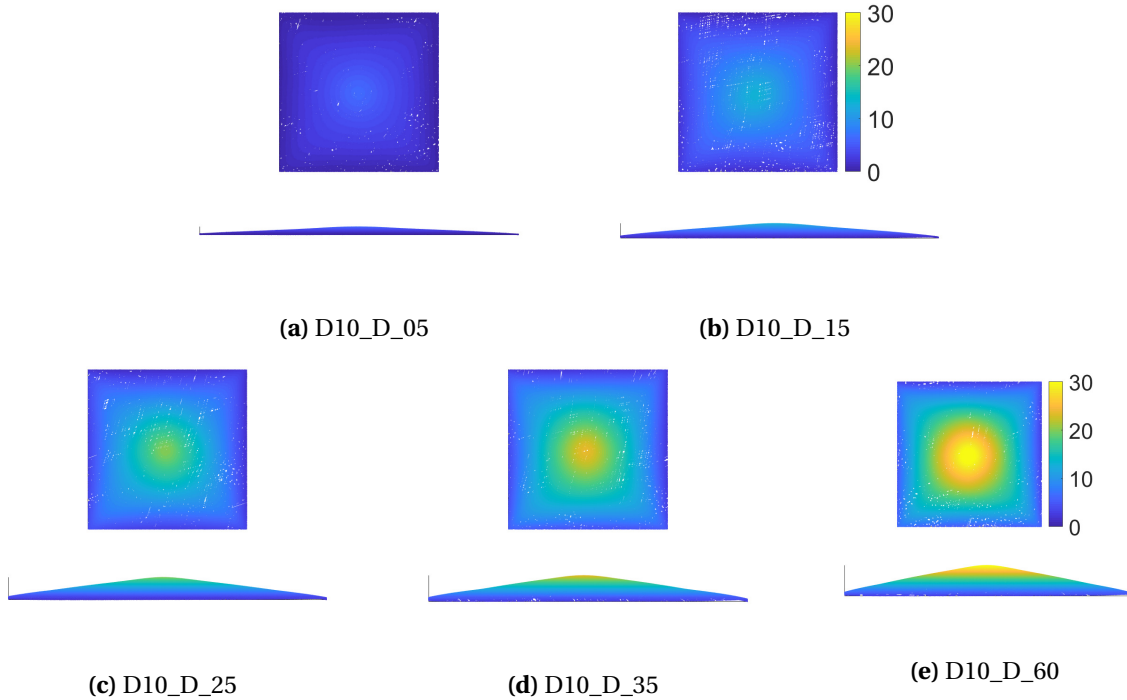
Figure 4.22: Point clouds of whole plates after being subjected to blast loads. The measurements on the colour bars are in mm.

4.4.6 Failure Modes

The observed failure modes are described in Table 4.4. Where the failure mode is global deformation it was not observed any new fractures during the blast tests. Where the mode is crack arrest, the plate either developed new cracks or, in the case of the ballistic plates, already existing cracks propagated. However, the cracks did not propagate all the way to the end of the clamping frame, as they did for D14_B1_35 , which experienced total failure. C1, C2, and C3 in Table 4.4 represents the length of the cracks after the blast loading, and the notation follows the one described in Figure 4.23. The cracks are measured from the edge of the pre-exisiting hole with an electronic caliper having a resolution of 0.01 mm, and an accuracy of 0.03 mm[45].

Table 4.4: Failure modes and plate response for all tests, including crack lengths where applicable. C1, C2 and C3 denotes the fractures of each plate following the notation used in Figure 4.23. D6 refers to the material Docol 600, D1000 to Docol 1000, D14 to Docol 1400. C is the configuration with a machined hole and B has bullet holes. The last number is the firing pressure.

Name	Mode	C1	C2	C3
D6_C1_25	Global deformation	-	-	-
D6_C1_35	Global deformation	-	-	-
D6_B1_25	Global deformation	-	-	-
D6_B1_35	Crack arrest	5.81 mm	5.52 mm	-
D10_C1_25	Global deformation	-	-	-
D10_C1_35	Global deformation	-	-	-
D10_B1_25	Crack arrest	9.83 mm	6.24 mm	-
D10_B1_35	Crack arrest	7.28 mm	4.08 mm	9.88 mm
D14_C1_25	Global deformation	-	-	-
D14_C1_35	Crack arrest	27.22 mm	13.82 mm	-
D14_B1_25	Crack arrest	52.44 mm	86.99 mm	17.33 mm
D14_B1_35	Total failure	-	-	-
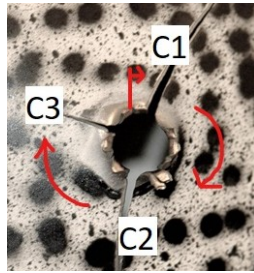
Figure 4.23: System for fracture notation. The first crack, C1, is the first after the red line and C2 and C3 follows in clockwise direction.

It is evident that the ballistic plates undergo more damage than the plates with machined circular holes. Four blast tests are carried out for each material. Only one of the plates of the D6 material fractures, and the cracks are the shortest in the test matrix. Two of the D10 plates fractures and experiences crack arrest. Three of the D14 plates fractures, all three have longer cracks than D6 and D10 and one of the plates experiences total failure. Furthermore, the more ductile materials also seem to exhibit less fracture than the high strength materials. The fractures mostly present themselves in the vertical direction, and if there are several cracks, they are usually longer in the vertical direction, rater than the horizontal. This is apparent for D14_B1_25 and D14_C1_35 seen in Figure 4.24.

The fracture of D14_B1_25 and D14_C1_35 are very similar even though the first only experienced a load due to a firing pressure of 25 bar. Both front and back of each plate are depicted in Figure 4.24. Note that if the names have the addendum F, it is the front of the plate, and B represent the back of the plate. Both the blast and ballistic load entered the plate at the front side.
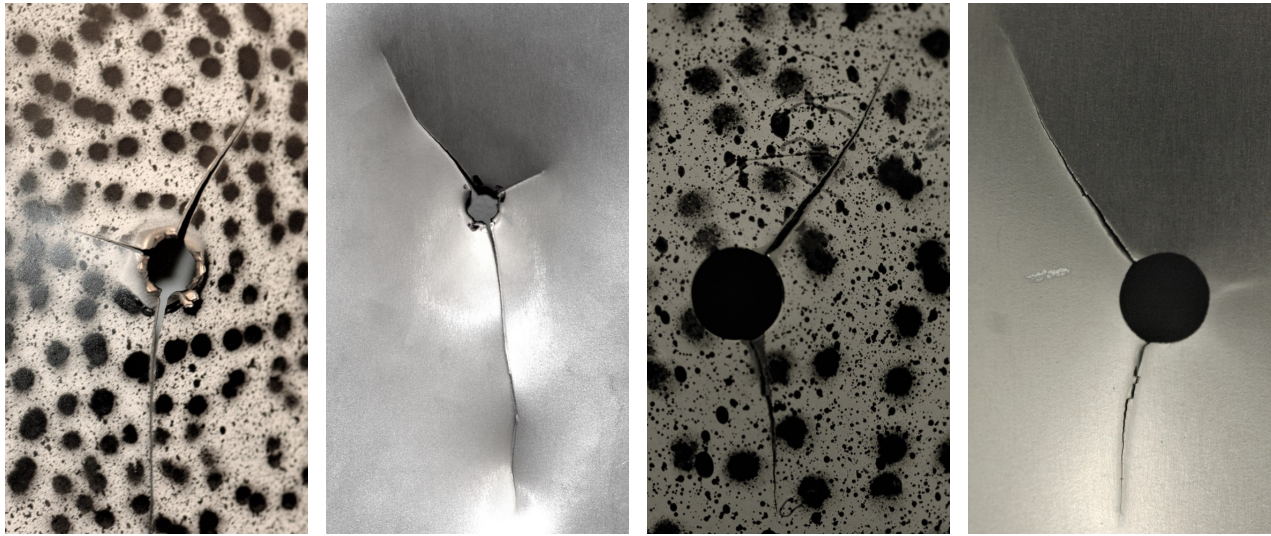
(a) D14_B1_25_B　　　　**(b)** D14_B1_25_F　　　　**(c)** D14_C1_35_B　　　　**(d)** D14_C1_35_F

Figure 4.24: Plates with large crack arrest after blast.

Most of the plates with pre-formed holes only experienced large global deformation, and experienced no fractures. An example of that is in Figure 4.25.
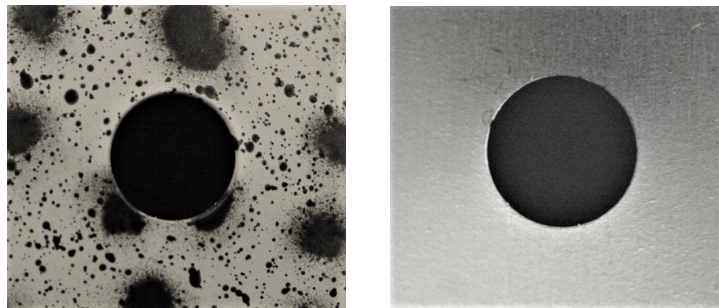
(a) D14_C1_25_B after undergoing blast loading.　　**(b)** D6_D14_25_F after undergoing blast loading.

Figure 4.25: Plates with large deformation after undergoing blast deformation.

Some of the plates experienced a small increase in the crack length; D6_B1_35, D10_B1_25, and D10_B1_35, seen in Figure 4.26. These cracks mostly propagated from the ballistic fracture, thus the plates of B configurations were the most prone to fracture.

(a) D6_B1_35_B   **(b)** D10_B1_25_B   **(c)** D10_B1_35_B

(d) D6_B1_35_F   **(e)** D10_B1_25_F   **(f)** D10_B1_35_F
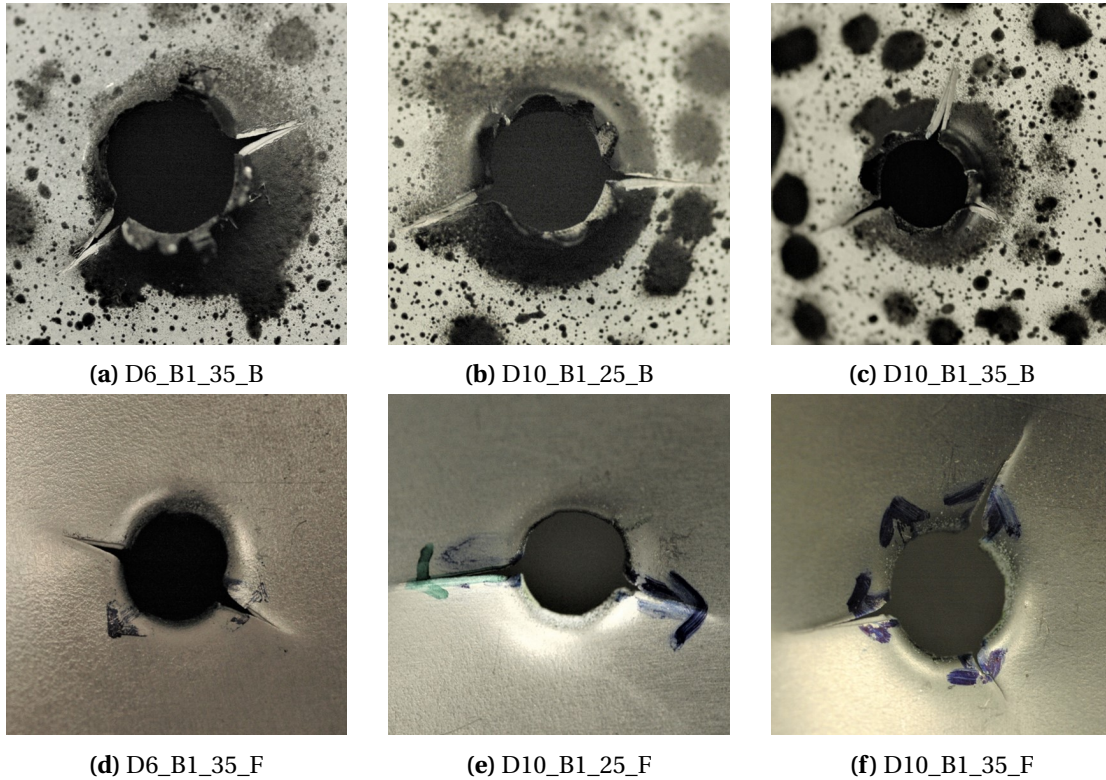
Figure 4.26: Plates with small crack arrest after undergoing blast loading.

In general, it is seen that fracture in the rolling direction, dominates compared to fracture in the horizontal direction, which is 90° to the rolling direction. As mentioned in Section 2.1, the plates are cold rolled, which have been found to affect the plastic isotropy of the material in a study by Gosh and Ray[46]. They found that the plastic anisotropy increases with increased cold-rolling. A thin plate is likely to be more cold rolled than a slightly thicker plate, such as the plates that have been used to discuss isotropy in the articles in Section 3.1, where some are of different thicknesses. This may indicate that there is some anisotropy in the material due to the cold-rolling, but further investigation is needed to conclude.

4.5 Concluding Remarks

The perforation process was similar for the majority of the ballistic impact tests. The difference in initial and residual velocity was 1.89 % at maximum, which supported the assumption that the plates did not suffer significant global deformation. Further it was observed that Docol 1400 experienced more prominent cracking at the base of the petals than Docol 600, while Docol 600 allowed for slightly more local deformation.

For the blast tests D6_B1_25 and D6_C1_35 the firing pressure was lower than the desired pressure. This resulted in slightly lower peak pressures, but for the rest of the positive phase the difference from the other tests were negligible. The pressure curves differed slightly between the different configurations and materials. The peak reflected pressure seemed to increase with material strength and cracking of the plates. Also, the peak reflected pressure was shown to be

lower than that of the rigid plates. This difference appeared to increase with increasing firing pressure, which is consistent with the findings of previous work [28]. The whole plate tested at 25 bar, D10_D1_25, seems to be an exception as the peak reflected pressure was almost the same as that for a rigid plate and the midpoint deformation extracted from DIC was almost the same as that for 35 bar.

The reference point deformations illustrate the difference in peak deformations for the different materials, and different pressures. As expected, a higher pressure gives a larger deformation. Moreover, it is seen that the low-strength material experience a larger deformation than the high-strength materials for the same pressure, as they can endure more strain to fracture than Docol 1400. This trend is confirmed by the point clouds of Section 4.4.5, where it was observed that the permanent deformations of Docol 600 were the highest, followed by Docol 1000, and Docol 1400 being the lowest. Another difference between the materials is that the high-strength materials have larger elastic rebound after the peak deformation than the low-strength materials. The elastic rebound makes Docol 1400 oscillate with a higher amplitude than Docol 1000, which in turn has a higher amplitude than Docol 600. The damage of the tests increases with strength of the material.

The plastic hinges travelling from the corners towards the centre of the plates are most evident in the deformation profiles for Docol 1400 and become less pronounced for Docol 1000 and least for Docol 600. This could be due to the fact that work hardening distributes the deformation over a larger area, resulting in the deformations have a shape similar to a global dome.

The plates that had been exposed to ballistic impact, the B configurations, experienced fractures at lower firing pressures than those with pre-formed holes. The only C configuration that developed cracks was Docol 1400 at 35 bar, while all the B tests experienced some sort of crack arrest except for Docol 600 at 25 bar, which only experienced global deformation. There was also a trend that crack propagation was observed to originate from the cracks initiated in the ballistic tests. This indicates that pre-existing damage is detrimental to the plate's resistance against failure during blast loading compared to pre-cut holes. It is also seen that the fractures after blast loading are mostly in the rolling direction of the plate, which may indicate a slight anisotropic behaviour.

5   Numerical Work

5.1   Numerical Simulations

To model the entirety of the shock tube problem was not considered in the scope of this thesis, given the limited time and resources available. Therefore, simplified geometries, loading and boundary conditions were used to investigate the differences in structural response for the various materials and plate configurations.

With the intended outcome to model the combined effect of ballistic impact and blast loading, a restart analysis in LS-DYNA was defined. This made it possible to run a ballistic analysis once for each component and use the permanent changes this impact inflicts on the plate as initial conditions for the blast simulations. Damage, plastic strains, element erosion and temperature

changes from the impact will therefore be accounted for in the blast analysis. The temperature change will not represent the conditions during physical testing as the plates will be at room temperature when placed in the shock tube. This is also the case for any potential remaining elastic response of the plates, after impact at the end of the simulation.

In addition to the restart, a damping function in LS-DYNA was utilised. This made it possible to damp out the energy wave from the impact and thus lowering the simulation time considerably. The plates need to be at rest before performing blast analysis restart in order to replicate the experimental conditions. Total time of the simulations was set to 3.5 ms as this was considered sufficient time to capture the general trend of the plate deformation. Moreover, the crack initiation and propagation in the experiments happened well within this time-frame. Longer simulation time was considered excessive for this thesis as it would involve considerably higher computational times.

Due to the time being set to zero for the physical experiments when the pressure wave is at Sensor 1, and the simulations start when the plate experiences loading, a common time axis for the numerical simulations and physical experiments must be found. Therefore, the time from when the pressure wave reaches Sensor 1 until it reaches the plate must be calculated. Knowing the distance between Sensor 1 and 2 enables the calculation of the pressure wave velocity. The pressure wave velocity is found from Equation (16). Constant velocity near the plate, along with the ideal gas law are assumed to be valid assumptions.

$$u_s = \frac{d_2 - d_1}{\Delta t} \tag{16}$$

u_s is the velocity of the pressure wave, d_1 and d_2 are the distances from Sensor 1 and 2 to the plate, with Δt representing the time it takes the pressure wave to move between the sensors. When both the velocity of the wave and the distance between Sensor 1 and the plate are known, the time it takes for the wave to travel from Sensor 1 to the plate can be found from Equation (17).

$$t_{plate} = u_s \cdot d_1, \tag{17}$$

For the rest of this thesis, the time axis starts when the blast load hits the plate. This means when numerical results are compared to the experimental results, the latter are adjusted with the time t_{plate}.

5.2 Numerical Model

An uncoupled Lagrangian formulation was used, which implies neglection of any FSI effects. As mentioned in the introduction, the plates were modelled using a simplified quarter model. The clamping frame from the shock tube was excluded in the model, which means that the boundaries were modelled as fixed. Only models with a two-axes symmetry were run in this thesis. It has been shown that these simplifications is a satisfactory approach for plates with pre-formed slits[8]. Aune investigated the effect of a simplified model using shell elements for plates with pre-formed holes and found the fixed boundary condition to yield less deflections than a clamped assembly. The good agreement with the experiments was indicated to be due to limited sliding of the supports. The simplified model was able to predict just about the same

damage evolution in the exposed area as the full model and was therefore further used for a mesh sensitivity study of the failure pattern [28]. Solid elements are considered necessary when aiming to describe crack initiation and propagation, although a clamped assembly using solid elements would not be practical for the purpose of this thesis. Therefore, the simulations of the perforation and blast loading of the plates were carried out with a simplified model. The implications of the simplification of the boundary conditions will be investigated in Section 5.3.1.

Figure 5.1a and 5.1b show the plate geometries with measurements, mirrored about the global xz and yz planes. Due to the simplification of using a quarter model, all damage and crack propagation in the plate will be symmetrical about the mirroring planes in the simulations. As a quarter of the plate was used for simulations, also a quarter part of the bullet was modelled. This is pictured in Figure 5.2 in Section 5.2.1.

(a) The plates without pre-formed holes.   **(b)** The plates with pre-formed holes.
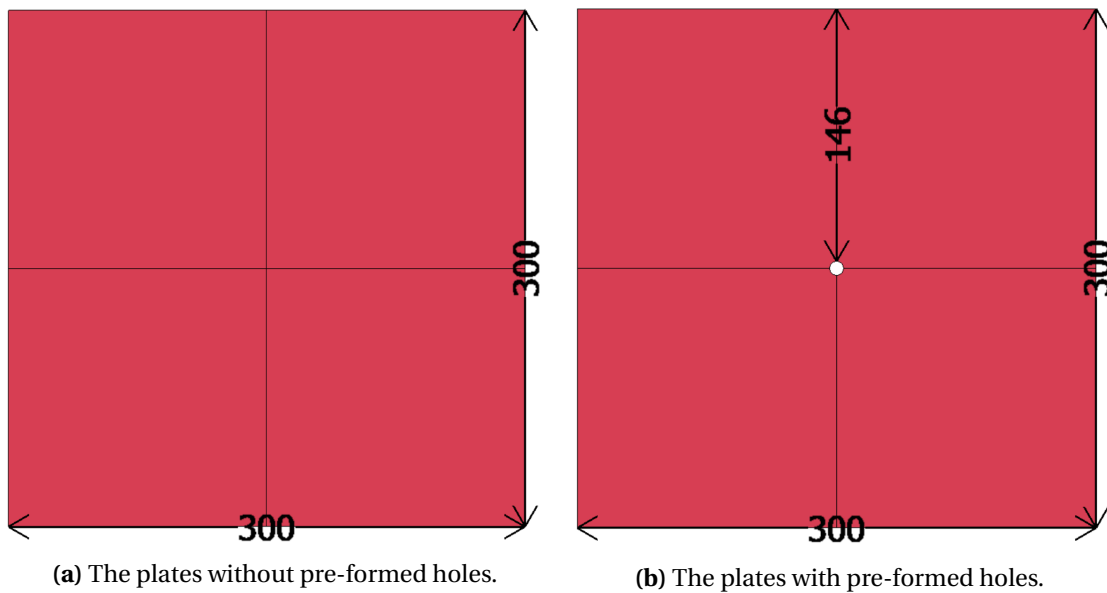
Figure 5.1: The plate models used in the simulations. The plates are mirrored about the xz and yz planes.

5.2.1   The Projectile

The projectile was modelled after the APM2 bullet which is described in Section 4.1.1. Figure 5.2 shows the bullet, which has a much coarser mesh than the target plates. The projectile was assigned analytically rigid properties, meaning that it was of considerably higher stiffness than that of the plate. The deformations of the projectile could therefore be considered negligible. Hald [5] investigated the computational time of simulations with rigid, elastic and elastoplastic bullets and found it to be lowest for the rigid. The elastic and elastoplastic bullets experienced minimal deformations and he therefore modelled the bullet as rigid in any further analyses. Børvik et al. [47] also used a rigid projectile when modelling impact on 15-30 mm thick aluminium plates, as the effect of using a rigid or elastic-plastic projectile was found to be minor when a hardened projectile impacts a much softer target. Thus, an analytically rigid bullet was utilised for the purpose of this thesis. The density of the bullet was found by dividing the

volume of the quarter bullet model by a quarter of the actual mass of the physical bullet. A velocity of 900 m/s was assigned to the bullet and the impact point was set in the origin, or the corner of the quarter model plate.

Figure 5.2: The quarter bullet used in the numerical computations.

5.2.2   Mesh

In the attempt to capture crack initiation and growth, solid elements were chosen for the study. Generally, numerous elements over the thickness are needed to describe the characteristics of ballistic impacts in an accurate way[47]. However, blast loading is, undeniably, a global problem and a very fine mesh would be highly computationally expensive. Consequently, all the plates were modelled with an element size of 0.267 mm, in an attempt to find a compromise between computational cost and accuracy for a combined problem such as this. This corresponds to three elements over the thickness and, naturally, the plates with preformed holes were modelled with the same element size as the plates to be fired upon. The whole plates and the perforated plates therefore consist of 995328 and 946899 elements, respectively. The solid elements are constant stress elements, which are default in LS-DYNA. They use one-point integration, which substantially reduce the computational time compared to 8-point integration, but is prone to hourglass modes. In addition, second order objective stress update is active so as to account for large rotations.

A mesh convergence study is not included in the numerical work. It is recommended using at least three elements over the thickness for solid elements, and further mesh refinement would increase the computational time substantially, given the complexity of the problem at hand. This was therefore deemed beyond the scope of this thesis, but would be recommended for further work.

Figure 5.3 displays the meshing of the plates. The full plates are not presented because the elements were too small to distinguish. However, close ups on the mesh around the hole and the point of impact are presented in Figure 5.3b and 5.3c. For the whole plate, a structured mesh was used for the entire area. The plate with a pre-formed hole was partitioned in order to allow for an unstructured mesh around the hole arc. An unstructured mesh is well suited for handling high-curvature boundaries where a structured mesh could lead to highly deformed elements[48]. The partition lines are in bold black, and outside the boundaries of these lines the mesh is structured.

For the purpose of comparison between experimental and numerical results, the models must allow for data extraction in the same manner as what can be obtained from DIC. Figure 5.4 shows the point of extraction for the reference point and the edge from which the deformation profiles are plotted. The mesh used in 3D-DIC is deactivated around the hole, as shown in Sec-
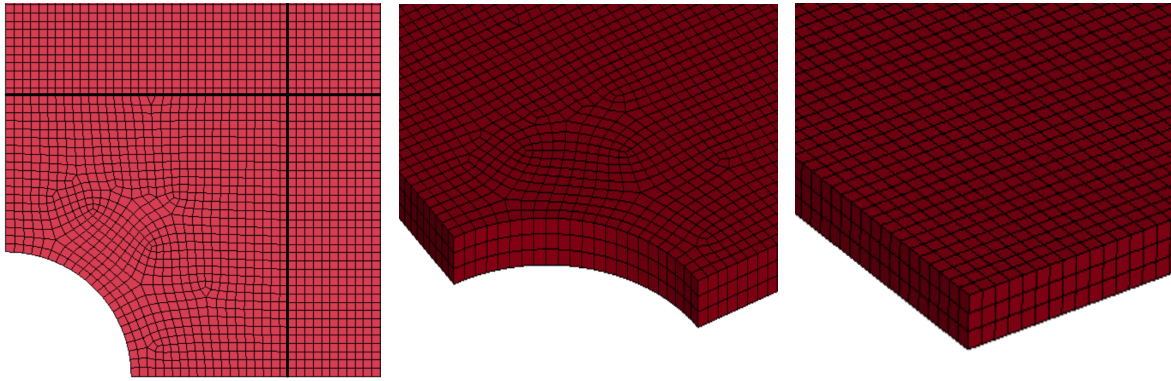
(a) Close up on mesh with partition lines.

(b) Mesh of plate with preformed hole.

(c) Mesh of whole plate.

Figure 5.3: Meshing of the plates. The mesh has an element size of 0.267 mm. Figure (a) shows a close up of the plate with preformed holes with the partition lines in black. Figure (b) and (c) show the solid elements over the thickness for the plate with and without pre-formed holes, respectively.
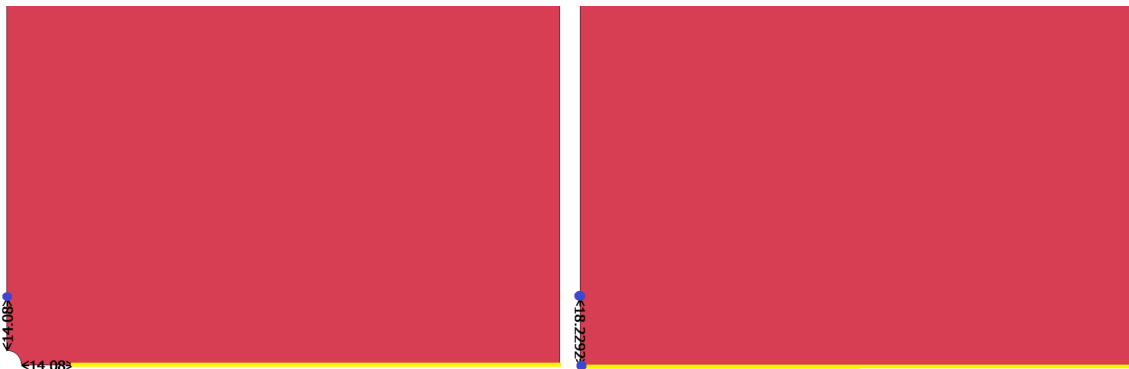
(a) Plate with pre-formed hole.

(b) Whole plate.

Figure 5.4: The reference point is marked as a blue dot and the edge for extracting deformation profiles is marked in yellow.

tion 4.2.1, and the reference point is accordingly taken 18.1 mm from the centre of the plates.

5.2.3   Input Parameters

The plates in the physical experiment are not experiencing any oscillations from the ballistic perforation when they are subjected to the blast load. This is due to the experiments not being performed within seconds of each other, but rather days. To emulate the lacking of oscillations after the perforation, the plate is damped at the end of the ballistic analysis to reduce the simulation time. An alternative method could have been to let the simulation run for several seconds, but this would have increased the simulation run time substantially. Furthermore, only plasticity can dissipate energy in this simulation, so without damping, the elastic oscillations would go on indefinitely. Therefore, Rayleigh mass damping is applied to the plate of the model. The reason behind the exclusion of the bullet is because the Rayleigh mass damping also damps rigid

44

body modes[49]. The purpose of the damping is to reduce the oscillations of the plate without affecting the rest of the simulation. Thus, only low frequency structural modes will be damped. Rayleigh damping's system damping matrix, C is split into mass and stiffness damping[49]:

$$C = \mu M + \lambda K, \tag{18}$$

where M is the system structural matrix, K is the system structural stiffness matrix and μ and λ are the respective damping coefficients. The acceleration is applied to translational and rotational degrees of freedom as

$$\alpha^n = M^{-1}(P^n - F^n - F^n_{damp}). \tag{19}$$

M is the diagonal mass matrix, which is found by a summation of the mass matrix rows[50]. P^n is the external load vector, F^n is the internal load vector, and F^n_{damp} is the force vector because of system damping. It is given as

$$F^n_{damp} = D_s m v, \tag{20}$$

where $D_s = 2\omega_{min}$. D_s is the damping constant for the lowest frequency of interest, ω_{min}[51].

In the ballistic impact simulations, contact between the bullet and the plate was modelled with a contact eroding surface-to-surface algorithm in LS-DYNA. It is common in ballistic impact analyses to set the friction coefficient to zero as this is considered a conservative assumption for the residual velocity of the projectile[47] [52]. A conservative estimate for the objective of modelling in this thesis is considered to be imposing the most damage to the plate during perforation. The static and dynamic coefficients of friction were therefore set to 0.1. Ravid and Bodner suggested a coefficient of 0.1 for metal working and 0.05 for impacts with higher velocities[53]. In addition it has been found that including friction is beneficial for eroding elements in front of the projectile tip, so that they do not become distorted. The residual velocity of the bullet was checked for all the simulations and was found to be less than 1 % lower than the initial velocity, which is in good agreement with the experiments. No self contact in the plate occurred within the window of interest in the blast simulations. If parts of the plate come into contact with one another, it means the plate has opened up too much to be considered a representative model, as the loading would be applied in an inaccurate manner. Such large deformations are beyond the scope of this thesis to model. Therefore, no contact algorithm was included in the modelling of the blast experiments. Energy may be dissipated due to the contact in the ballistic simulation, which is why sliding energy dissipation is computed for the ballistic analyses.

Hourglass modes is an issue for under-integrated elements, such as the solid constant stress element. An hourglass mode is an artificial deformation that occurs when the element is deformed without any work being done on the element. During hourglass deformation, the strain energy is therefore zero[54]. In both ballistic and blast models, hourglass control of the type Flanagan-Belytschko stiffness form with exact volume integration for solid elements is chosen. The hourglass coefficient, which scales the stiffness that counteracts the hour-glassing, is set to 0.01. This is below the value that may give unstable solutions[51]. To keep account of the hourglass energy, it is calculated throughout the simulation.

The critical time step is calculated from the Courant–Friedrichs–Lewy (CFL) time step condition[49]:

$$\Delta t_{cr} \leq \frac{L}{c_d}, \tag{21}$$

which ensures that the time step is sufficiently small to keep information from propagating longer than the length of an element in a time step. L is the characteristic length of an element, which in this case is found from $L = \frac{area}{longest\,side}$. c_d is the speed of sound in the material found from $c_d = \sqrt{\frac{E}{\rho}}$.

Energy data, stresses, strains and the reference point deformations described in Figure 5.4 are saved for each time step. The contour plots which are used to collect the damage, temperature and deformation profiles, also described in Figure 5.4, are only written 20 times throughout the analysis. The times at which the contour plots are written are given by $dt = \frac{endtim}{20}$, where $endtim$ is the end time of the simulation.

As mentioned in Section 5.2 Lagrangian simulations were carried out. The experimental pressure data for the massive plates were used by Aune[28] to fit the Friedlander equation. The obtained loading curves, which were applied in the numerical simulations in this thesis, are presented in Figure 5.5. It should be noted that the figure shows the loading until it reaches zero, while the simulation time was 3.5 ms only. The reader is referred to Aune[28] for further information on the process of the Friedlander fit.
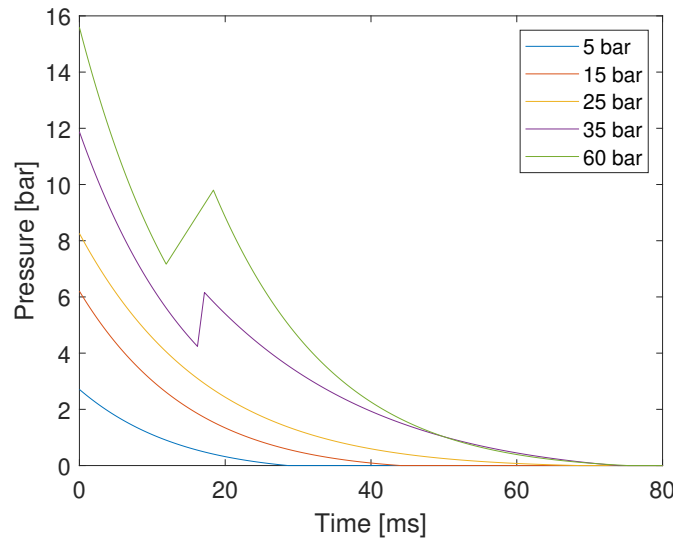
Figure 5.5: The load curves applied to the plates in LS-DYNA. The loading is applied immediately, therefore the curves start at $t = 0$.

The simplified blast loading is applied as a varying pressure load over the entire plate. Consequently, the pressure is always applied normally to the plate, regardless of the plate deformation. This is therefore an uncoupled approach. In the experiment, however, the blast loading is always applied in the same direction and does not follow the movement of the plate. As a result, the load application is known to be overly conservative, and especially so at high deformations[38]. In a coupled method, the fluid and structural sub-domains are coupled using an

46

FSI algorithm. One may model the experiment using different levels of coupling. The higher the level of coupling, the more accurate is the result, but it is more cumbersome to achieve and increases the computational time substantially[20]. This is therefore considered beyond the scope of this thesis.

5.3 Numerical Results

Before the results of the analyses are collected, the energies are checked to ensure that the amount of artificial energy is acceptable. It is found to be well within the acceptable range, as both hourglass energy and damping energy are a thousandth of the internal and kinetic energy. The complete calculations for each configuration is found in AppendixD. Furthermore, it is shown here that the damping energy is less than 10 %, as required from Section 5.2.3.

5.3.1 Effects of Boundary Conditions on Whole Plates

In this section, a parametric study on the effect of boundary conditions (BCs) in the blast simulations will be described. Before the full numerical computations were carried out, some simplifications were made. In particular, the boundary conditions needed to be simplified to reduce the computational time of the simulations. Because the study includes ballistic loading, which requires a solid mesh with a high number of elements through the thickness[32], simplifications of the boundary conditions is preferred. However, this is expected to affect the numerical results, and was therefore investigated.

Three different models were investigated. Firstly, a model with a plate of solid elements and simplified boundary conditions, which was used further in this thesis. A further two models with a plate of shell elements, for the purpose of reducing the computational time of this study, were investigated. The first shell element model has the same simplified boundary conditions as the aforementioned solid element model. This is to examine whether changing from solid to shell element formulation would affect the results severely, ensuring that the parametric study evaluates the different boundary conditions and not the element formulations. In the last model, the element formulation is also of shell elements. Moreover, the boundary conditions are as elaborate as possible and include the full fastening method of the physical experiments of both the clamping plates and bolted connections. The solid element model will be explained further in the subsequent chapter. The shell elements used in the analyses are 1 by 1 mm and of the type Belytschko-Tsay, which is the default in LS-DYNA due to its computational efficiency[51]. As fracture is not expected, playing no part in this pre-study, the element size is found by previous studies to be more than large enough to capture the response purely of the blast loading on the thin plate[7].

The three different models can be seen in Figure 5.6, which are all quarter models. For Docol 1000, simulations were performed for all three models. Because the materials Docol 600 and Docol 1400 are also included in the thesis, though not tested for blast on whole plates, the simulations on these materials were limited to the clamped assembly and the fixed shell model in figures 5.6a and 5.6b. It was expected that the models in figures 5.6b and 5.6c would give almost identical results.

(a) Clamped assembly.   **(b)** Fixed shell element plate.   **(c)** Fixed solid element plate.
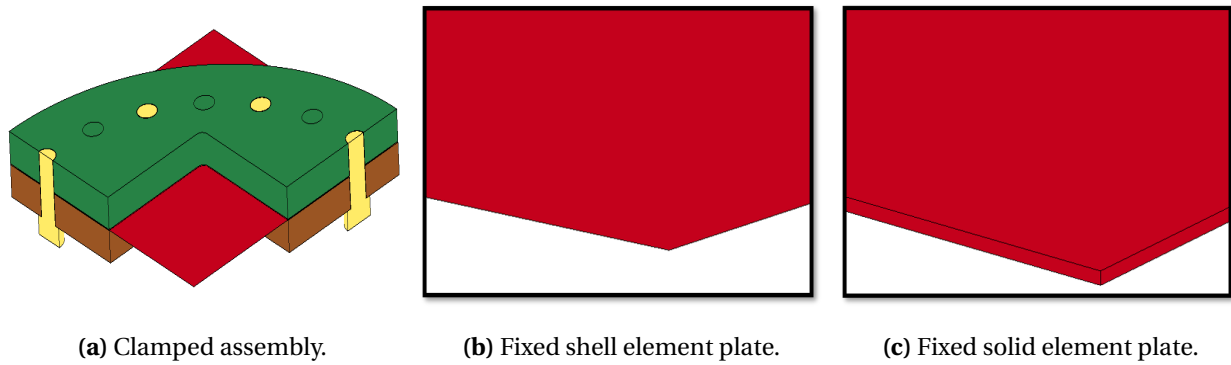
Figure 5.6: The three different models used in the numerical simulations: Figure (a) depicts the clamped assembly with a plate of shell elements. Figure (b) depicts a close-up of the corner of the fixed plate of shell elements. Figure (c) depicts a close-up of the corner of the fixed plate of solid elements.

Firstly, it was validated that the solid element plate model with fixed BCs yielded similar results as the shell element plate model with fixed BCs. The comparison is seen in Figure 5.7a, with the maximum midpoint deformations viewable in Table 5.1. From the figure, it is evident that the behaviour is very similar, as the maximum midpoint deformations differ by at most 3.23 %. It can then be concluded that changing from solid to shell elements has a very small impact on the results, and that the assumption of the previous section still holds. Furthermore, the model with clamped BCs and shell element plate was compared to the model with fixed BCs and shell element plate in Figure 5.7b. All maximum reference point deformations with their respective differences can be seen in Table 5.1.
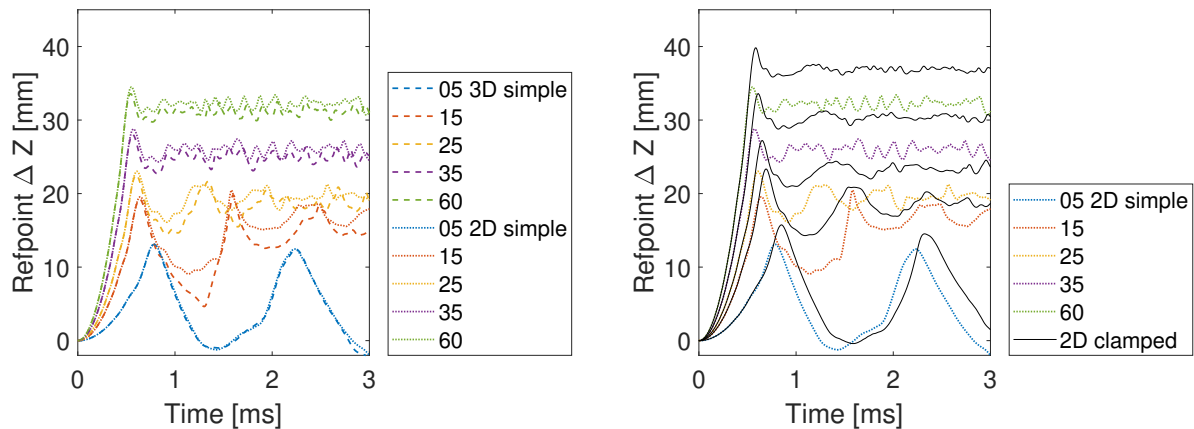
(a) Comparison of solid element and shell element plate models with otherwise identical set-up.   **(b)** Comparison of simple and clamped boundary conditions of shell element plate.

Figure 5.7: Firing pressures of 5, 15, 25, 35 and 60 bar are included. 'Simple' denotes that the boundary conditions are fixed in all translational directions, and 'clamped' means that the entire clamping assembly is included in the model. The clamped results are in black solid lines, whereas the simple BCs results are in coloured, dotted lines. The coloured dashed lines represent the solid element model, which also has fixed boundary conditions. The solid, coloured lines represent the experimental results. '3D' is here representing the model with a plate of solid elements, and '2D' a plate of shell elements.

Table 5.1: Difference in maximum midpoint deformation for whole plates of Docol 1000 with different set-up in LS-DYNA. '3D' refers to a model where the plate is modelled with solid elements, and '2D' to a model where the plate is modelled as shell elements. 'simple' means that the BCs are simplified to be fixed in all translational directions. 'Clamp' means that the model includes an assembly were the actual fastening method is modelled. The columns that start with 'Diff.' give the percentage difference between the two following values. All measurements are in mm.

Test	3D simple	2D simple	Diff. 2D simple to 3D simple	2D clamp	Diff. 2D clamp to 2D simple
D10_D_05	13.07	13.09	0.15 %	15.75	20.32 %
D10_D_15	19.84	20.48	3.23 %	23.36	15.38 %
D10_D_25	22.54	23.04	2.22 %	27.23	18.19 %
D10_D_35	28.03	28.78	2.68 %	33.61	16.78 %
D10_D_60	33.57	34.50	2.77 %	39.82	15.42 %

The simulations for D600 and D1400 an be seen in Figure 5.8 and 5.9, respectively. These were split into three to ease interpretation of the plots. 5 and 15 bar firing pressure results are in Figure(a), 25 and 35 bar are in Figure(b), and 60 bar is in Figure(c). The y-axis limit was set to 60 mm for all plots to make visual inspection between the materials easier. From the figures, the same trend is seen as for Docol 1000, in particular that the clamped assembly yields higher deformations than the model with fixed BCs and shell elements. Rakvåg et al. found it important to model the boundary conditions of the plates with a sufficient degree of accuracy in order to capture the straining around the bolts in the experiments. Due to the thin nature of the plates, they are required to carry the load through membrane forces [6]. The same assumption would apply to the plates in this thesis. The exact maximum deformations for both materials and the difference between them can be seen in Table 5.2. It is evident that the difference in displacement between the model with clamped assembly and the model with fixed BCs and shell elements is least for D6 and highest for D14, with D10 in between.

(a) 5 and 15 bar firing pressure. **(b)** 25 and 35 bar firing pressure. **(c)** 60 bar firing pressure.
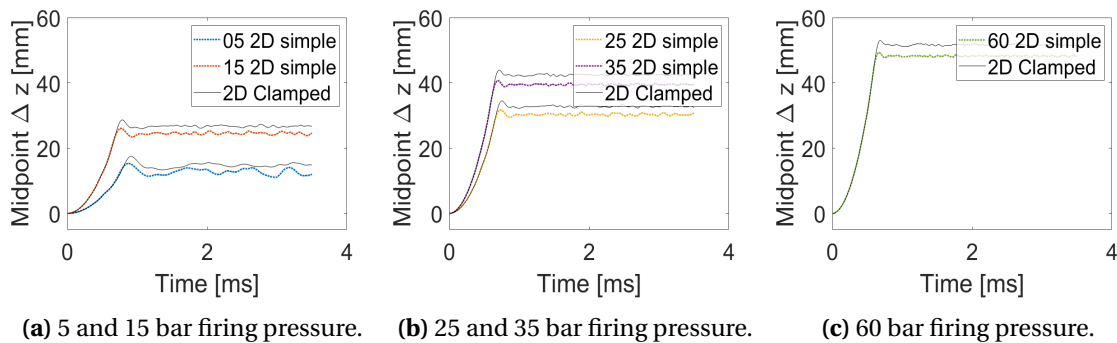
Figure 5.8: Comparison between model with clamped assembly and plate of shell elements and model with fixed BCs and plate of shell elements for D600. '3D' is here representing the model with a plate of solid elements, and '2D' a plate of shell elements.

49

(a) 5 and 15 bar firing pressure. **(b)** 25 and 35 bar firing pressure. **(c)** 60 bar firing pressure.
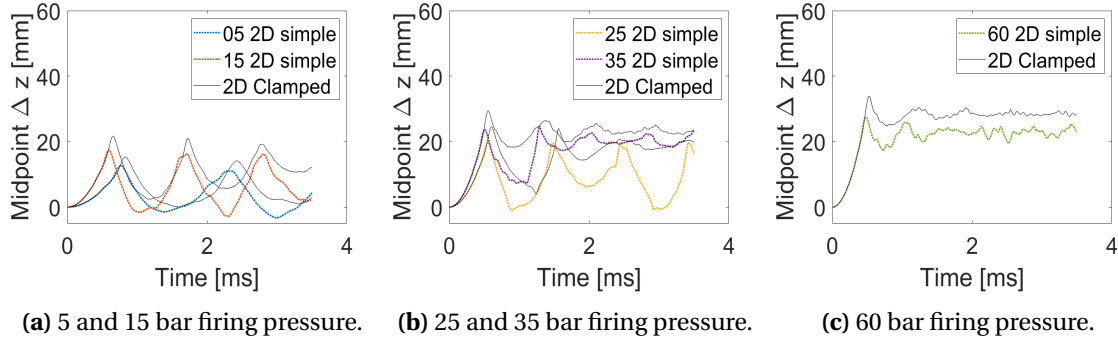
Figure 5.9: Comparison between model with clamped assembly and plate of shell elements and model with fixed BCs and plate of shell elements for D1400. '3D' is here representing the model with a plate of solid elements, and '2D' a plate of shell elements.

Table 5.2: Difference in maximum mid point deformation for whole plates of Docol 600 and Docol 1400. '2D' refers to a model where the plate is modelled with shell elements. 'simple' means that the BCs are simplified to be fixed in all translational directions. 'Clamp' means that the model includes an assembly were the actual fastening method is modelled.The column Diff. 2D clamp to 2D simple gives the percentage difference between the clamped and the simple BCs for the shell plate models. All measurements are in mm or %.

Test	2D simple	2D clamp	Diff. 2D clamp to 2D simple
D6_D_05	15.31	17.47	14.11 %
D6_D_15	26.06	28.65	9.94 %
D6_D_25	31.70	34.48	8.77 %
D6_D_35	40.70	43.92	7.91 %
D6_D_60	49.32	53.04	7.54 %
D14_D_05	12.69	15.36	21.04 %
D14_D_15	17.43	21.68	24.38 %
D14_D_25	19.77	24.52	24.03 %
D14_D_35	24.81	29.42	18.58 %
D14_D_60	27.46	33.88	23.38 %

It has been shown that the model with fixed boundary conditions and shell elements is able to represent the model with fixed boundary conditions and solid elements. Furthermore, a difference was found between the materials, where the fixed boundary conditions had a more prominent effect on the high-strength materials D1000 and D1400, opposed to the low-strength material, Docol 600. Consequently, the difference between numerical displacements and experimental results for perforated plates of D1400 are expected to be higher compared to D600 when implementing simplified boundary conditions. In other words, D1400 is likely to deviate the most, being the least ductile material.

5.3.2 Performance of the Numerical Models

In Table 5.3, some representative run times are listed along with the smallest time step of that simulation and the number of cores used. The simulations that used 12 and 8 cores were run on an external cluster provided by the Department of Structural Engineering at NTNU, whereas the simulations run on 4 cores were done so on a laptop with 8GB RAM and Intel Core i7-8550U. Moreover, it is seen that the simulation of the C configuration test has a time step roughly four times larger than the same simulation of B configuration, and runs significantly faster despite only using 8 cores. This is an expected outcome as the C simulations are not damaged from a previous ballistic simulation and so have no distorted elements when the simulation begins. The critical time step will decrease as the element size increases, as seen from Equation (21).

Furthermore, the B configurations also need to run the ballistic impact before blast loading is applied, which can take roughly 4 hours on 12 cores. Lastly, it is seen that the model with shell element plate and simplified BCs has the shortest simulation time by a significant margin of only 5 minutes, whereas the full assembly with clamped BCs and shell element plate has a simulation time of 36 minutes. By changing from simplified to clamped BCs, the simulation time is increased seven-fold when shell element plates are used. With this information, it can likely be deduced that running a model with a solid element plate and fully clamped assembly would take several weeks, which would be unviable.

Table 5.3: Run times in LS-DYNA for a selection of the simulations. The first simulation is of the ballistic impact loading before restart. The simulations between the first and second dashed lines are all of the basis model with solid elements and fixed BCs. The simulation below the second dashed line is of the model with shell element plate and fixed BCs. The simulation below the third dashed line is of the model with shell element plate and fully clamped assembly.

Simulation	Smallest time step [s]	Run time	Cores	Nr. of elements
D14 ballistic	3.6778E-08	3 hours 55 minutes 13 seconds	12	995600
D10_B1_25	5.3901E-09	70 hours 51 minutes 55 seconds	12	995328
D10_C1_25	2.1592E-08	21 hours 45 minutes 18 seconds	8	946899
D10_D1_35	3.6778E-08	21 hours 36 minutes 32 seconds	8	995328
D10_35 2D fixed	1.6599E-07	0 hour 5 minutes 14 seconds	4	22500
D10_35 2D clamped	1.6599E-07	0 hour 36 minutes 0 second	4	61734

The parameter study in Section 5.3.1 showed that the fully clamped assembly gave the closest representation of the deformation of the experiments. A deviation in deformation between the experimental results and the computational results from the model with fixed boundary conditions and plate of solid elements must therefore be expected. As described in Section 4, in addition to the experiments on plates with holes, blast waves of initial intensity of 5, 15, 25, 35, and 60 bar were exerted on whole plates of Docol 1000. These results are presented in Figure 5.10. Experiments on 0.8 mm thick plates of type Docol 600 and Docol 1400 have been conducted in previous work but, as these would have been of a different material batch, the results were not included for comparison. The difference between the experimentally obtained maximum deflections and the numerically predicted deflection for the simplified solid element model and

the shell element clamped assembly is presented in Table 5.4. It is seen that the model with solid element plates and fixed BCs has a consistently lower deformation than the experimental results.

For the lower pressures, the oscillations are excessive in the numerical simulations. This is consistent with the findings of Elveli et al.[11] on perforated plates of Docol 600 and Docol 1400. At 5 bar the plate does not appear to reach any permanent deformation in the simulation time. The experimental maximum deflection is also considerably higher than what could be expected from the numerical simulation, yielding the highest difference in percentage. For 15 bar and 35 bar the simulations and experiments seem to converge towards similar permanent deformations, while for 60 bar and 25 bar the deformations are considerably underestimated. There were, however, raised questions about the test at 25 bar previously in Section 4.2.1, so comparison involving this test should be handled with care.

Figure 5.11a shows a comparison of the displacement histories for the D10_D1_35 test for the three different numerical models treated in this section against the experimental result. It can be seen that the model with clamped boundary conditions is closest to the deformation pattern seen from the experiments. This observation is supported by Figure 5.11b, where the experimental results are plotted together with the deformation of the clamped model for all firing pressures.
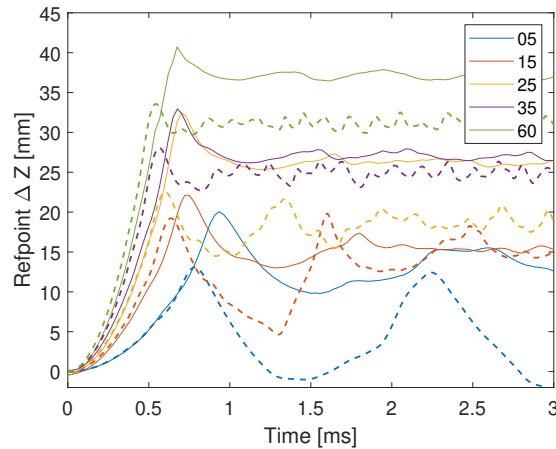
Figure 5.10: Comparison of midpoint displacements of whole plates of Docol 1000 DP. The dashed lines are the numerical results using the simplified BCs with a plate of solid elements, and the continuous lines are the experimental results.

52
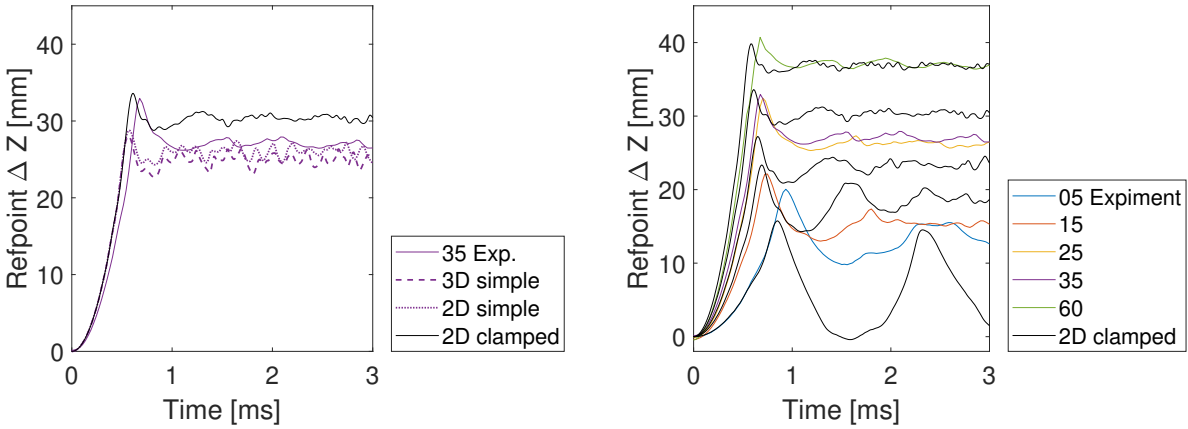
(a) All models for 35 bar firing pressure, including the experimental results for 35 bar.

(b) Shell element plate model with clamped BCs compared to experimental results.

Figure 5.11: Clamped assembly results are in black solid lines. Simple BCs results are in coloured dotted lines and the coloured dashed lines represent the solid element model, with fixed BCs. The solid coloured lines represent the experimental results. '3D' is here representing the model with a plate of solid elements, and '2D' a plate of shell elements.

Table 5.4: Difference in maximum mid point deformation for whole plates of Docol 1000 from experiments to numerical results. '2D' refers to a model where the plate is modelled as shell elements. '3D' refers to a model where the plate is modelled with solid elements. 'simple' means that the BCs are simplified to be fixed in all translational directions. 'Clamp' means that the model includes an assembly were the actual fastening method is modelled. As before 'Diff.' gives the difference in percentage between the two following values. All measurements are in mm or %.

Test	Exp.	Diff. exp. to 3D simple	Diff. exp. to 2D clamp
D10_D_05	20.05	53.40 %	27.30 %
D10_D_15	22.13	11.54 %	−5.27 %
D10_D_25	32.44	49.92 %	19.13 %
D10_D_35	32.95	17.55 %	−1.96 %
D10_D_60	40.71	21.27 %	2.24 %

As mentioned in Section 5.2.3, the contour plots for extracting deformation profiles are only written 20 times throughout the simulation. Therefore, the deformation profiles can only be plotted for a limited number of time frames. The four states, presented in Figure 5.12, were chosen as a result. The comparison to experiments was made based on maximum deformation in a similar manner as in Section 4.4.3. The states represent varying percentage of maximum deformation for the different simulations as the states are set at certain times. Consequently, the plots were labelled with "State 1" through "State 4". Corresponding frames to extract deformation profiles from 3D-DIC were calculated to yield the same percentage of experimental maximum deformation as the states used in the numerically obtained maximum deflection. Deformation profiles were extracted from 3D-DIC in the same manner as in Section 4.2.2. As

there is also a limited number of frames available for DIC, there may be minor deviations in the deformations compared to maximum deformation.
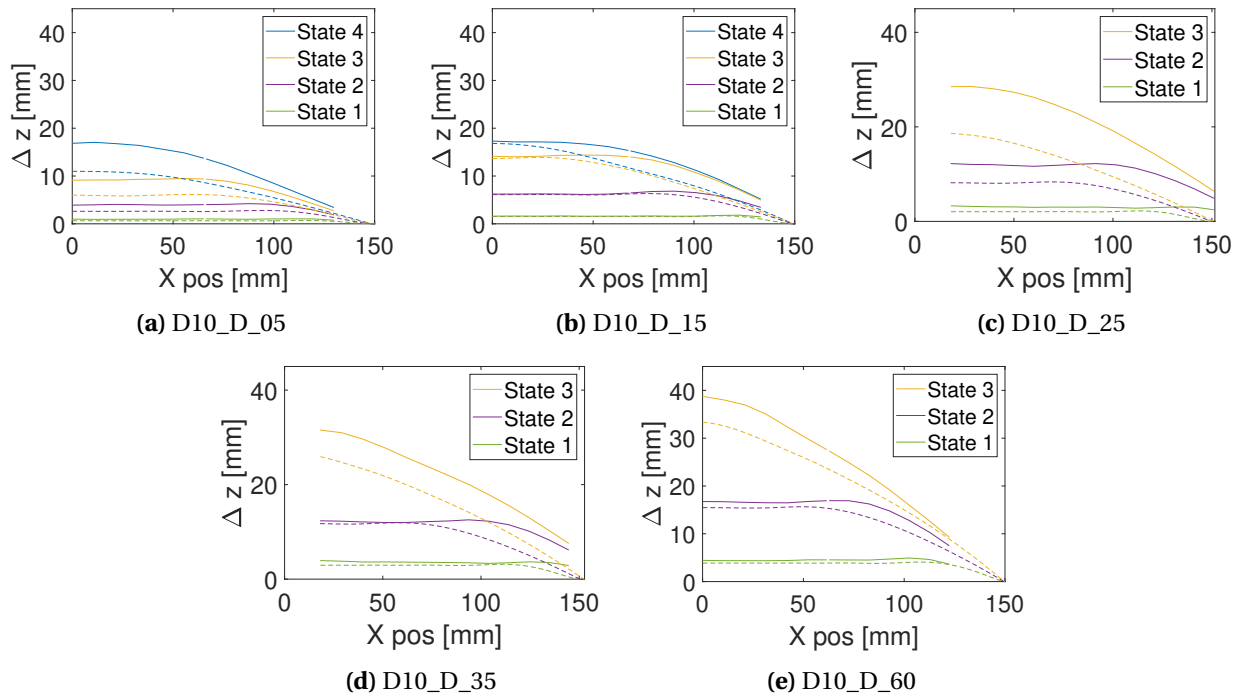
Figure 5.12: Comparison of D1000 whole plate profiles. The dashed lines are the numerical results and the continuous lines are the experimental results. State 1, 2, 3, and 4 represent different deformation states compared to maximum deformation. For instance, State 1 of the numerical results and the experimental results will be at the same percentage of their maximum deformation.

For State 4 the maximum deformation has already been reached at pressures 25 bar, 35 bar and 60 bar. The deviation between numerical and experimental results naturally increases from State 1 to State 4 because the maximum deformations are larger for the experimental than the numerical results. The difference between the same percentage of the maximum deformations increases as the percentage increases. Figure 5.12d and 5.12e illustrate this clearly. The travelling plastic hinge is less visible in the simulation profiles than those extracted from DIC.

These simulations highlight some important aspects concerning the numerical model, which should be kept in mind when considering the results for the plates exposed to ballistic impact and plates with pre-formed holes. The solid element model with fixed boundary conditions seems to underestimate the global deformations of the plates and oscillates to a greater extent. It has been shown that the boundary conditions affect the displacement to a various degree for the three materials. In addition, the chosen material model and the strain rate sensitivity may influence the results. A clamped assembly using shell elements predicts the displacement histories of the experiments more accurately. However, using shell elements to describe the combined effect of ballistic impact and blast loading is not suitable, and using a clamped model with solid elements would be highly computationally expensive. Therefore, the simplified solid element model is, based on these results, presumed to be a representative model given the re-

sources and time available.

5.3.3 Reference Point Deformations for Perforated Plates

In this section, the numerically obtained deformations from the tests on perforated plates are presented, i.e. the C and B configurations. The numerical model with fixed BCs and solid element plate is used in the following. Figure 5.13 shows the deflection of the reference point in the simulations for both configurations. The fracture point is marked and the deformation curve cut off thereafter. The maximum deformations of the D600 plates seem to be in good agreement with the experiments. As previously discussed, the simplified boundary conditions yield lower deformations than a clamped assembly, but this effect was shown to be less significant for D600. Neglecting FSI effects typically increases the deformations compared to a coupled approach [28]. Therefore, the good agreement between the simulations and experiments may come as a result of a circumstantial synergy between these two factors. Fracture for D6_B1_35 also occurs at similar times and deformations. As for the whole plates, the deformation is underestimated for D1000 and fracture happens a little early compared to the tests. This is also the case for the D1400 plates. D14_C1_25 also experiences total failure, while no crack initiation was obtained in the experiment.

(a) C1_25

(b) C1_35

(c) B1_25

(d) B1_35
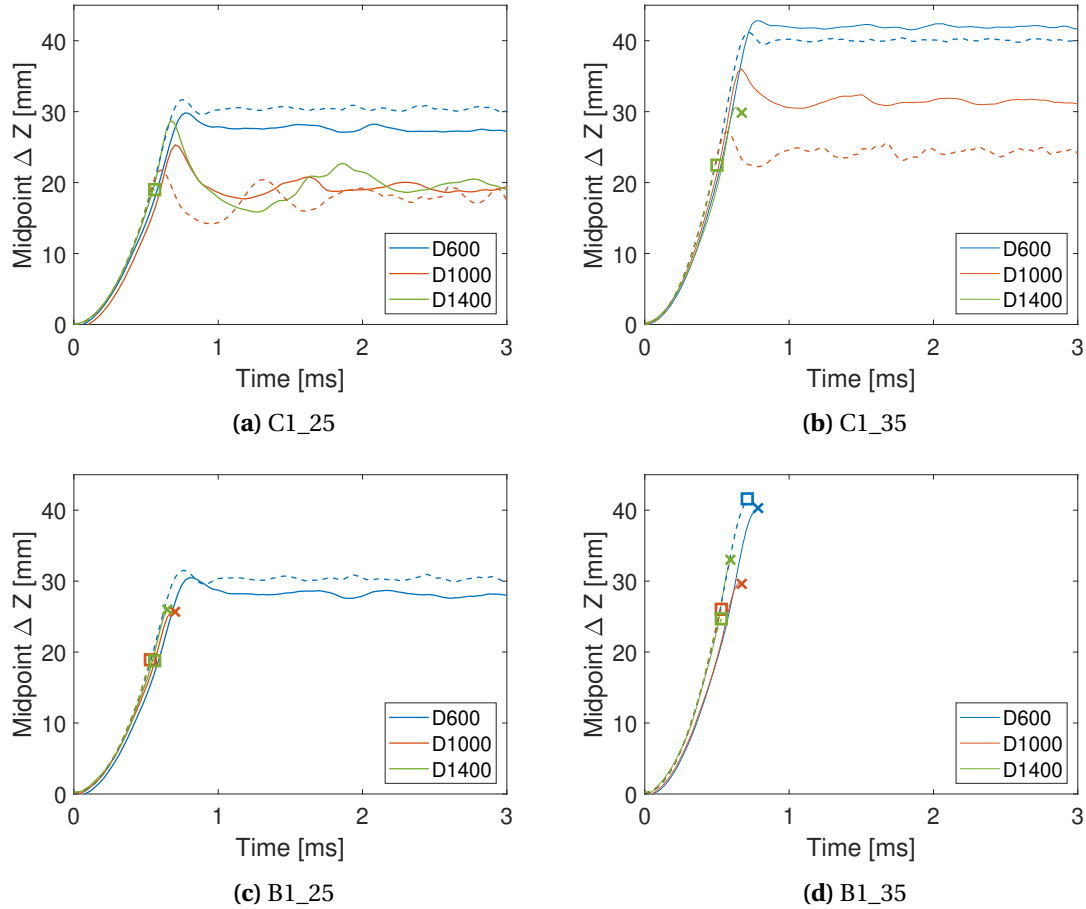
Figure 5.13: Comparison of reference point deformation for plates of B and C configuration. The dashed lines are the numerical results, and the continuous lines are the experimental results. × represents the point of fracture for the experimental results, and □ represents the fracture point of the numerical results.

5.3.4 Damage on Perforated Plates

In the following figures, the crack propagation of the failed plates are shown. The model is mirrored about the symmetry axes in all pictures. The contour plots are of the damage variable from LS-DYNA. Damage accumulation after ballistic impact for the B configurations is shown in Figure 5.15. The difference between the response is evident for the three materials. For D1400, the petals are torn all the way to the base, yielding larger and more clearly divided pieces than for D600. It can be seen from the results, after ballistic impact, that for all the materials the crack initiation happens at the two edges of the quarter model that are used for symmetry. This is the area with the highest level of damage. The cracks are slightly larger for D1000 than for D600 and D1400. However, D1400 experiences a larger area of damage close to the critical value at the base of the petal formation. From Figure 5.16 to Figure 5.19 the full plate at the last time frame to the left and a close up on the hole to the right are presented. However, all the Docol 1400 plates experience total failure and the last time frame is therefore not presented. The full plate is included for a a series of time frames, from crack initiation to close to complete tearing of

the plate at the supports. These are shown from Figure 5.20 and 5.23. As mentioned in Section 5.2, utilising symmetry in the simulation implies that any cracks in the experiments which are unsymmetrical about the in plane axes cannot be replicated.

Labelling the cracks was done in the same way as for the experimental results in Section 4.4.6. An example is shown in Figure 5.14. The plate response and failure modes with measured crack lengths from LS-DYNA are presented in Table 5.5.
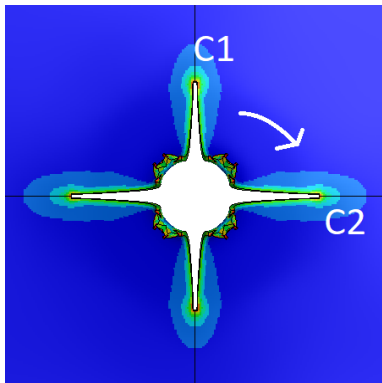
Figure 5.14: Damage contour of D10_B1_25 with system for crack numeration.

Table 5.5: Failure modes and plate response for all simulations, including crack lengths where applicable. C1 and C2 denotes the fractures of each plate following the notation used in Figure 5.14

Test	Mode	C1 [mm]	C2 [mm]
D6_C1_25	Global deformation	-	-
D6_C1_35	Global deformation	-	-
D6_B1_25	Crack arrest	7.7	-
D6_B1_35	Crack arrest	39.89	-
D10_C1_25	Global deformation	-	-
D10_C1_35	Global deformation	-	-
D10_B1_25	Crack arrest	11.05	12.6
D10_B1_35	Crack arrest	31.18	42.62
D14_C1_25	Total failure	-	-
D14_C1_35	Total failure	-	-
D14_B1_25	Total failure	-	-
D14_B1_35	Total failure	-	-

(a) D600

(b) D1000

(c) D1400
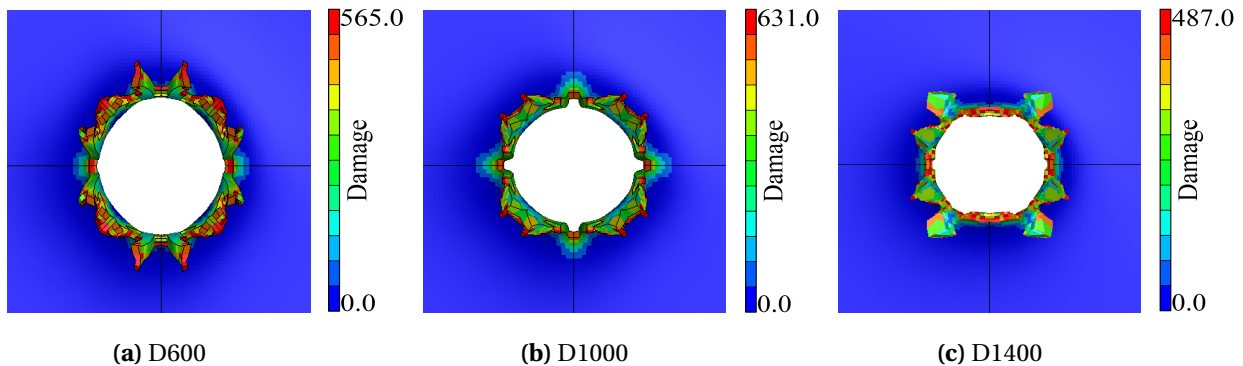
Figure 5.15: Close up on area of perforation after numerical simulation of ballistic impact.

(a) Full plate view.   **(b)** Close up.   **(a)** Full plate view.   **(b)** Close up.
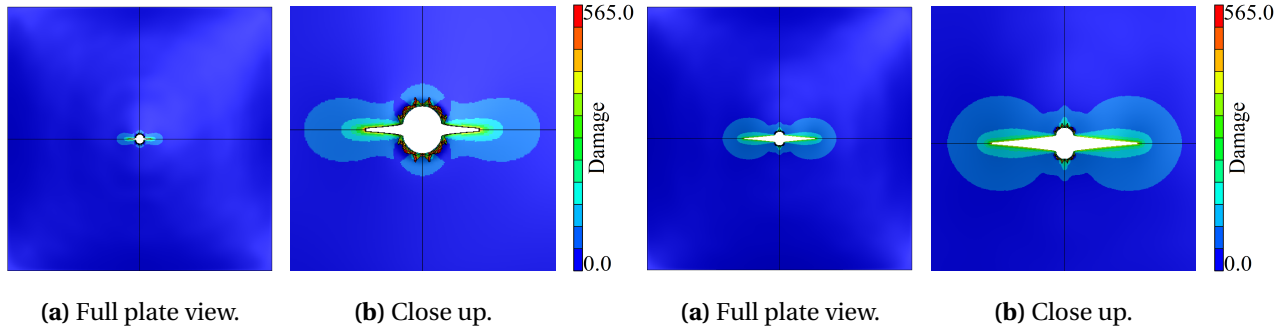
Figure 5.16: Perforation of D6_B1_25 after numerical simulation of ballistic impact.   **Figure 5.17:** Perforation of D6_B1_35 after numerical simulation of ballistic impact.

Both of the blast simulations for D600 with B configuration experience fracture along the horizontal edge of the plate. These were areas with a high level of damage after ballistic impact, as seen in Figure 5.15a. The D6_B1_25 experiment did not have any crack propagation after the blast, while D6_B1_35 experienced minor cracking. The simulation gave almost 8 times the crack length compared to that observed experimentally.

(a) Full plate view.   **(b)** Close up.   **(a)** Full plate view.   **(b)** Close up.
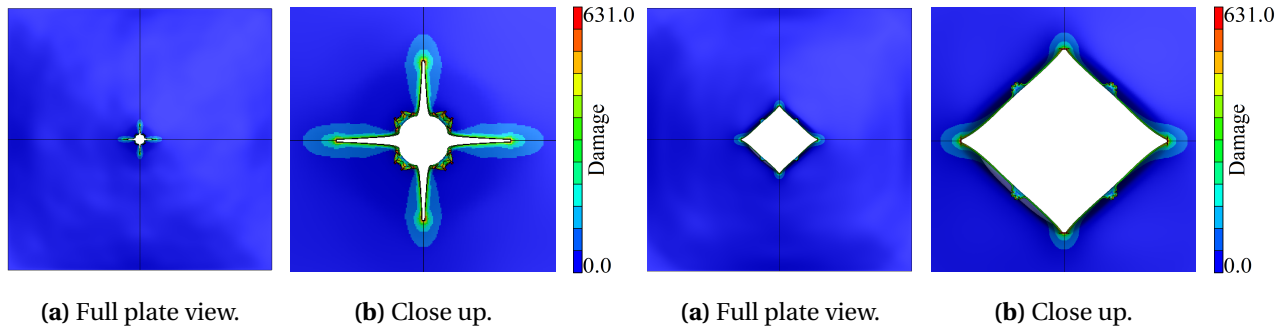
Figure 5.18: D10_B1_25 after numerical simulation of blast loading.   **Figure 5.19:** D10_B1_35 after numerical simulation of blast loading.

The simulations of the D1000 plates that had been subjected to ballistic impact led to larger cracks both along the vertical and horizontal edges of the plate. These were also the most affected areas at the base of the petals after ballistic impact. The crack lengths of D10_B1_25 are similar to those in the experiment, where C2 is twice the length. For D10_B1_35 the cracks are arrested, but the hole has opened completely, resembling a square slit. At this point, it should here be noted that the simulations are uncoupled and, therefore, make the assumption that the pressure is unaltered by the plate deformations. When the plate opens up, as in Figure 5.19, the numerical simulation conditions deviate from the physical as the load is always applied normally to the plate. This will increase the deformations as the pressure pushes the plate, while in the experiment it would have been allowed to pass into the dump tank, reducing the load.

(a) $t = 0.71ms$ **(b)** $t = 1.41ms$ **(c)** $t = 2.12ms$
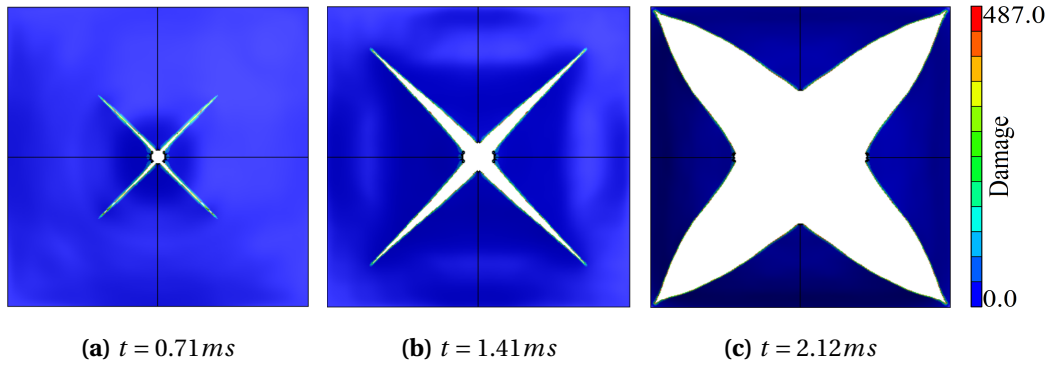
Figure 5.20: Numerical results of blast loading of D14_B1_25 at different simulation times. The contour plots are of the damage.

(a) $t = 0.53ms$ **(b)** $t = 1.41ms$ **(c)** $t = 1.77ms$
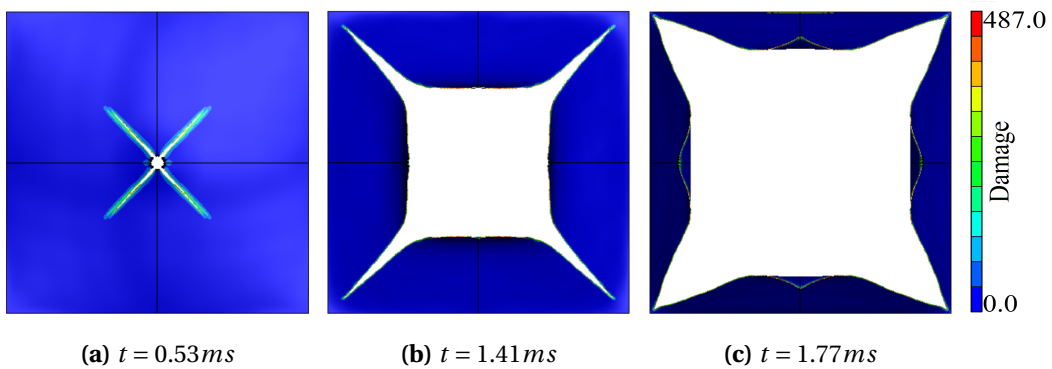
Figure 5.21: Numerical results of blast loading of D14_B1_35 at different simulation times. The contour plots are of the damage.

(a) $t = 0.71ms$ **(b)** $t = 1.41ms$ **(c)** $t = 2.12ms$
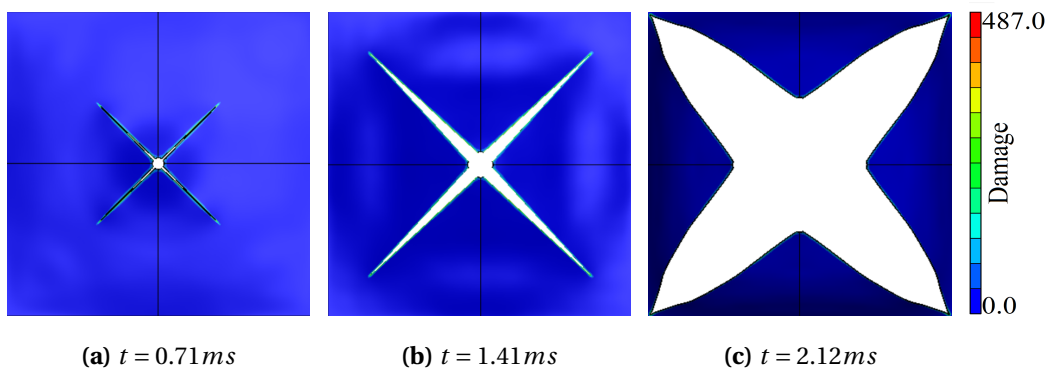
Figure 5.22: Numerical results of D14_C1_25 at different simulation times. The contour plots are of the damage.

59

(a) $t = 0.53\,ms$ **(b)** $t = 1.41\,ms$ **(c)** $t = 1.77\,ms$
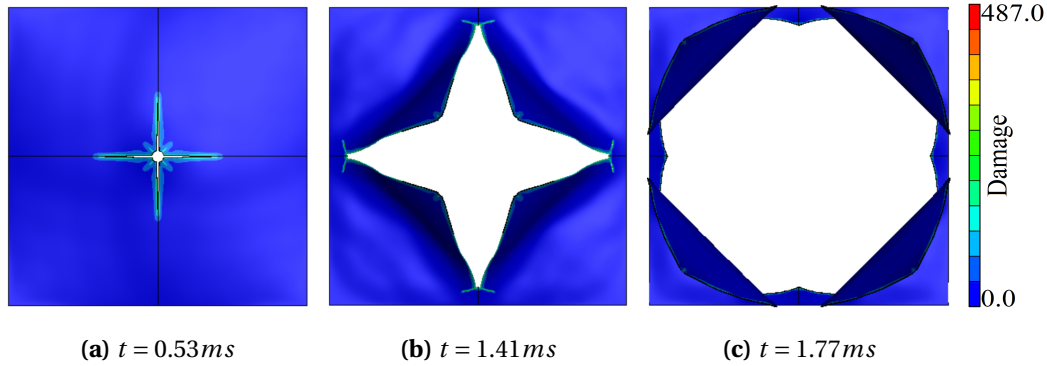
Figure 5.23: Numerical results of D14_C1_35 at different simulation times. The contour plots are of the damage.

As mentioned, all the D1400 simulations led to total failure of the plate. This could be a consequence of the numerical loading application or the calculated fracture parameter being inaccurate. Both B configurations fail along the diagonal. D14_B1_35 also fails completely in the experiment. From Figure 5.20 to Figure 5.23 the crack propagation for three time frames is shown. Different frames were chosen for 25 and 35 bar firing pressure as frame of first fracture and total failure varied for the simulations. The crack propagation in the D14_C1_25 simulation is excessive compared to the experimental results, which yielded only global deformation. The crack initiation in the 35 bar simulation is along the vertical and horizontal edges. However, the crack propagation does not continue all the way to the boundaries, as the pressure pushes the centre of the plate to such a degree that the plate tears again. This can be seen in Figure 5.23 and is illustrating a case for which an uncoupled approach is unsuited. In order to describe the behaviour of plates after considerable deformation, a coupled FSI simulation should be used. This is not in the scope of this thesis. It is noted that the simulations yield conservative results considering crack length for all materials and configurations.

5.4 The Effect of Strain Rate Sensitivity in Blast Loading

As mentioned in Section 3.2, a small parametric study was conducted to investigate the influence of the choice of the strain rate sensitivity parameter. As Docol 1000 has not been tested as extensively as Docol 600 and Docol 1400, the authors were not able to find the strain rate sensitivity constant, c in the literature. Therefore, the whole plate model was used to run simulations for c values of 0.01, 0.007 and 0.004. The values of 0.01 and 0.004 are the strain rate sensitivity constants for D600 and D1400, respectively, and 0.007 is the average of the two. The resulting midpoint displacements are presented in 5.24. The pressure was chosen as 35 bar.
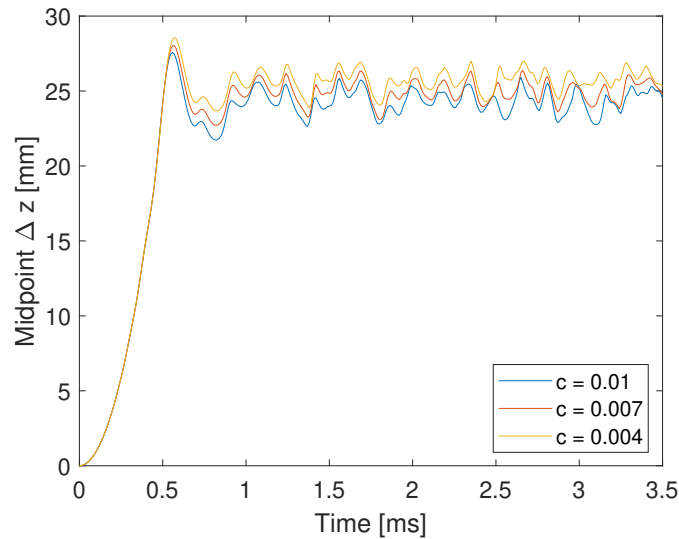
Figure 5.24: Midpoint deflection of whole plates of type D1000 for different values of the strain rate sensitivity constant, c.

For the purpose of choosing c, the minor differences between the displacement curves indicate that the choice is not of major importance for the results of blast loading. Rate dependency usually increases with strain rate [25]. When the strain rate increases, the heat does not have time to dissipate, which results in an elevated temperature. As the temperature increment in the simulation is low, which can be seen in Figure 5.25, this indicates that the strain rates are relatively small and the negligible difference of 1 mm maximum displacement could be expected. Thus, $c = 0.007$ was chosen on the basis of global response and that the response of Docol 1000 generally seems to lie in between the two other materials.

Figure 5.24 shows that deformation increases for smaller values of c. Rakvåg et al. [6] conducted split Hopkins tests on Docol 600 and found the strain rate sensitivity to be dependent on the level of plastic straining. This phenomenon is not captured by the modified Johnson-Cook constitutive model, as a constant value for the rate sensitivity is assigned. Different values are needed to fit the experimental data for a constant reference strain rate.

Contour plots of the effective plastic straining from the simulations with different values of c are shown in Figure 5.26. The level seemed to increase with a decreasing rate sensitivity, which is consistent with the findings of Rakvåg et al. The differences were found to be minor. Total plastic straining was also modest, with only a small area in the middle of the plate exceeding 2.5 %. The small increase in displacement for lower values of c might be due to this slightly increased level of plastic straining. Hald [5] investigated the influence of the strain rate sensitivity parameter for perforated plated of type Docol 600 and Docol 1400 which did not experience fracture. He found the plastic strains to be considerably higher for Docol 600 than for Docol 1400. This was expected as D600 is a more ductile material. Almost no difference in displacement history for the given D1400 test was observed, while there were minor deviations for the D600 test. It should be emphasised that the parametric study described in this section has been conducted for blast loading on whole plates, which is a highly global problem with moderate strain rates and limited plastic straining. The strain rates in a ballistic impact could be considerably higher

61

and so the response of the material would vary more. Additionally, in a localised problem such as crack initiation and propagation, the viscoplasticity would likely influence the response to a greater degree. Taking this into consideration, the c parameter should be calibrated by conducting tensile or compression tests at a range of temperatures and strain rates[25]. However, this is beyond the scope of this thesis.
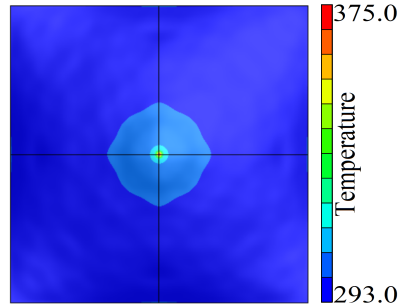
Figure 5.25: Temperature contour of the D10_D1_35 plate for $c = 0.007$

(a) $c = 0.01$ (b) $c = 0.007$ (c) $c = 0.004$
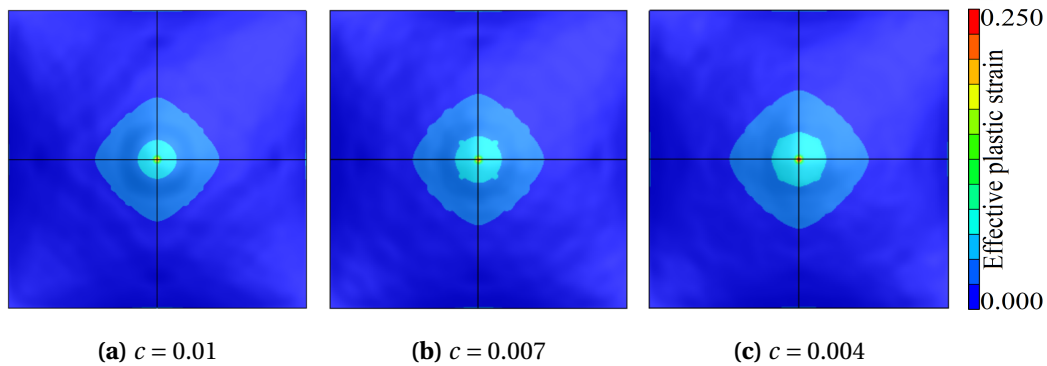
Figure 5.26: Plastic strain contour of D10_D1_35 for different values of c.

5.5 The Cockcroft-Latham Fracture Parameter's Effect on Fracture

From the numerical results for the perforated plates, it was observed that fracture in the simulations was exaggerated compared to what was observed in the experimental tests. Motivated by these results, a small study on the influence of the Cockcroft-Latham fracture parameter was conducted. It is emphasised that the purpose of the study is not to replicate the experiments in an exact manner, but rather investigate the influence of the fracture parameter, especially in regard to failure modes. Three tests were chosen for the study. These were D10_B1_25, D14_C1_25 and D14_C1_35. It was desired to use both configurations as well as plates that had experienced different responses in the experiment. Therefore, both D14_C1_25 and D14_C1_35 were used, as the first had no crack initialisation, while complete failure was predicted numerically for the last.

It was decided that two larger values of W_c should be used. As shown in Figure 3.4a in Section 3.4 a small increase in extraction time, or a small increase in strain at fracture, yields a large

difference in accumulated damage. This indicates that if point of fracture is changed to a small degree, this may result in a significant difference in the value of W_c.

In Figure 5.27, 5.28 and 5.29 the damage contour plots are presented for the three tests. The value of W_c is set as the maximum range of the colour bars to make it apparent which value was used. The unit is MPa. For D10_B1_25, the original simulation is also included as the cracks were arrested, unlike for D14_C1_25 and D14_C1_25. It should be noted that the pictures are not to scale, and the plate response and measured crack lengths are therefore presented in Table 5.6.

(a) Original value. **(b)** Middle value. **(c)** High value.
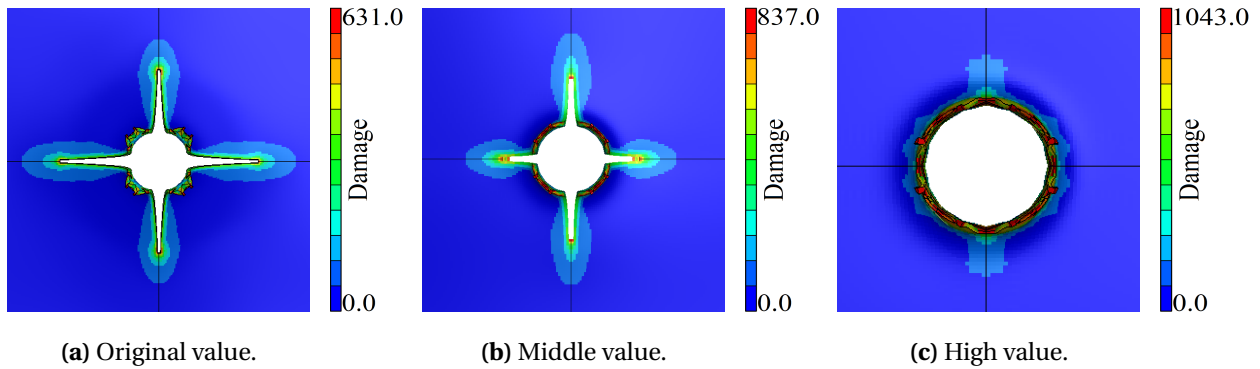
Figure 5.27: Contour plots of damage accumulation of D10_B1_25. The highest value of each colour bar is the same as the Cockcroft-Latham parameter for each simulation.

(a) Middle value. **(b)** High value.
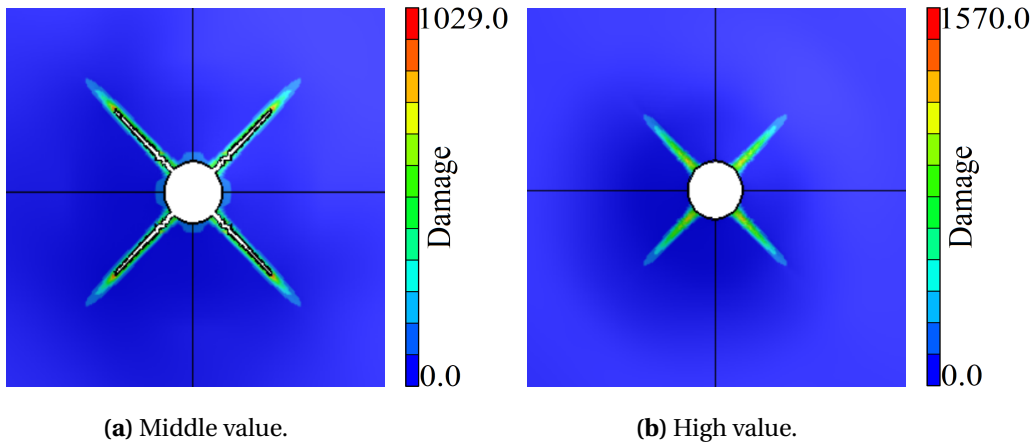
Figure 5.28: Damage accumulation D14_C1_25. The highest value of each colour bar is the same as the Cockcroft-Latham parameter for each simulation.

(a) Middle value.　　　　　　　　　　　　**(b)** High value.
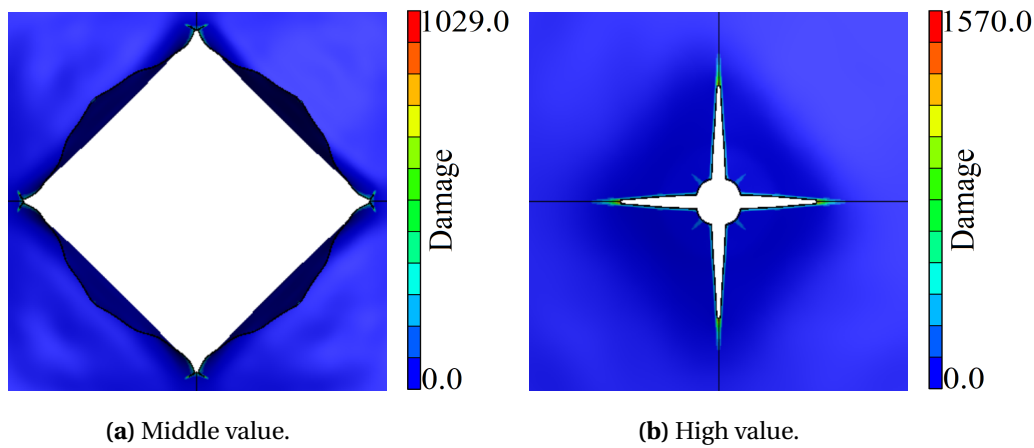
Figure 5.29: Damage accumulation D14_C1_35. The highest value of each colour bar is the same as the Cockcroft-Latham parameter for each simulation.

Table 5.6: Crack lengths of the three plates in the numerical study. C1 and C2 denotes the fractures of each plate.

Test	W_c	Mode	C1	C2
	[MPa]		[mm]	[mm]
D10_B1_25	837	Crack arrest	5.54	3.02
D10_B1_25	1043	Global deformation	-	-
D14_C1_25	1029	Crack arrest	13.85	-
D14_C1_25	1570	Global deformation	-	-
D14_C1_35	1029	Total failure	-	-
D14_C1_35	1570	Crack arrest	26.18	23.17

It is evident that increasing the fracture parameter yielded less crack propagation, which was an expected result. Figure 5.27 shows how the accumulated damage became more circular and the petals diminished as the fracture parameter increases. The cracking from the ballistic impact was significantly reduced. The highest W_c = 1043 MPa demonstrated no crack propagation at all, which proved that by increasing W_c enough cracking can be completely suppressed. The same is shown in Figure 5.28, where the plate transitions from an originally complete failure with W_c = 487 MPa to solely deformation with W_c = 1570 MPa. The damage accumulation is still clear along the diagonals of the hole.

The middle value of W_c = 1029 MPa was not enough to keep the D14_C1_25 plate from failing completely. Due to this complete failure, the last time frame of the simulation is not included in Figure 5.28a. The figure is of the entire plate, and is not a close-up. The failure mode was still the same as for W_c = 487 MPa. When W_c = 1570 MPa the cracks were arrested.

It has been shown that increasing the fracture parameter does not change the failure modes of the plates presented in this study. The only change is the crack lengths, which were reduced as the fracture parameter was increased. Some of the plates that experienced fracture in the original numerical model were even absent of cracking with the highest values of W_c.

5.6 Effect of Strain Rate Sensitivity Constant on Damage

It was discovered in the parameter study on the strain rate sensitivity constant c, in Section 5.4, that increasing the constant reduces the deformation in the simulations of blast loading of whole plates. Elveli and Iddberg[55] found that a decrease in c also yielded a larger extent of crack propagation on square perforated plates of Docol 600. The same trend was then expected for combined ballistic and blast loading, using a plate that would experience fracture. The test D10_B1_25 was simulated with an identical set-up in all ways except for the different strain rate sensitivity constant. It should be noted that the resulting damage from using values of 0.01 and 0.004 was compared to the damage using the value of 0.007 in the numerical computation in Section 5.2. The resulting damage can be seen in Figure 5.30, which contains close-ups of the fractures after blast loading.

(a) c=0.004　　　　　　**(b)** c=0.007　　　　　　**(c)** c=0.001
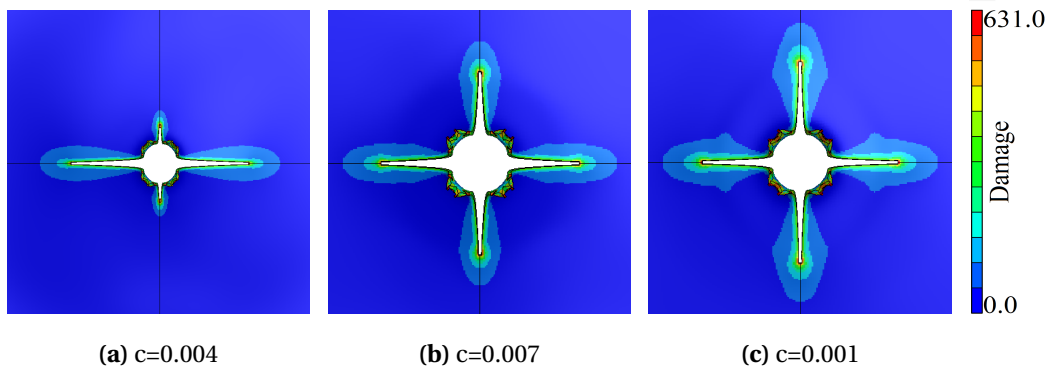
Figure 5.30: Close-up on area of fracture after blast loading of D10_B1_25 with different strain rate sensitivity constants.

The crack lengths have been measured to evaluate if there are any differences in the damage due to the strain rate sensitivity constant. Only their in-plane lengths were measured, so out-of-plane deformations were neglected. As it can be seen from the figures above, the three different constants yield different forms of deformations. Though all damage originated at the centre, with propagation occurring both vertically and horizontally, there was a difference between the lengths of the fractures and their symmetry. $c = 0.004$ yielded the longest and shortest crack, as seen in Table 5.7, whereas the other values of c gave a more symmetric result. The total crack length was the largest for $c = 0.004$, as seen in the fourth column. The highest strain rate sensitivity constant, $c = 0.01$, seemed to yield the lowest total crack length, although the differences are minor.

Table 5.7: Crack lengths of simulations with different strain rate sensitivity constants.

c	C1 [mm]	C2 [mm]	C1+C2 [mm]
0.004	4.94	20.29	25.23
0.007	11.05	12.60	23.65
0.01	11.52	11.45	22.97

5.7 Effect of Strain Rate and Principal Stress on Damage

It has been shown in the previous sections that there are several factors that can affect the damage and element erosion of the plate. From Equation (13), it can be observed that damage is dependent on the first principal stress and the plastic strain rate. These parameters are therefore inspected further, though the strain rate is used instead of the plastic strain rate, due to the availability in the numerical simulations. In Figure 5.31, the contour plots of the time frame immediately before fracture of the numerical simulation of D14_C1_25 is shown, which fractured along the diagonal. Figure 5.32 shows the same contour plots, solely for simulation D14_C1_35, which fractured in the vertical and horizontal directions. In both figures it is seen that the area that experienced the most damage, as presented in Figure (c), also had high values of strain rate compared to other areas of the plates. The same areas also had slightly higher values of maximum principal stress, though not as pronounced and localised.
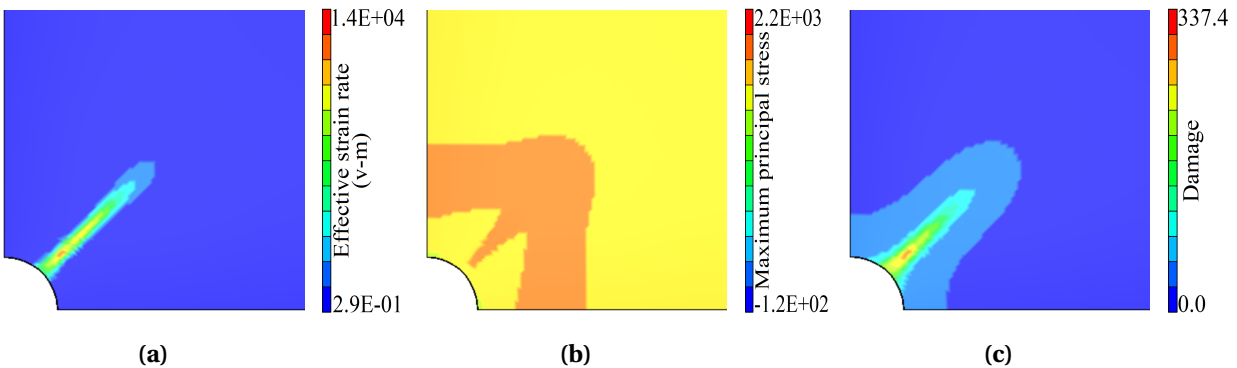
Figure 5.31: Contour plots of effective strain rate (v-m) in (a), maximum principal stress in (b) and damage in (c) for the D14_C1_25 test.
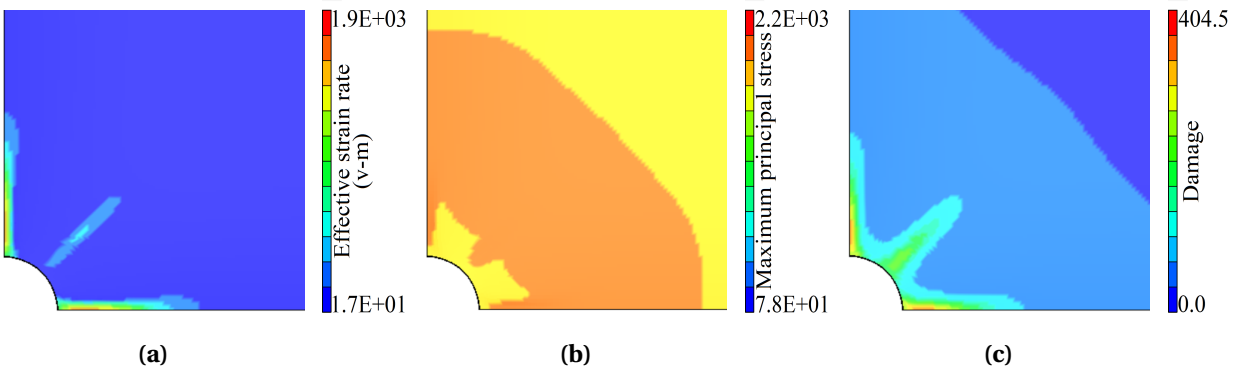
Figure 5.32: Contour plots of effective strain rate (v-m) in (a), maximum principal stress in (b) and damage in (c) for the D14_C1_35 test.

To further investigate the damage, strain rate and principal stress, an element was chosen for four different numerical simulations; D14_C1_25, D14_C1_35, D6_B1_25 and D14_B1_35. The element was chosen from the time frame just before erosion. The simulations were deemed

representative, as they all experienced fracture in the numerical calculations, with one of each configuration experiencing diagonal fracture and horizontal or vertical fracture. Figures 5.33a and 5.33b show the chosen elements for two tests. These underwent horizontal and diagonal fracture, respectively. The elements for the last tests were chosen in the same manner and time data was collected for all the four elements up until erosion. The resulting plots are shown in Figure 5.34. As the plastic strain rate, $\dot{p}$, was not available in the history output, the effective von Mises strain rate was chosen, $\dot{\varepsilon}$.

(a)   **(b)**
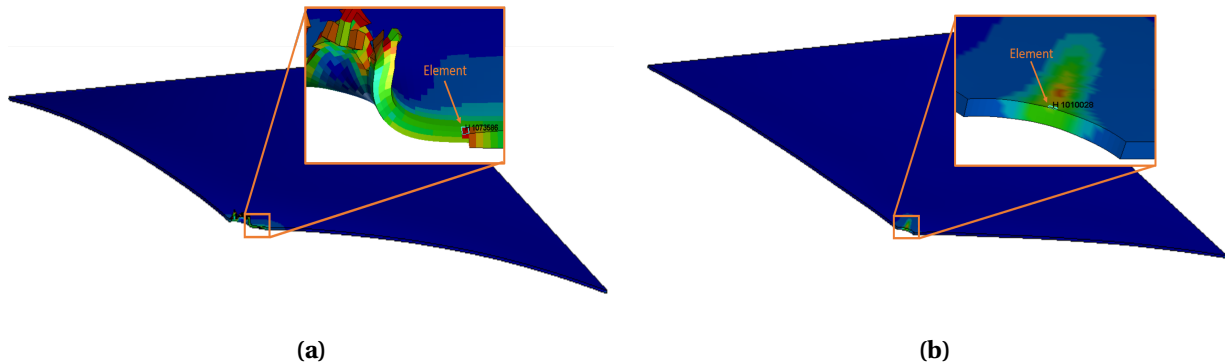
Figure 5.33: Two examples showing the elements for which the data are plotted. The elements are eroded in the next time frame.

It can be seen that the principal stresses build up gradually until fracture. For the C configurations the principal stress seems to flatten out and decrease just before fracture. The strain rate, however, has an abrupt increment just before fracture, when the damage parameter also experiences a sudden increment. The principal stress for the B configurations also experience a more sudden increase just before fracture, but not as prominent as the strain rate. It should be noted that the element in Figure 5.34c has an initial principal stress value. This is due to the cracking of this plate happening along the diagonal where the element chosen had remaining stress from the ballistic impact, though had not suffered significant damage. The element, for which data is plotted in Figure 5.34d, had experienced minor damage as it was chosen along the symmetry axes where crack initiation happened during ballistic impact.

(a) D14_C1_25

(b) D14_C1_35

(c) D14_B1_35

(d) D6_B1_25
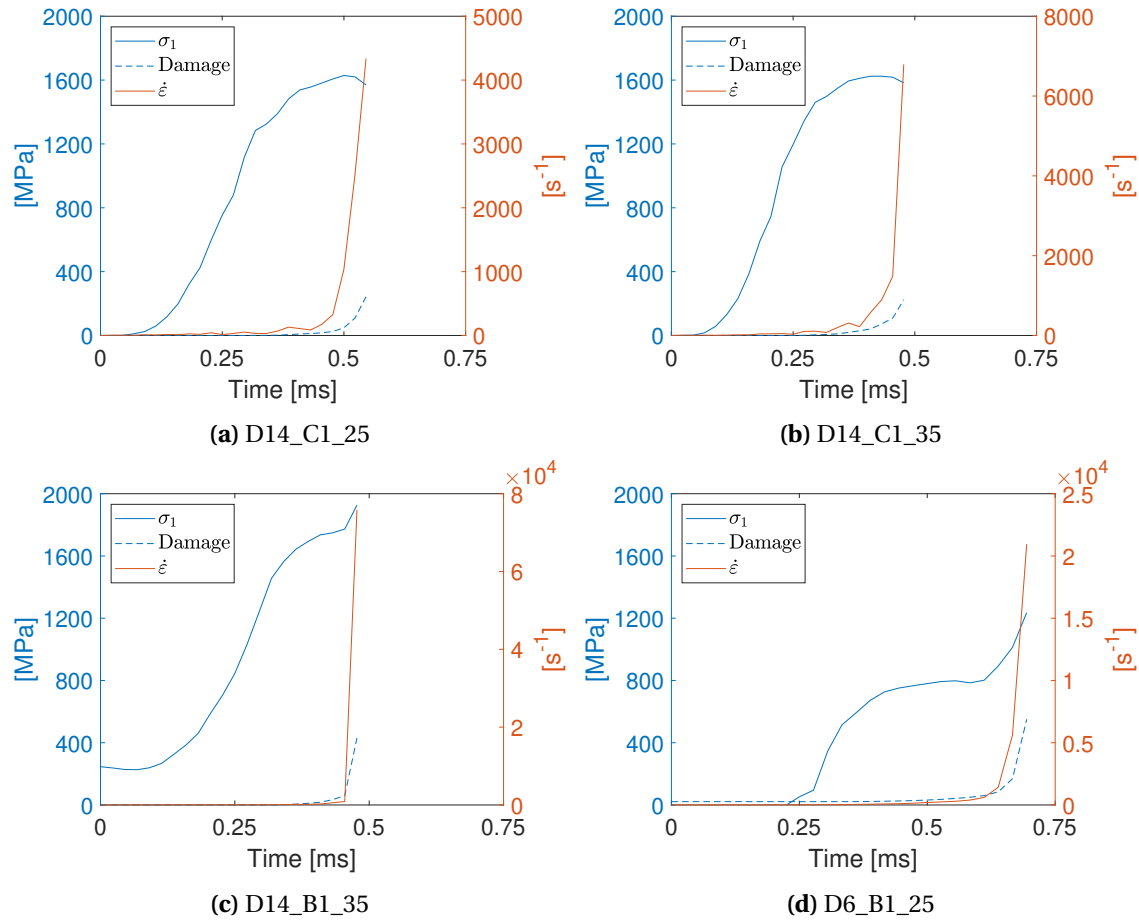
Figure 5.34: Plots for the elements seen in Figure 5.33 and from the two other test. They include maximum principal stress (solid blue line), damage (dashed blue line) and effective von Mises strain rate (orange line). Both maximum principal stress and damage are represented by the left y-axis as their dimensions are in MPa, whereas the strain rate is represented by the right y-axis and has the dimension of s^{-1}.

5.8   Concluding Remarks

The parametric study on boundary conditions showed that a model with a fully clamped assembly gives larger displacements than a simplified model that is fixed at the edges. This influence of the boundary conditions seems to increase with increasing material strength. As experiments were performed on whole plates of Docol 1000, these results were utilized to examine the performance of the simplified solid element model used to simulate the ballistic impact and blast loading of the plates. It was shown that the simplified model underestimated the displacements in the experiments.

The clamped model with shell elements seemed to predict results closer to the experiments. However, using shell elements for numerical simulations of ballistic impact is not recommended in order to describe fracture and crack propagation. On the other hand, using a fully clamped assembly with solid elements would be highly impractical for the purpose of this thesis given

the considerable computational time. This reflects one of the main challenges in the modelling of combined impact and blast loading. As a compromise, the simplified solid element model was deemed satisfying, with its limitations.

Agreement between the displacement histories of the numerical model and the blast loading experiments on perforated plates for Docol 600 was found to be good. For Docol 1000 and Docol 1400 the differences were more prominent in the general way that the numerically obtained deflections were lower than the experimental. This could be expected given the increasing effect of boundary conditions on the response of higher material strength, and the study conducted on whole plates of Docol 1000.

As observed in the experiments, Docol 1400 was most prone to fracture, followed by Docol 1000 and Docol 600. Failure in the simulations occurred at a somewhat lower global reference deflection than in the experiments for Docol 1000 and Docol 1400. This could be related to the numerical models predicting smaller deformations in the first place. The damage plots after ballistic impact showed that the area around the axes of symmetry had the highest level of damage at the base of the petals, with small crack initiation. Cracks also propagated from these areas in the subsequent simulations of the blast tests. As a results of the axes of symmetry, the models can only predict cracking symmetrical about these axes. The numerical model was able to replicate the different petal shapes for the various materials, as was obtained experimentally. Every simulation for the B configuration plates predicted crack propagation either horizontally or vertically and horizontally along the crack initiation from ballistic impact. The exception was the Docol 1400 plates, for which the cracking propagated diagonally until total failure. Plates of Docol 1400 with pre-formed holes experienced two different failure modes with respect to the direction of cracking.

In general, the crack propagation was exaggerated numerically compared to the fractures in the experiments. This was most evident for the Docol 1400 plates, which all experienced total failure in the simulations. A parametric study on the Cockcroft-Latham fracture criterion was therefore conducted for two larger values than the one calibrated for Docol 1000 and Docol 1400. As expected, the crack propagation was restricted by increasing W_c, indicating that the modelling of fracture should be investigated further in order to predict the experiments in an accurate manner.

The effect of changing the strain rate sensitivity constant was also examined in terms of global deformation as well as damage. Increasing the constant from $c = 0.004$ to $c = 0.01$, only slightly decreased the maximum deflection for the D1000 whole plate during blast loading. The total crack length was found to increase slightly with decreasing c, showing that the rate dependency is also a deciding factor when it comes to describing damage and fracture propagation. The importance of strain rate on the damage accumulation was confirmed by inspecting the contribution of maximal principal stress and strain rate to the damage evolution in the plates. It was found that damage evolution is highly related to the evolution of the strain rate.

It is important to emphasise that this thesis was limited to uncoupled simulations, and in cases of large deformations of the plates, the loading will be overly conservative as it is applied perpendicular to the plate throughout the entire simulation. Special focus was therefore placed on crack initiation and the first part of the crack propagation. It can be concluded that the level of crack initiation from ballistic impact was to some degree captured by the numerical models.

However, there seems to be a trend that these simulations are influenced by the symmetry conditions. Like in the experiments, the cracks mostly propagated from pre-existing cracks during blast loading. Reduced ductility was needed for cracks to propagate along the diagonals from the centre of the plate to its corner instead.

6 Discussion

The experimental results showed that work hardening and ductility were important for the blast-resistant capacity of the plates. The materials with higher strength and less ductility and hardening were outperformed by the low-strength materials with more ductility and hardening. These materials were able to spread out the deformation over a larger area, thereby reducing local straining, as seen in Section 4.4.4. For D600 hardly any plastic hinges are seen, and it seems dominated by membrane loading resulting in a deformation similar to of a global dome. On the other hand, D1400 has distinct local plastic hinges moving from the corners and towards the centre of the plates. When the hinges meet at the centre of the plate, the maximum deformation is reached, and some of the plates fracture under the high straining. As a result, D1400 has the lowest blast-resistant capacity, and D600 has the highest.

From both the experimental and numerical results, it was observed that the plates with pre-formed holes underwent less damage during the blast loading, than the plates subjected to ballistic impact. Thus, simplifying the experiment to not include fragmentation impact may lead to non-conservative results.

Due to the restricted time frame of this thesis, there were some limitations with respect to the material model, the physical experiments and the numerical simulations. The material model does not include anisotropy and, though previous studies on the steels under consideration in this thesis have concluded that they are isotropic, these have been performed on other batches of the same material, which may give a different result. The trend of more crack propagation in the rolling direction of the plate, could possibly indicate that there is some anisotropy in the material but this has not been included in the constitutive model, as most evidence points to isotropic behaviour. Isotropic material behaviour is also a necessary condition for the quarter model simulation of the plate in the numerical simulation, and significantly simplifies the problem at hand compared to an anisotropic material model.

Dynamic material tests have not been performed to identify dynamic material properties, such as the strain rate sensitivity constant, c, and the thermal softening constant, m. As a consequence, these have been taken from literature using other batches of material. As c proved difficult to find in any literature for D1000, this value was chosen based on the knowledge that the material properties of D1000 lie within the range of the properties of D600 and D1400. This may, however, be inaccurate and as discussed in Sections 5.3.2, 5.4 and 5.6, could influence the deformations and fractures in the numerical results. Furthermore, the strain rate sensitivity is set as constant throughout the thesis by using the MJC material model, even though Rakvåg et al.[6] found that it can vary with plastic strain.

The work during this thesis confirms the complexity involved in the assessment of combined ballistic impact and blast loading. As seen in Table 6.1, there are several differences between

blast and ballistic loading. Blast loading is more of a global problem with smaller strains and strain rates, compared to the ballistic impact which is a local problem. Although the deformation pattern of the blast loading is, as discussed in Section 4.4.4, influenced by the moving plastic hinge, which is a local effect. It should therefore be noted that the blast-resistance of the plates is to be considered as a global problem, at least until any localisation of damage occurs in the plates. So, the limitations of the material model may also have an effect here. Furthermore, as this is a combined problem, the discrepancies may influence the ballistic loading, which is a highly local problem. The errors from the ballistic loading will then be transferred to the blast loading for the B configuration plates.

Table 6.1: General differences between blast and ballistic loading. The table is taken from [56].

Blast load	Ballistic load
Global problem	Local problem
Structural problem	Material problem
Large deformations/stability	Local failure
Moderate strain and strain rates	Large strains and strain rates
Isothermal conditions	Adiabatic conditions
Complex, unknown loading	Simple, often well-identified, loading
Shell element formulation	2D-axisymmetric or 3D element formulation
Fluid-structure interaction (FSI)	No fluid-structure interaction (FSI)
Coupled Eulerian - Lagrangian FEA	Lagrangian FEA
Complex tests	Simple test
Fluid mechanics	Solid mechanics

In reality, when a plate undergoes blast loading from an explosion, fragments may only impact the target if the stand-off distance is short enough and the wave travels slower than the primary fragments. This is thus an underlying assumption of this thesis. In this particular scenario, it is possible that the plate under investigation may vibrate from the impact of the fragments when the blast loading occurs. This is not investigated here, since test facilities that can perform a ballistic and blast test within milliseconds was not available for the work in this thesis.

Due to limited time and resources, a simplified model has been used in the numerical simulations. From Table 6.1, it is evident that blast loading and ballistic loading are vastly different problems that usually are simplified in different ways to allow for reduced computational time. However, with the combined loading case, the same model had to be used for both cases. Due to the short duration of ballistic loading compared to the blast loading time, in addition to the ballistic problem being a local problem, the mesh is usually of solid or 2D-axisymmetric elements, and very dense. The blast mesh is usually of shell elements and less dense to allow for a longer time step and faster calculations, as the calculation time is dependent on both the number of elements and its size, as seen in Section 5.2.3. A compromise between capturing both global and local effects had to be made, which lead to a solid mesh of three elements over the thickness, and simplifications wherever possible. The nature of the thin plate, would suggest that the plate will mostly experience membrane forces, rather than bending forces. When membrane forces need to be captured, shell elements would often be preferred. Moreover, the uncoupled model used

in this thesis is expected to overestimate the deformations since it neglects FSI effects. In summary, there are several simplifications that may either increase or decrease the deformations. As a result, if exact replication of the experimental results was achieved from the computational results, it could possibly have been due to two conflicting simplifications working against each other. Neglecting FSI effects could, for instance, increase the deformations, whilst the simplifications of the boundary conditions will decrease the deformations.

7 Conclusions

In this thesis, material tests were firstly performed on D600, D1000 and D1400 to characterise the materials. The data was then then fitted to the MJC material model and the Cockcroft-Latham failure criterion calibrated. Then, both ballistic and blast load experiments were carried out on thin steel plates of the aforementioned materials. Finally, numerical simulations of the component tests were performed to see whether the numerical model was able to replicate the results of the experiments. Consequently, several findings have been observed, with the most important observations presented in the following list.

- In the material tests, the trend from the manufacturer's data sheet was confirmed; D600 is more ductile and work hardens more than the other two materials, with D1400 being the least ductile. Furthermore, D1400 has the highest yield strength and D600 has the lowest.

- As expected, larger blast intensities lead to a larger deformation in the plates for all materials considered in this thesis.

- Each different material responds differently in the experimental tests. Concerning permanent deformations, D600, which is the most ductile, had the largest global deformations. D600 also experienced the largest maximum deflection. D1400 had the least permanent global deformations, but was more prone to pronounced travelling plastic hinges. In contrast, the D600 deformation shape was like that of a global dome. It was also found that D1400 was considerably more susceptible to fracture than D600. The D1000 material was found to be in-between D600 and D1000 with respect to deformation and fracture.

- Whole plates, of D configuration, had no fracture during blast loading. The plates with pre-formed holes, C configuration, had some fracture but considerably less than the ballistic plates of B configuration. The B configurations had the most fracture, with the cracks that initiated during ballistic impact seeming to propagate when blast loaded.

- The numerical simulations are, to some extent, able to replicate the behaviour from the physical tests, although simplifications were made, reducing the accuracy. The simplifications were necessary with the limited time at hand. The leading obstacle for the numerical work is to combine the assumptions for both loading cases so as to predict satisfactory results without increasing the complexity to a highly impractical level.

- Boundary conditions have an effect on the deformations of the plate in the numerical simulations, and a simulation containing the fully clamped assembly results in a higher global

deformation in the simulations compared to the boundary conditions that are fixed in all translational and rotational directions. The assembly with clamped boundary conditions resulted in a deformation that is closer to that of the experiments, but is too computationally expensive.

- The model's ability to predict crack initiation from ballistic impact is essential to describe the correct failure modes and crack propagation as, at least for the lower strength materials, cracking continued from these areas of eroded elements. The fracture predicted by the computational model are too large compared to the experiments. As expected, the fracture was dependent on the Cockcroft-Latham failure parameter W_c, but susceptible to the viscoplasticity through the strain rate sensitivity constant c. Hence, MJC may not be sufficient to capture the possibly varying strain rate sensitivity of the materials.

8 Further Work

This thesis was limited to three different steel materials, as well as plates of thickness $0.8\,\text{mm}$ with one hole in the centre. To investigate the field of combined ballistic impact and blast loading, there are several topics that could be looked into in future work for greater insight into this topic. For instance, the number of holes and their spatial distribution could affect the results. Furthermore, by increasing the thickness of the plate, bending deformation may dominate, membrane deformation may be diminished and other failure modes than petalling may occur instead. Moreover, the blast problem could change from a global to a more local problem, by using explosive detonations close to the plates to generate the blast loading. A change in the size of the holes, both the pre-formed hole and the ballistic hole with pre-existing damage can also be investigated, in an effort to see whether this affects the mode of failure or if plates with ballistic holes would still be more prone to fracture.

The material parameters have been obtained by manual calibration, while there exist programs, such as LS-OPT, which aid the calibration of an accurate fit to the experimental data. As simplifications have been made in the identification of the material parameters, dynamic tests, such as the Split-Hopkinson Tensile Bar (SHTB) test, should be conducted for D1000 as well. Since this work indicates that the material behaviour is not accurately reproduced using a strain rate sensitivity constant, a material model that allows for a variable strain rate sensitivity should be investigated. Variability in the strain rate sensitivity should also be included in the failure criterion.

Extensive failure of the plate was not simulated accurately, hence a suggestion for further work is to look into the failure criterion and the identification of the W_c parameter. To accurately emulate the unsymmetrical failure of the experiment is impossible with the quarter model. Due to this, an alternative suggestion would be to simulate using a whole model instead of a quarter model. Investigating the FSI effects on crack propagation and deformation using a coupled approach in either LS-DYNA or another FEA program could also be beneficial.

It was shown in this thesis that the boundary conditions affected the results severely and that the simplification of fixed boundary conditions was inaccurate. A full-scale simulation of the clamping of the plate with the solid elements could ultimately be conducted.

Due to time restrictions, the simulation time was limited. If possible, it would therefore be interesting to increase the simulation time so the complete response of the plates could be captured and compared to experimental results from DIC and point clouds. Calibration of the constitutive model and failure criteria for different material tests lying within a range of strain at fracture could also be completed, with the potential variation in structural response examined.

Lastly, a parametric study on mesh refinement should be conducted to investigate the effect of only three elements over the thickness of the plate and whether the global response and damage are affected by changing the mesh.

Bibliography

[1] "National consortium for the study of terrorism and responses to terrorism," Global terrorism database (GTD), (accessed: 26.05.20). [Online]. Available: https://www.start. umd.edu/gtd/

[2] H. Y. Grisaro and A. N. Dancygier, "Characteristics of combined blast and fragments loading," *International Journal of Impact Engineering*, vol. 16, pp. 51–64, 2018.

[3] U. Nystrom and K. Gylltoft, "Numerical studies of the combined effects of blast and fragment loading," *International Journal of Impact Engineering*, vol. 36, no. 8, pp. 995–1005, 2009.

[4] H. Hao. International journal of protective structures. SAGE Publishing. (accessed: 27.05.2020). [Online]. Available: http://www.multi-science.co.uk/ijps.htm

[5] A. Hald, "Dynamic Response of Steel Plates Subjected to Combined Impact and Blast Loading, An Experimental and Numerical Study," 2019, M.S. thesis, Norwegian University of Science and Technology (NTNU).

[6] K. G. Rakvåg, N. J. Underwood, G. K. Schleyer, T. Børvik, and O. S. Hopperstad, "Transient pressure loading of clamped metallic plates with pre-formed holes," *International Journal of Impact Engineering*, vol. 53, pp. 44–55, 2013.

[7] H. Granum, V. Aune, T. Børvik, , and O. S. Hopperstad, "Aluminium plates with pre-formed slits subjected to blast loading," *EPJ Web of Conferences*, vol. 183, 2018.

[8] H. Granum, V. Aune, T. Børvik, and O. S. Hopperstad, "Effect of heat-treatment on the structural response of blast-loaded aluminium plates with pre-cut slits," *International Journal of Impact Engineering*, vol. 132, pp. 103–306, 2019.

[9] V. Aune, G. Valsamos, F. Casadei, M. Langseth, and T. Børvik, "On the dynamic response of blast-loaded steel plates with and without pre-formed holes," *International Journal of Impact Engineering*, vol. 108, pp. 27–46, 2017.

[10] H. H. Kristiansen and G. Sigstad, "Dynamic response of blast-loaded steel plates with and without preformed holes," 2019, M.S. thesis, Norwegian University of Science and Technology (NTNU).

[11] B. S. Elveli, T. Børvik, , and V. Aune, "Blast-load response of thin steel plates after balllistic impact from small-arms projectiles," *LWAG*, 2019.

[12] K. Osnes, S. Dey, O. S. Hopperstad, and T. Børvik, "On the dynamic response of laminated glass exposed to impact before blast loading," *Experimental Mechanics*, pp. 1–14, 2019.

[13] X. Kong, W. Wu, J. Li, P. Chen, and F. Liu, "Experimental and numerical investigation on a multi-layer protective structure under the synergistic effect of blast and fragment loadings," *International Journal of Impact Engineering*, vol. 65, pp. 146–162, 2014.

[14] P. Del Linz, S. Fan, and C. Lee, "Modeling of combined impact and blast loading on reinforced concrete slabs," *Latin American Journal of Solids and Structures*, vol. 13, no. 12, pp. 2266–2282, 2016.

[15] T. Iuchi, Y. Yamada, M. Sugira, and A. Torao, in *Experimental Methods in the Physical Sciences*. Elsevier, 2010, ch. 4 - Thermometry in Steel Production.

[16] J. Hollandt, J. Hartmann, O. Struß, and R. Gärtner, in *Experimental Methods in the Physical Sciences*. Elsevier, 2010, ch. 1 - Industrial Applications of Radiation Thermometry.

[17] Docol DP/DL Cold reduced dual phase steels. SSAB. (accessed: 24.03.2020). [Online]. Available: http://www.meracing.com/high-strength-steel/docol__1293

[18] Docol M Cold reduced martensitic steels. SSAB. (accessed: 24.03.2020). [Online]. Available: https://www.yumpu.com/en/document/read/11500088/docol-m-ssab

[19] Mahr Digital Micrometer 40 EW / 40 EXL. Mahr. (accessed: 24.03.2020). [Online]. Available: http://www.industributiken.se/english/measuring-tools/micrometers/mahr-digital-micrometer-40-ew-40-exl.html

[20] T. Børvik, "Impact mechanics: An introduction to blast loading," lecture Notes in TKT4128, (accessed: 14.04.2020). [Online]. Available: https://ntnu.blackboard.com/webapps/blackboard/content/listContent.jsp?course_id=_14952_1&content_id=_819077_1

[21] N. McCormick and J. Lord, "Digital Image Correlation," *Materials Today*, vol. 13, no. 12, pp. 52–54, 2010.

[22] E. Fagreholt. eCorr v4.0 Documentation. (accessed: 10.04.2020). [Online]. Available: http://folk.ntnu.no/egilf/ecorr/doc/index.html#

[23] G. Gruben, M. Langseth, E. Fagerholt, and O. S. Hopperstad, "Low-velocity impact on high-strength steel sheets: An experimental and numerical study," *International Journal of Impact Engineering*, vol. 88, pp. 153–171, 2016.

[24] J. K. Holmen, O. S. Hopperstad, and T. Børvik, "Low-velocity impact on multi-layered dual-phase steel plates," *International Journal of Impact Engineering*, vol. 78, pp. 161–177, 2014.

[25] O. S. Hopperstad and T. Børvik, "Impact mechanics – part 1: Modelling of plasticity and failure with explicit finite element methods," lecture note in the NTNU course TKT4128,(accessed: 28.04.2020). [Online]. Available: https://ntnu.blackboard.com/webapps/blackboard/content/listContent.jsp?course_id=_15320_1&content_id=_750483_1

[26] A. V. Hershey, "The plasticity of an isotropic aggregate of anisotropic face-centered cubic crystals," *Journal of Applied Mechanics*, vol. 76, pp. 241–249, 1954.

[27] R. Logan and W. F. Hosford, "Upper-bound anisotropic yield locus calculations assuming-pencil glide," *International Journal of Mechanical Sciences*, vol. 22(7), pp. 419–430, 1980.

[28] V. Aune, "Behaviour and modelling of flexible structures subjected to blast loading," Ph.D. dissertation, Norwegian University of Science and Technology (NTNU), 2017. [Online]. Available: https://ntnuopen.ntnu.no/ntnu-xmlui/bitstream/handle/11250/2441684/Vegard%20Aune_PhD.pdf?sequence=1&isAllowed=y

[29] M. G. Cockcroft and D. J. Latham, "Ductility and the workability of metals," *Journal of the Institute of Metals*, vol. 96, pp. 33–39, 1968.

[30] S. Dey, T. Børvik, O. S. Hopperstad, and M. Langseth, "On the influence of fracture criterion in projectile impact of steel plates," *Computational Materials Science*, vol. 38, pp. 175–191, 2006.

[31] H. Wadleya, T. Børvik, L. Olovsson, J. Wetzel, K. Dharmasena, O. Hopperstad, V. Deshpande, and J. Hutchinson, "Deformation and Fracture of Impulsively Loaded Sandwich Panels," *Journal of the Mechanics and Physics of Solids*, vol. 62, no. 1, pp. 674–699, 2013.

[32] T. Børvik, S. Dey, and A. H. Clausen, "Perforation resistance of five different high-strength steel plates subjected to small-arms projectiles," *International Journal of Impact Engineering*, vol. 36, no. 7, pp. 948–964, 2009.

[33] A. Kane, T. Børvik, and A. H. Clausen, "Failure criteria with unilateral conditions for simulation of plate perforation," *European Journal of Mechanics - A/Solids*, vol. 30, no. 4, pp. 468–476, 2011.

[34] T. Børvik, O. S. Hopperstad, and M. Langseth, "Impact mechanics: An introduction to penetration and perforation mechanics," lecture Notes in TKT4128. [Online]. Available: https://ntnu.blackboard.com/bbcswebdav/pid-732426-dt-content-rid-21815438_1/xid-21815438_1

[35] V. Aune, E. Fagerholt, M. Langseth, and T. Børvik, "A shock tube facility to generate blast loading on structures," *International Journal of Protective Structures*, vol. 7, no. 3, pp. 340–366, 2016.

[36] "Romer absolute arm," Hexagon Metrology, (accessed: 28.04.2020). [Online]. Available: https://www.hexagonmi.com/?utm_source=DomainRedirect&utm_medium=hexagonmetrology_com

[37] "movmean," MathWorks. [Online]. Available: https://se.mathworks.com/help/matlab/ref/movmean.html

[38] V. Aune, G. Valsamos, F. Casadei, M. Langseth, and T. Børvik, "Fluid-structure interaction effects during the dynamic response of clamped thin steel plates exposed to blast loading," *Preprint submitted to International Journal of Mechanical Sciences*, 2020.

[39] Fluid-structure interaction. (accessed: 14.04.2020). [Online]. Available: https://www.comsol.com/multiphysics/fluid-structure-interaction

[40] O. Zienkiewicz, R. Taylor, and P. Nithiarasu, in *The Finite Element Method for Fluid Dynamics (Seventh Edition)*. Elsevier, 2014, ch. 13 - Fluid–Structure Interaction.

[41] R. D. Blevins, *Formulas for natural frequency and mode shape.* Van Nostrand Reinhold Company, 1979.

[42] X. Bai, L. Zhu, and T. Yu, "Saturated impulse for fully clamped square plates under blast loading," *International Journal of Mechanical Sciences*, vol. 146–147, pp. 417–431, 2018.

[43] M. Escudier and T. Atkins, *A Dictionary of Mechanical Engineering, 2 ed.* Oxford University Press, 2019.

[44] N. Jones, *STRUCTURAL IMPACT, second edition.* Cambridge University Press, 2012.

[45] "RS PRO 150mm Digital Caliper 0.0005 in 0.01 mm Metric & Imperial," RS Components, (accessed: 07.04.2020). [Online]. Available: https://no.rs-online.com/web/p/calipers/8412518?cm_mmc=NO-PLA-DS3A-_-google-_-CSS_NO_NO_Test_And_Measurement-_-Linear_Measurement%7CCalipers-_-PRODUCT_GROUP&matchtype=&pla-397138506212&gclid=Cj0KCQjwybD0BRDyARIsACyS8mvXC31S87dCOxCPZD3Uh5bhWW8ZqGOgxjopcEABYZrV.soL0UnmrauQaAuztEALw_wcB&gclsrc=aw.ds

[46] P. Ghosh and R. Ray, in *Automotive Steels.* Elsevier, 2016, ch. 5 - Deep drawable steels.

[47] T. Børvik, M. J. Forrestal, O. S. Hopperstad, T. I. Warren, and M. Langseth, "Perforation of AA5083-H116 aluminium plateswith conical-nose steel projectiles – Calculations," *International Journal of Impact Engineering*, vol. 36, no. 3, pp. 426–437, 2009.

[48] J. Tu, G. Yeoh, and C. Liu, in *Computational Fluid Dynamics: A Practical Approach.* Elsevier, 2019, ch. 4 - CFD Mesh Generation: A Practical Guideline.

[49] R. D. Cook, D. S. Malkus, M. E. Plesha, and R. J. Witt, *Concepts and Applications of Finite Element Analysis, fourth edition.* John Wiley & Sons. Inc., 2002.

[50] "Ls-dyna theory manual," Livermore Software Technology Corporation (LSTC), 2016, compiled by John O. Hallquist.

[51] "Ls-dyna keyword user's manual volume 1 r11," Livermore Software Technology Corporation (LSTC), 2018, documentation found from LS-Run 1.0.

[52] J. K. Holmen, J. Johnsen, S. Jupp, O. S. Hopperstad, and T. Børvik, "Effects of heat treatment on the ballistic porperties of AA6070 aluminium alloy," *International Journal of Impact Engineering*, vol. 57, pp. 119–133, 2013.

[53] M. Ravid and R. Bodner, "Dynamic perforation on viscoplastic plates by rigid projectiles," *International Journal of Engineering Science*, vol. 21, no. 6, pp. 577–591, 1983.

[54] K. Bell, *Engineering Approach to Finite Element Analysis of Linear Structural Mechanics Problems.* Akademika, 2015.

[55] B. S. Elveli and M. B. Iddberg, "Experimental and numerical study on perforated plates subjected to blast loading," 2018, M.S. thesis, Norwegian University of Science and Technology (NTNU).

[56] T. Børvik, "Impact mechanics: An introduction to blast loading," handout in TKT4128, (accessed: 13.04.2020). [Online]. Available: https://ntnu.blackboard.com/webapps/blackboard/content/listContent.jsp?course_id=_14952_1&content_id=_819077_1&mode=reset

[57] S. Henin, "popout," mATLAB Central File Exchange. [Online]. Available: https://www.mathworks.com/matlabcentral/fileexchange/30556-popout)

Appendix

A   Component Measurements

Table .1: Test matrix of material tests with specimen measurements and comments from testing. t_{nr} and w_{nr} are the measurements of the width and thickness of the dog-bone tests. The specimen names give the material, the orientation and the test number. D600-0-1 is for instance the first specimen of Docol 600 DL orientated at 0° compared to the rolling direction.

Specimen	t_1 [mm]	t_2 [mm]	t_3 [mm]	w_1 [mm]	w_2 [mm]	w_3 [mm]	Comment
D600-0-1	0.817	0.817	0.815	12.532	12.535	12.531	
D600-0-2	0.821	0.821	0.817	12.539	12.538	12.531	
D600-0-3	0.820	0.817	0.815	12.526	12.528	12.530	Tested without shims
D600-45-1	0.817	0.814	0.815	12.528	12.525	12.523	
D600-45-2	0.816	0.817	0.814	12.555	12.548	12.535	
D600-45-3	0.815	0.816	0.814	12.522	12.527	12.526	
D600-90-1	0.816	0.816	0.813	12.535	12.543	12.538	
D600-90-2	0.822	0.820	0.814	12.544	12.534	12.529	
D600-90-3	0.816	0.819	0.815	12.531	12.535	12.557	
D1000-0-1	0.789	0.791	0.788	12.523	12.520	12.509	
D1000-0-2	0.799	0.802	0.799	12.526	12.525	12.513	
D1000-0-3	0.805	0.804	0.802	12.534	12.531	12.526	
D1000-45-1	0.813	0.813	0.816	12.525	12.526	12.529	
D1000-45-2	0.812	0.811	0.808	12.522	12.522	12.526	
D1000-45-3	0.808	0.810	0.811	12.555	12.546	12.541	
D1000-90-1	0.799	0.802	0.803	12.523	12.526	12.529	
D1000-90-2	0.794	0.818	0.802	12.528	12.525	12.523	
D1000-90-3	0.795	0.803	0.804	12.527	12.526	12.526	
D1400-0-1	0.817	0.815	0.813	12.523	12.518	12.523	
D1400-0-2	0.814	0.815	0.815	12.555	12.580	12.575	
D1400-0-3	0.807	0.804	0.802	12.507	12.508	12.517	
D1400-45-1	0.819	0.813	0.816	12.521	12.528	12.527	
D1400-45-2	0.816	0.811	0.819	12.534	12.533	12.574	Hard to measure, warped specimen
D1400-45-3	0.817	0.814	0.816	12.531	12.524	12.520	
D1400-90-1	0.812	0.813	0.820	12.525	12.531	12.531	
D1400-90-2	0.818	0.817	0.818	12.525	12.532	12.539	
D1400-90-3	0.822	0.820	0.818	12.527	12.528	12.535	

B   Matlab Scripts

Deformation profiles from DIC:

```matlab
%Plot displacements, midpoint and deformation fields:
clear all;close all;clc;

t0=50; %time when pressure wave hits sensor 1qstat
rig=[95        92        89        87        83]; %frames when deformation
%profiles are collected
tp=(rig-t0)./37;%time, 37 kHz is sampling frequency

%import midpoint displacement:
data=readtable('midP.txt', 'ReadVariableNames',false);
Dmid=table2array(data(t0:end,2));
clear data

%import rig movement:
data=readtable('subset.txt', 'ReadVariableNames',false);
Drig=table2array(data(t0:end,2));
clear data

%rig displacement at different profiles:
a100=Drig(rig(1));
a90=Drig(rig(2));
a75=Drig(rig(3));
a60=Drig(rig(4));
a40=Drig(rig(5));

Dmid=-Dmid; %positive axis
Dmid_new=(Dmid+Drig); %corrected for rig movement
f=1/37; %frquency
t=[0:f:f*(length(Dmid_new)-1)]; %time vector

%Plot reference point deformation:
f=figure;
plot(t,Dmid_new); hold on;
xlabel('Time [ms]')
ylabel('Midpoint \Delta Z [mm]')
supersizeme(f,2.5)

%import deformation profiles:
startRow = 4;
formatSpec = '%17s%26s%26s%26s%26s%26s%26s%26s%26s%26s%s%[^\n\r]';
fileID = fopen('profile.txt','r');
```

```matlab
dataArray = textscan(fileID, formatSpec, 'Delimiter', '', 'WhiteSpace',
'', 'TextType', 'string', 'HeaderLines' ,startRow-1, 'ReturnOnError',
false, 'EndOfLine', '\r\n');
fclose(fileID);

%convert from table to plottable arrays:
profile = table;
x100 = str2double(dataArray{1,1});
z100 = -str2double(dataArray{1,2})-a100;
x90 = str2double(dataArray{1,3});
z90 = -str2double(dataArray{1,4})-a90;
x75 = str2double(dataArray{1,5});
z75 = -str2double(dataArray{1,6})-a75;
x60 = str2double(dataArray{1,7});
z60 = -str2double(dataArray{1,8})-a60;
x40 = str2double(dataArray{1,9});
z40 = -str2double(dataArray{1,10})-a40;

%shift profiles to begin at same position as LS Dyna results:
x100=x100-x100(1)+18.1;
x90=x90-x90(1)+18.1;
x75=x75-x75(1)+18.1;
x60=x60-x60(1)+18.1;
x40=x40-x40(1)+18.1;

%Plot profiles:
f=figure;
plot(x100,z100); hold on;
plot(x90,z90)
plot(x75,z75)
plot(x60,z60)
plot(x40,z40)
xlabel('Plate Position [mm]')
ylabel('\Delta z [mm]')
legendCell = cellstr(num2str(tp', 't=%.2f')); %time legends from string
legend(legendCell)
supersizeme(f,1.7) %function for generating correct font size

%clear all variables:
clearvars filename startRow formatSpec fileID dataArray ans raw col numericData
rawData row regexstr result numbers invalidThousandsSeparator thousandsRegExp
rawNumericColumns rawStringColumns R idx;
```

Listing 1: Matlab code to plot deformation profiles from 3D DIC.

Import points for point cloud:

```matlab
function [PC, x, y, z] = ImportPoints(file) %function name

fid = fopen(file); %open file
idx = 1; % while loop counter
%create empty strings:
x=[];
y=[];
y=[];

i=1; %if loop counter
while ~feof(fid) %Check every line in the file
    templine = fgetl(fid); %Read line
    if ~strcmp(templine(1),'L') %If it does not begin with L...
        Clean_Data{idx,1} = templine; %Record line
        data{idx,1} = strsplit(templine); %split string
        if length(data{idx})==3 %split into 3 vectors; x, y, z
            x(i)=str2double(data{idx}{1});
            y(i)=str2double(data{idx}{2});
            z(i)=str2double(data{idx}{3});
            i=i+1; %increase counter by 1
        else
            %Do nothing
        end
        idx = idx+1; %increase counter by 1
    else %If it begins with L...
        % Do nothing
    end
end
PC=[transpose(x),transpose(y),transpose(z)];%output
end
```

Listing 2: Matlab code to import points from laser scanner's .xyz file.

Point cloud:

```matlab
clear all;
clc;
close all;

%Import points:
[PC, x, y, z] = ImportPoints('D10_C1_25_Pre.xyz'); %Call import function
x=transpose(x);
y=transpose(y);
z=transpose(z);

%Point cloud before filtering
ptCloud1 = pointCloud([x,y,z]);
f=figure;
pcshow(ptCloud1); hold on;
view([45 45])
colorbar('eastoutside')
grid off
supersizeme(f,1.7)

% Manual filtering in X:
xmin=x<15;
x(xmin) = [];
y(xmin) = [];
z(xmin) = [];

xmax=x>285;
x(xmax) = [];
y(xmax) = [];
z(xmax) = [];

% Manual filtering in Y:
ymin=y<15;
x(ymin) = [];
y(ymin) = [];
z(ymin) = [];

ymax=y>285;
x(ymax)=[];
y(ymax)=[];
z(ymax)=[];
```

```matlab
% Manual filtering in Z:
zmax=z>35;
x(zmax)=[];
y(zmax)=[];
z(zmax)=[];

zmin=z<-3;
x(zmin)=[];
y(zmin)=[];
z(zmin)=[];

%Point cloud after filtering
ptCloud2 = pointCloud([x,y,z]);
f=figure;
pcshow(ptCloud2); hold on;
colorbar('eastoutside')
view([45 45])
grid off
supersizeme(f,1.7)
```

Listing 3: Matlab code to plot point clouds and remove unnecessary points.

Post processing material tests:

```matlab
clear all; close all; clc;

%Import all data from DIC:
if exist('data_full.txt','file')
    fid1 = fopen('data_full.txt','r');
    data=readtable('data_full.txt', 'ReadVariableNames',false);
    fclose(fid1);
end
m=table2array(data);
clear data

%Create load and length matrices:
for i = 1:27
    n=2*i;
    L(:,i)=m(:,n-1);
    f(:,i)=m(:,n);
end

%Import tensile results from LS Dyna:
if exist('D600_A.txt','file')
    fid1 = fopen('D600_A.txt','r');
    data=fscanf(fid1,'%f ',[2 inf]);
    fclose(fid1);
end
xLSA=(30-data(1,:)).*2; %length
fLSA=4*data(2,:) ;%load
clear data
eLSA=(xLSA-xLSA(1))/xLSA(1); %eng strain
ALS=12.5*0.4*2; %cross sectional area
sLSA=fLSA./ALS; %eng stress

if exist('D600_I.txt','file')
    fid1 = fopen('D600_I.txt','r');
    data=fscanf(fid1,'%f ',[2 inf]);
    fclose(fid1);
end
xLSI=(30-data(1,:)).*2; %length
fLSI=4*data(2,:); %load
clear data
eLSI=(xLSI-xLSI(1))/xLSI(1);%eng strain
ALS=12.5*0.4*2; %cross sectional area
sLSI=fLSI./ALS;%eng stress
```

```matlab
%Import thickness and width measurements from experiment:
if exist('Materialtester.txt','file')
    fid1 = fopen('Materialtester.txt','r');
    data=fscanf(fid1,'%f ',[8 inf]);
    fclose(fid1);
end

for i=1:27
t(i)=sum(data(3:5,i))/3; %avg thickness before test
w2(i)=sum(data(6:8,i))/3; %avg width before test
A(i)=t(i)*w2(i); %resulting area
end
clear data
for i=1:27 %Engineering strain and stress:
    e(:,i)=(L(:,i)-L(1,i))/L(1,i);
    s(:,i)=1000*f(:,i)/(A(i));
end

%Plot eng. stress and strain for D600:
f=figure;
for i=1:3
    plot(e(:,i),s(:,i), 'r'); hold on;
end
for i=4:6
    plot(e(:,i),s(:,i), 'k'); hold on;
end
for i=7:9
    plot(e(:,i),s(:,i), 'b'); hold on;
end
xlabel('Engineering strain [-]')
ylabel('Stress [MPa]')
legend('0{\circ} 1', '0{\circ} 2', '0{\circ} 3', '45{\circ} 1', '45{\circ} 2',
'45{\circ} 3', '90{\circ} 1', '90{\circ} 2', '90{\circ} 3')
title('Docol 600')
xlim([0,0.35])
ylim([1,700])
supersizeme(f,1.5)

%Plot eng. stress and strain for D1000:
f=figure;
for i=10:12
    plot(e(:,i),s(:,i), 'r'); hold on;
end
```

```matlab
for i=13:15
    plot(e(:,i),s(:,i), 'k'); hold on;
end
for i=16:18
    plot(e(:,i),s(:,i), 'b'); hold on;
end
xlabel('Engineering strain [-]')
ylabel('Stress [MPa]')
legend('0{\circ} 1', '0{\circ} 2', '0{\circ} 3', '45{\circ} 1', '45{\circ} 2',
'45{\circ} 3', '90{\circ} 1', '90{\circ} 2', '90{\circ} 3')
title('Docol 1000')
xlim([0,0.15])
ylim([0,1200])
supersizeme(f,1.5)

%Plot eng. stress and strain for D1400:
f=figure;
for i=19:21
    plot(e(:,i),s(:,i), 'r'); hold on;
end
for i=22:24
    plot(e(:,i),s(:,i), 'k'); hold on;
end
for i=25:27
    plot(e(:,i),s(:,i), 'b'); hold on;
end
xlabel('Engineering strain [-]')
ylabel('Stress [MPa]')
legend('0{\circ} 1', '0{\circ} 2', '0{\circ} 3', '45{\circ} 1', '45{\circ} 2',
'45{\circ} 3', '90{\circ} 1', '90{\circ} 2', '90{\circ} 3')
title('Docol 1400')
xlim([0,0.08])
ylim([0,1600])
supersizeme(f,1.5)

%Plot all together:
f=figure;
plot(e(:,1),s(:,1), 'k'); hold on;
plot(e(:,19),s(:,19), 'r')
plot(e(:,10),s(:,10), 'b')
for i=2:9
    plot(e(:,i),s(:,i), 'k'); hold on;
end
```

```matlab
for i=11:18
    plot(e(:,i),s(:,i), 'b'); hold on;
end

for i=20:27
    plot(e(:,i),s(:,i), 'r'); hold on;
end

xlabel('Engineering strain [-]')
ylabel('Stress [MPa]')
legend('D600', 'D1000', 'D1400')
title('All')
supersizeme(f,1.5)
%-------------------------------------------------------------------------
%Find measured E for Docol 600 45 deg nr 1 (4):
sig=s(:,4).*(1+e(:,4)); %true stress
eps=log(1+e(:,4)); %true strain
p=epsC-sig/Ec; %Remove elastic strain from plastic
p=p(22:end); %Only use plstic true strain
sigP=sig(22:end); %only use plastic true stress


%-------------------------------------------------------------------------
%Compare Voce fit:
x=[0:0.001:1.0];
%Voce fit A:
Qa=395.6;
ca=16.32;
sa=376.1;
Ta1=Qa*(1-exp(-ca*x));%first and only term of voce 1
va=sa+Ta1; %total Voce

%Voce fit I:
Qi1=355;
ci1=5;
Qi2=183;
ci2=39;
Qi3=60;
ci3=9;
si=354.4;
Ti1=Qi1*(1-exp(-ci1*x)); %first term
Ti2=Qi2*(1-exp(-ci2*x)); %second term
Ti3=Qi3*(1-exp(-ci3*x)); %third term
vi=si+Ti1+Ti2+Ti3; %total Voce
```

X

```matlab
%Goodness of fit after run with LS Dyna:
f=figure;
ax7=subplot(1,1,1);
plot(ax7,e(:,4),s(:,4)); hold on;
plot(ax7,eLSA,sLSA);
plot(ax7,eLSI,sLSI, 'm--');

xlabel(ax7,'Engineering strain [-]')
ylabel(ax7,'Engineering stress [MPa]');
title(ax7,'D600: Comparison LS dyna to experiment')
legend(ax7,'Experiment', 'A', 'I')
supersizeme(f,1.7)
```

Listing 4: Matlab code to post process material tests.

Pressure curves for perforated plates:

```
close all; clear all; clc;
importD6;
importD10;
importD14;
importRigid;

x1=t_D6_B1_25;
x2=t_D6_C1_25;
x3=t_D10_B1_25;
x4=t_D10_C1_25;
x5=t_D14_B1_25;
x6=t_D14_C1_25;
x7=t_R_25;
y1 = p2_D6_B1_25;
y2 = p2_D6_C1_25;
y3 = p2_D10_B1_25;
y4 = p2_D10_C1_25;
y5 = p2_D14_B1_25;
y6 = p2_D14_C1_25;
y7 = p8_R_25;

[x1,y1] = moveMean(x1,y1);
[x2,y2] = moveMean(x2,y2);
[x3,y3] = moveMean(x3,y3);
[x4,y4] = moveMean(x4,y4);
[x5,y5] = moveMean(x5,y5);
[x6,y6] = moveMean2(x6,y6);
[x7,y7] = moveMean(x7,y7);

x1 = x1+0.1;
x2 = x2-0.154;
x3 = x3-0.126;
x4 = x4+0.1;
x5 = x5+0.1;
x6 = x6-0.154;
x7 = x7+0.8342;

figure;
plot(x1,y1, 'linewidth', 1); hold on;
plot(x2,y2, 'linewidth', 1);
plot(x3,y3, 'linewidth', 1);
plot(x4,y4, 'linewidth', 1);
plot(x5,y5, 'linewidth', 1);
```

```matlab
plot(x6,y6, 'linewidth', 1);
plot(x7,y7, 'linewidth', 1);
legend('D6-B1-25','D6-C1-25','D10-B1-25','D10-C1-25','D14-B1-25','D14-C1-25','R-25',
'fontsize',8)


f=figure;
plot(x1,y1, x2, y2, 'linewidth', 1); hold on;
plot(x3,y3, x4, y4, 'linewidth', 1);
plot(x5,y5, x6, y6, 'linewidth', 1);
plot(x7,y7, 'linewidth', 1)
xlabel('Time [ms]'); ylabel('Pressure [MPa]');
set(gca, 'fontsize', 8, 'linewidth', 1);
ylim([0 10]);
xlim([-1 50]);

props.axes1.position = [0.1 0.15 0.7 0.8];
props.axes2.position = [0.3 0.54 0.15 0.28];
props.axes1.fontsize = 8;
props.axes2.fontsize = 5;
props.axes2.linewidth = 0.5;
props.xlabel = '';
props.ylabel = '';

[ax1 ax2] = popout(gcf, 1.1, 3, props);
legend('D6-B1-25','D6-C1-25','D10-B1-25','D10-C1-25','D14-B1-25','D14-C1-25','R-25',
'fontsize',8)
supersizeme(f,1.7)


x1_2=t_D6_B1_35;
x2_2=t_D6_C1_35;
x3_2=t_D10_B1_35;
x4_2=t_D10_C1_35;
x5_2=t_D14_B1_35;
x6_2=t_D14_C1_35;
x7_2=t_R_35(11420:end);

y1_2 = p2_D6_B1_35;
y2_2 = p2_D6_C1_35;
y3_2 = p2_D10_B1_35;
y4_2 = p2_D10_C1_35;
y5_2 = p2_D14_B1_35;
y6_2 = p2_D14_C1_35;
y7_2 = p8_R_35(11420:end);
```

```matlab
[x1_2,y1_2] = moveMean2(x1_2,y1_2);
[x2_2,y2_2] = moveMean(x2_2,y2_2);
[x3_2,y3_2] = moveMean(x3_2,y3_2);
[x4_2,y4_2] = moveMean(x4_2,y4_2);
[x5_2,y5_2] = moveMean(x5_2,y5_2);
[x6_2,y6_2] = moveMean(x6_2,y6_2);
[x7_2,y7_2] = moveMean2(x7_2,y7_2);


x1_2 = x1_2 -14.83;
x2_2 = x2_2 - 0.048;
x3_2 = x3_2 + 0.098;
x4_2 = x4_2 + 0.098;
x5_2 = x5_2 + 0.098;
x6_2 = x6_2 + 0.098;
x7_2 = x7_2 + 0.8983;


figure;
plot(x1_2,y1_2, 'linewidth', 1); hold on;
plot(x2_2,y2_2, 'linewidth', 1);
plot(x3_2,y3_2, 'linewidth', 1);
plot(x4_2,y4_2, 'linewidth', 1);
plot(x5_2,y5_2, 'linewidth', 1);
plot(x6_2,y6_2, 'linewidth', 1);
plot(x7_2,y7_2, 'linewidth', 1);
legend('D6-B1-35','D6-C1-35','D10-B1-35','D10-C1-35','D14-B1-35','D14-C1-35',
'Massive plate','fontsize',8)



f=figure;
plot(x1_2,y1_2, x2_2, y2_2, 'linewidth', 1); hold on;
plot(x3_2,y3_2, x4_2, y4_2, 'linewidth', 1);
plot(x5_2,y5_2, x6_2, y6_2, 'linewidth', 1);
plot(x7_2,y7_2, 'linewidth', 1)
xlabel('Time [ms]'); ylabel('Pressure [MPa]');
set(gca, 'fontsize', 8, 'linewidth', 1);
ylim([0 12]);
xlim([-1 50]);

props.axes1.position = [0.1 0.15 0.7 0.8];
props.axes2.position = [0.3 0.54 0.15 0.3];
props.axes1.fontsize = 8;
props.axes2.fontsize = 5;
props.axes2.linewidth = 0.5;
props.xlabel = '';
```

```
props.ylabel = '';

[ax1 ax2] = popout(gcf, 1, 3, props);
legend('D6-B1-35','D6-C1-35','D10-B1-35','D10-C1-35','D14-B1-35','D14-C1-35','R-35',
'fontsize',8)
supersizeme(f,1.7)
```

Listing 5: Matlab code to plot pressure curves for perforated plates.

Pressure curves for whole plates:

```
close all; clear all; clc;
importFull;
importRigid;
importD10;

x1=t_D10_D1_5;
x2=t_D10_D1_15;
x3=t_D10_D1_25;
x4=t_D10_D1_35;
x5=t_D10_D1_60;
x6=t_D10_B1_25;
x7=t_D10_C1_25;
x6_2=t_D10_B1_35;
x7_2=t_D10_C1_35;


x1_R=t_R_5;
x2_R=t_R_15;
x3_R=t_R_25;
x4_R=t_R_35(11420:end);
x5_R=t_R_60(7870:end);
x4_R2=t_R_35(11420:end);
x5_R2=t_R_60(7870:end);


y1 = p2_D10_D1_5;
y2 = p2_D10_D1_15;
y3 = p2_D10_D1_25;
y4 = p2_D10_D1_35;
y5 = p2_D10_D1_60;
y6 = p2_D10_B1_25;
y7 = p2_D10_C1_25;
y6_2 = p2_D10_B1_35;
y7_2 = p2_D10_C1_35;
```

```
y1_R = p8_R_5;
y2_R = p8_R_15;
y3_R = p8_R_25;
y4_R = p8_R_35(11420:end);
y5_R = p8_R_60(7870:end);
y4_R2 = p8_R_35(11420:end);
y5_R2 = p8_R_60(7870:end);


[x1,y1] = moveMean(x1,y1);
[x2,y2] = moveMean(x2,y2);
[x3,y3] = moveMean(x3,y3);
[x4,y4] = moveMean(x4,y4);
[x5,y5] = moveMean2(x5,y5);
[x6,y6] = moveMean(x6,y6);
[x7,y7] = moveMean(x7,y7);
[x6_2,y6_2] = moveMean(x6_2,y6_2);
[x7_2,y7_2] = moveMean(x7_2,y7_2);

[x1_R,y1_R] = moveMean(x1_R,y1_R);
[x2_R,y2_R] = moveMean(x2_R,y2_R);
[x3_R,y3_R] = moveMean(x3_R,y3_R);
[x4_R,y4_R] = moveMean2(x4_R,y4_R);
[x5_R,y5_R] = moveMean2(x5_R,y5_R);

x1_R = x1_R + 0.936;
x2_R = x2_R + 0.8625;
x3_R = x3_R + 0.8362;
x4_R = x4_R + 0.8983;
x5_R = x5_R - 4.402;
x4_R2 = x4_R2 - 1.2716;
x5_R2 = x5_R2 - 1.2716;
x1 = x1+0.092;
x2 = x2+0.092;
x3 = x3-0.112;
x4 = x4+0.092;
x5 = x5-15.108;

f = figure;
plot(x3,y3); hold on;
plot(x6,y6,x7,y7);
xlabel('Time [ms]'); ylabel('Pressure [MPa]');
ylim([0 10]);
```

```
xlim([-1 55]);
legend('D10-D1-25','D10-B1-25','D10-C1-25')
supersizeme(f,1.7)

f = figure;
plot(x4,y4); hold on;
plot(x6_2,y6_2,x7_2,y7_2);
xlabel('Time [ms]'); ylabel('Pressure [MPa]');
ylim([0 12]);
xlim([-1 55]);
legend('D10-D1-35','D10-B1-35','D10-C1-35')
supersizeme(f,1.7)

f=figure;
plot(x1,y1, 'linewidth', 1,'color',[0, 0.4470, 0.7410]); hold on;
plot(x2,y2, 'linewidth', 1,'color',[0.8500, 0.3250, 0.0980]);
plot(x3,y3, 'linewidth', 1,'color',[0.9290, 0.6940, 0.1250]);
plot(x4,y4, 'linewidth', 1,'color',[0.4940, 0.1840, 0.5560]);
plot(x5,y5, 'linewidth', 1,'color',       [0.4660, 0.6740, 0.1880]);
plot(x1_R,y1_R, 'linewidth', 0.5,'color',[0, 0.4470, 0.7410],'LineStyle','-.');
plot(x2_R,y2_R, 'linewidth', 0.5,'color',[0.8500, 0.3250, 0.0980],'LineStyle','-.');
plot(x3_R,y3_R, 'linewidth', 0.5,'color',[0.9290, 0.6940, 0.1250],'LineStyle','-.');
plot(x4_R,y4_R, 'linewidth', 0.5,'color',[0.4940, 0.1840, 0.5560],'LineStyle','-.');
plot(x5_R,y5_R, 'linewidth', 0.5,'color',[0.4660, 0.6740, 0.1880],'LineStyle','-.');
xlabel('Time [ms]'); ylabel('Pressure [MPa]');
set(gca, 'fontsize', 8, 'linewidth', 1);
ylim([0 15]);
xlim([-1 55]);

props.axes1.position = [0.1 0.15 0.7 0.8];
props.axes2.position = [0.4 0.65 0.1 0.24];
props.axes1.fontsize = 8;
props.axes2.fontsize = 5;
props.axes2.linewidth = 0.5;
props.xlabel = '';
props.ylabel = '';

[ax1 ax2] = popout(gcf, 0.8, 2.5, props);
legend('D10-D1-05','D10-D1-15','D10-D1-25','D10-D1-35','D10-D1-60','fontsize',8)
supersizeme(f,1.7)
```

Listing 6: Matlab code to plot pressure curves for whole plates.

Popout function for zooming[57]:

```matlab
function [ax1 ax2] = popout(h, xmin, xmax, extraprops)
% POPOUT create popout plot
%   [ax1 ax2] = popout(h, xmin, xmax)
%       creates a popout plot (e.g. outset plot) from axis contained in the
%       figure specfied by handle h, from limits specified by xmin and xmax.
%
%   [ax1 ax2] = popout(h, xmin, xmax, props)
%       creates a popout plot (e.g. outset plot) from axis contained in the
%       figure specfied by handle h, from limits specified by xmin and xmax
%       with axes properties specified by the structure props (see example below).
%
%       popout plot inherits all graphics properties of the axis in figure h
%       (e.g. linewidth, labels).
%
%       However, extra axes properties (for each axis) may be specfied to override
%       inherited properties, such as:
%
%       props.axes1.position = [0.1 0.15 0.7 0.8];
%       props.axes2.position = [0.5 0.1 0.4 0.6];
%       props.axes2.fontsize = 20;
%
%       Any valid axis property (fontsize, xtick, yticklabel, etc...) may be
%       provided for each axis.
%
%
%   example:
%
%       x=0:0.1:100;
%       y = bessel(1,x);
%       plot(x,y);
%       popout(gcf, 10, 20);
%
%   more complex popout plot example (with axes properties):
%
%       x=0:0.1:100;
%       y1 = bessel(1,x);
%       y2 = bessel(1,x)*2;
%
%       plot(x,y1, x, y2, 'linewidth', 2); grid on;
%       xlabel('time'); ylabel('amplitude');
%       title('Bessel functions');
%       set(gca, 'fontsize', 12, 'linewidth', 2);
%       ylim([-10 2]);
%
```

```matlab
%        props.axes1.position = [0.1 0.15 0.7 0.8];
%        props.axes2.position = [0.5 0.1 0.4 0.6];
%        props.axes1.fontsize = 10;
%        props.axes2.fontsize = 18;
%        props.axes2.linewidth = 2;
%        props.xlabel = 'poput x-label';
%        props.ylabel = 'poput y-label';
%
%        [ax1 ax2] = popout(gcf, 10, 20, props);
%
%
%        Copyright 2011, Simon Henin <shenin@gc.cuny.edu>
if nargin < 4,
    extraprops.axes1.position = [0.1 0.15 0.7 0.8];
    extraprops.axes2.position = [0.3 0.1 0.6 0.55];
end
type = get(h, 'Type');
if strcmp(type, 'figure'),
    ax1 = get(h, 'children');
else
    ax1 = h;
end
padding = 10;
ax2 = copyobj(ax1, h);
set(ax2, 'position', extraprops.axes2.position);
children = get(ax1, 'children');
ylimit = get(ax1, 'Ylim');
set(ax1, 'position',extraprops.axes1.position);
ylim([ylimit(1)+ylimit(1)*(padding/100) ylimit(2)+ylimit(2)*(padding/100)]);
ymax = 0;
ymin = 0;
for i=1:length(children),
    xd = get(children(i), 'xdata');
    index = find(xd >= xmin & xd <= xmax);
    yd =  get(children(i), 'ydata');
    ymax = max(ymax, max(yd(index)));
    ymin = min(ymin, min(yd(index)));
end
axes(ax1);
ymin = 6.5;
rectangle('Position',[xmin,ymin,xmax-xmin,ymax-ymin], 'linewidth', 0.5);
axes(ax2);
title('');
xlim([xmin xmax]);
ylim([ymin ymax]);
```

```matlab
% add special pop-out properties
if isfield(extraprops, 'xlabel'),
    xlabel(extraprops.xlabel);
end
if isfield(extraprops, 'ylabel'),
    ylabel(extraprops.ylabel);
end
% add axes properties
fields = fieldnames(extraprops.axes1);
for i=1:length(fields),
    set(ax1, fields{i}, getfield(extraprops.axes1, fields{i}));
end
fields = fieldnames(extraprops.axes2);
for i=1:length(fields),
    set(ax2, fields{i}, getfield(extraprops.axes2, fields{i}));
end
% add pop-out lines
[xf1 yf1] = popout_getcoords(ax1, xmin, ymin);
[xf2 yf2] = popout_getcoords(ax2, xmin, ymin);
annotation('line',[xf1 xf2],[yf1 yf2]);
% [xf1 yf1] = popout_getcoords(ax1, xmin, ymax);
% [xf2 yf2] = popout_getcoords(ax2, xmin, ymax);
% annotation('line',[xf1 xf2],[yf1 yf2]);
% [xf1 yf1] = popout_getcoords(ax1, xmax, ymin);
% [xf2 yf2] = popout_getcoords(ax2, xmax, ymin);
% annotation('line',[xf1 xf2],[yf1 yf2]);
% [xf1 yf1] = popout_getcoords(ax1, xmax, ymax);
% [xf2 yf2] = popout_getcoords(ax2, xmax, ymax);
% annotation('line',[xf1 xf2],[yf1 yf2]);
axes(ax2);
function [x y] = popout_getcoords(ax, x, y)
%% Get limits
axun = get(ax,'Units');
set(ax,'Units','normalized');
axpos = get(ax,'Position');
axlim = axis(ax);
axwidth = diff(axlim(1:2));
axheight = diff(axlim(3:4));
x = (x-axlim(1))*axpos(3)/axwidth + axpos(1);
y = (y-axlim(3))*axpos(4)/axheight + axpos(2);
%% Restore axes units
set(ax,'Units',axun)
```

Listing 7: Matlab code for function to zoom in on pressure curves.

Moving mean function to filter data:

```matlab
function [t,p] = moveMean(t_in,p_in)
TF = ischange(p_in);
a = find(TF == 1, 1);
p = zeros();

for i = 1:length(p_in)
    p(i) = p_in(i);
    if i > a
        if p_in(i) <= 0.001
            break;
        end
    end
end

p = movmean(p, 70);
t = linspace(0-t_in(a), t_in(i)-t_in(a), length(p));
end
```
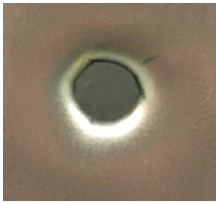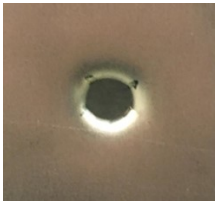
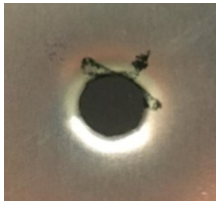**Listing 8:** Matlab code for function filter pressure curve data.

C   Pictures of Plates After Ballistic Impact

(a) D600-1 front

(b) D600-2 front

(c) D600-3 front

(d) D600-1 back

(e) D600-2 back

(f) D600-3 back

(g) D600-1 back

(h) D600-2 back

(i) D600-3 back

Figure .1: Resulting fractures of the D600 plates after ballistic impact.

(a) D1000-1 front

(b) D1000-2 front

(c) D1000-3 front

(d) D1000-1 back

(e) D1000-2 back

(f) D1000-3 back

(g) D1000-1 back

(h) D1000-2 back

(i) D1000-3 back
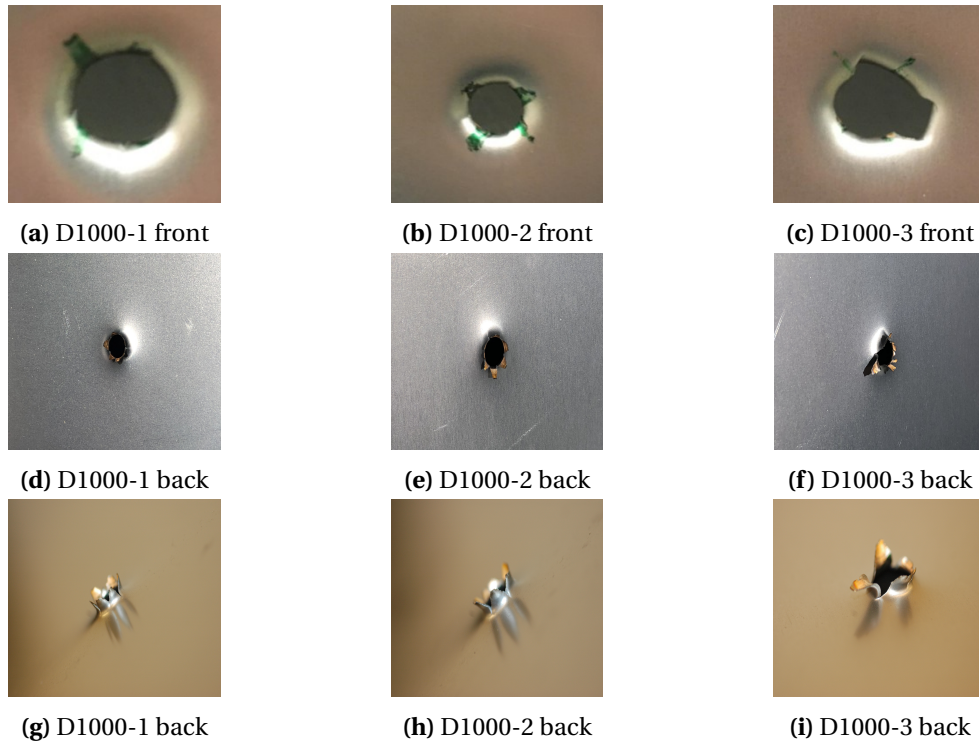
Figure .2: Resulting fractures of the D1000 plates after ballistic impact.

(a) D1400-1 front

(b) D1400-2 front

(c) D1400-3 front

(d) D1400-1 back

(e) D1400-2 back

(f) D1400-3 back

(g) D1400-1 back

(h) D1400-2 back

(i) D1400-3 back
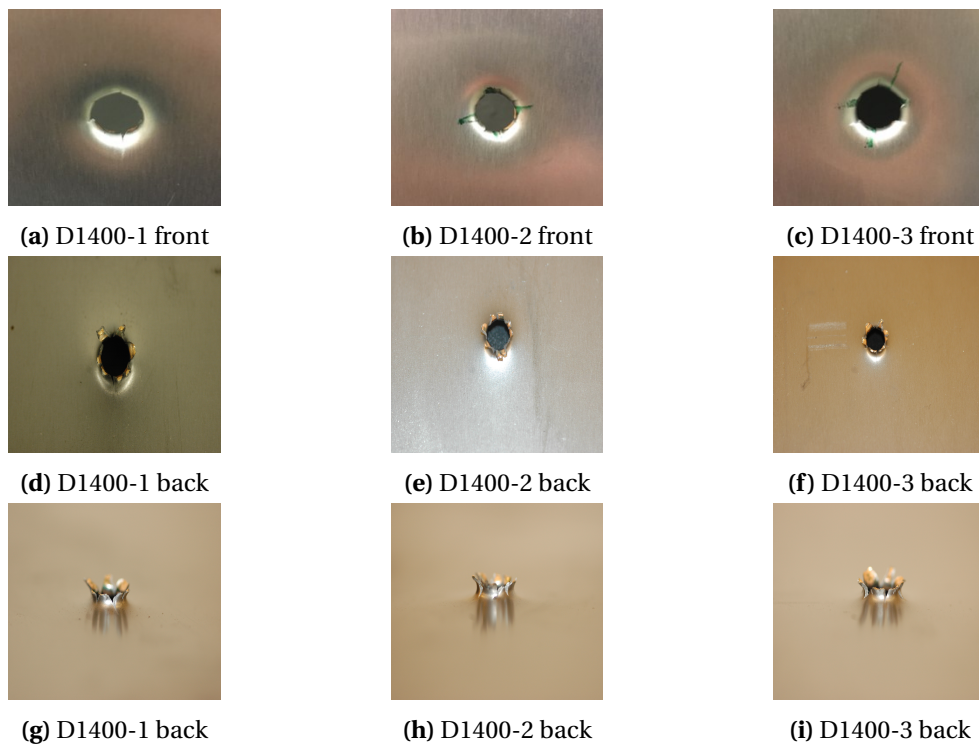
Figure .3: Resulting fractures of the D1400 plates after ballistic impact.

D   Energy in LS-DYNA

To ensure the nonlinear dynamic analyses do not add excessive artificial energies, the energy data is collected along with the energy ratios. The energy ratio is defined in the following equation.

$$ER = \frac{E_{total}}{E_{total}^0 + W_{ext}},\tag{1}$$

where W_{ext} is the external energy, E_{total}^0 is the total energy at the beginning of the analysis, and E_{total} is the total energy at a given time in the analysis. The total energy is a summation of all energies in the analysis. So that

$$E_{total} = E_{kin} + E_{int} + E_{si} + E_{rw} + E_{damp} + E_{hg},\tag{2}$$

which is respectively the kinetic energy, internal energy, sliding interface energy, rigid wall energy, damping energy and hourglass energy. The energies can be seen in figure .4. The energies are on the left axis and the energy ratios on the right.

(a) D6_B1_ballistic

(b) D6_B1_35

(c) D6_C1_35

(d) D10_D1_35
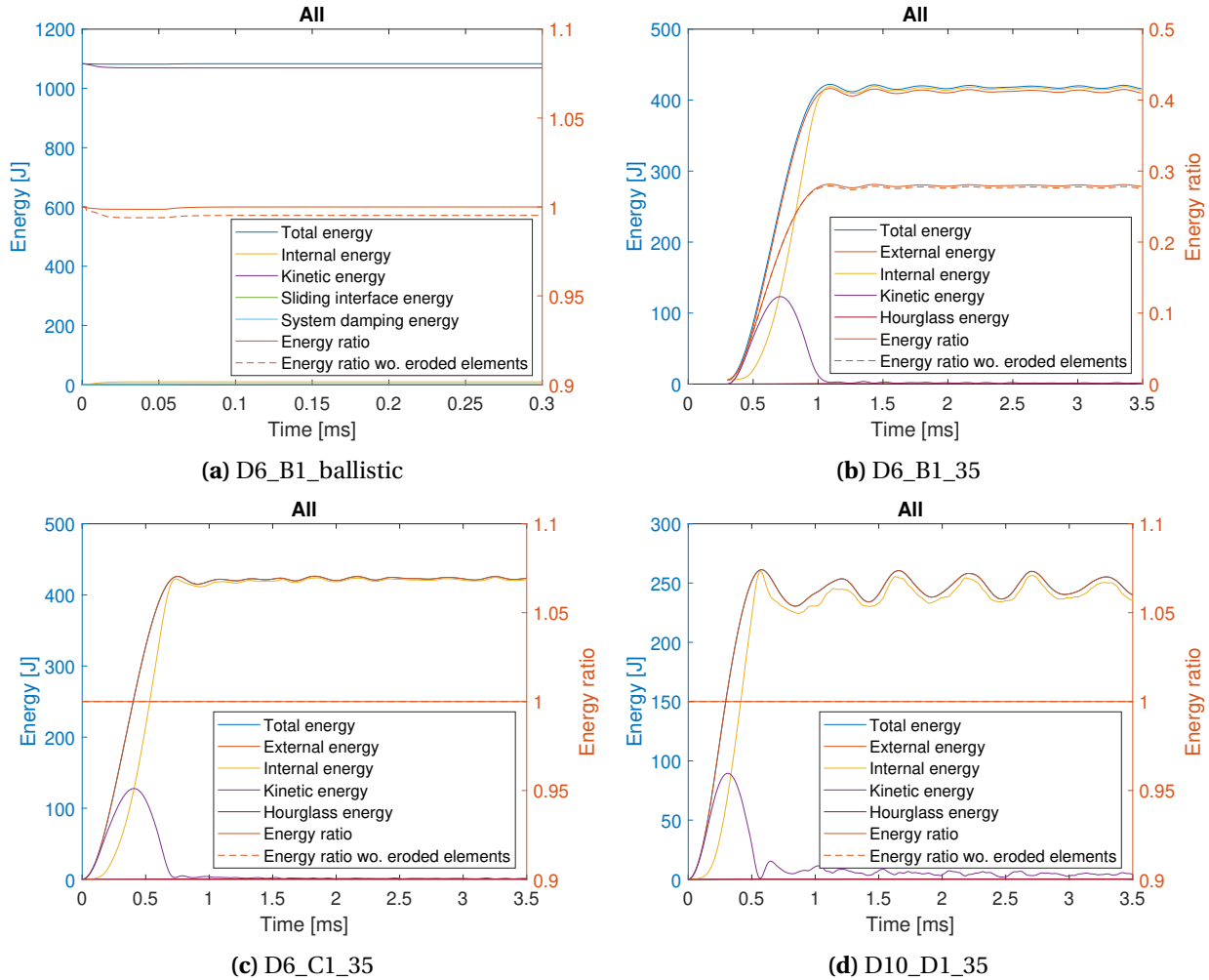
Figure .4: All energy data from LS DYNA for 4 representative simulations.

It is evident that all energy ratios are within a margin of 1 ± 0.1, where an energy ratio of 1, would be prefect. The exception is the blast loading of the combined loading seen in figure .4b. The reason the energy ratio deviates from the acceptable values, is that LS DYNA includes the final energy of the ballistic analysis seen in figure .4a in the initial energy of the blast analysis after the restart. This means that the eg. the velocity of the bullet is included in the initial energy of the blast analysis. As a result the energy ratio is calculated as

$$ER = \frac{E_{int} + E_{kin} + E_{hg}}{E_{int}^0 + E_{kin}^0 + W_{ext} + E_{tot}^{bullet}} = 0.280 \tag{3}$$

The correct calculation is

$$ER = \frac{E_{int} + E_{kin} + E_{hg}}{E_{int}^0 + E_{kin}^0 + W_{ext}} = 0.999, \tag{4}$$

which is satisfactory and well within 1 ± 0.1. Lastly, the damping energy in the ballistic simulation is shown to be less than 1 % of the total and kinetic energy. To highlight the differences of the energies, they are plotted in figure.5, where they are differentiated into high and low energies.
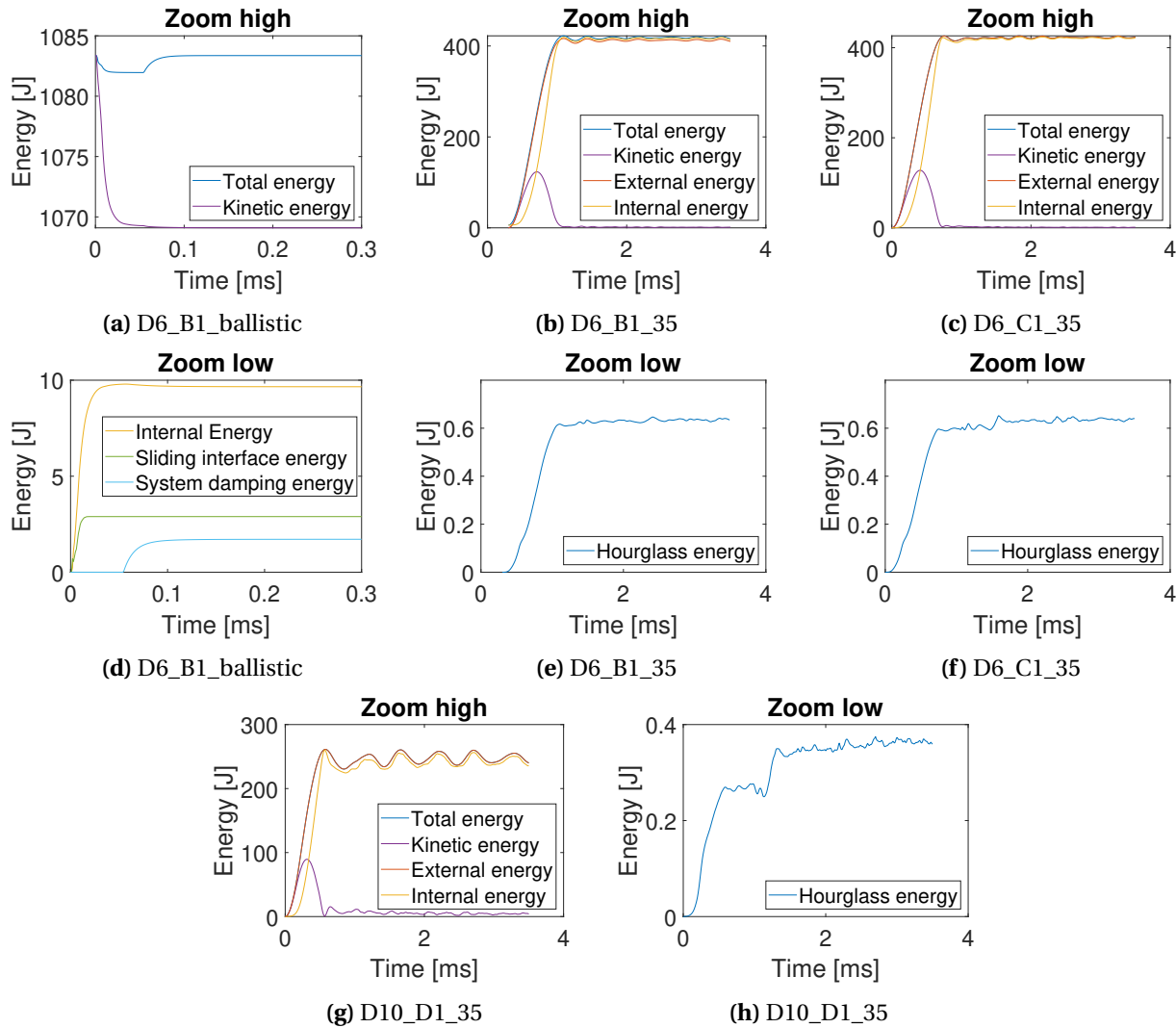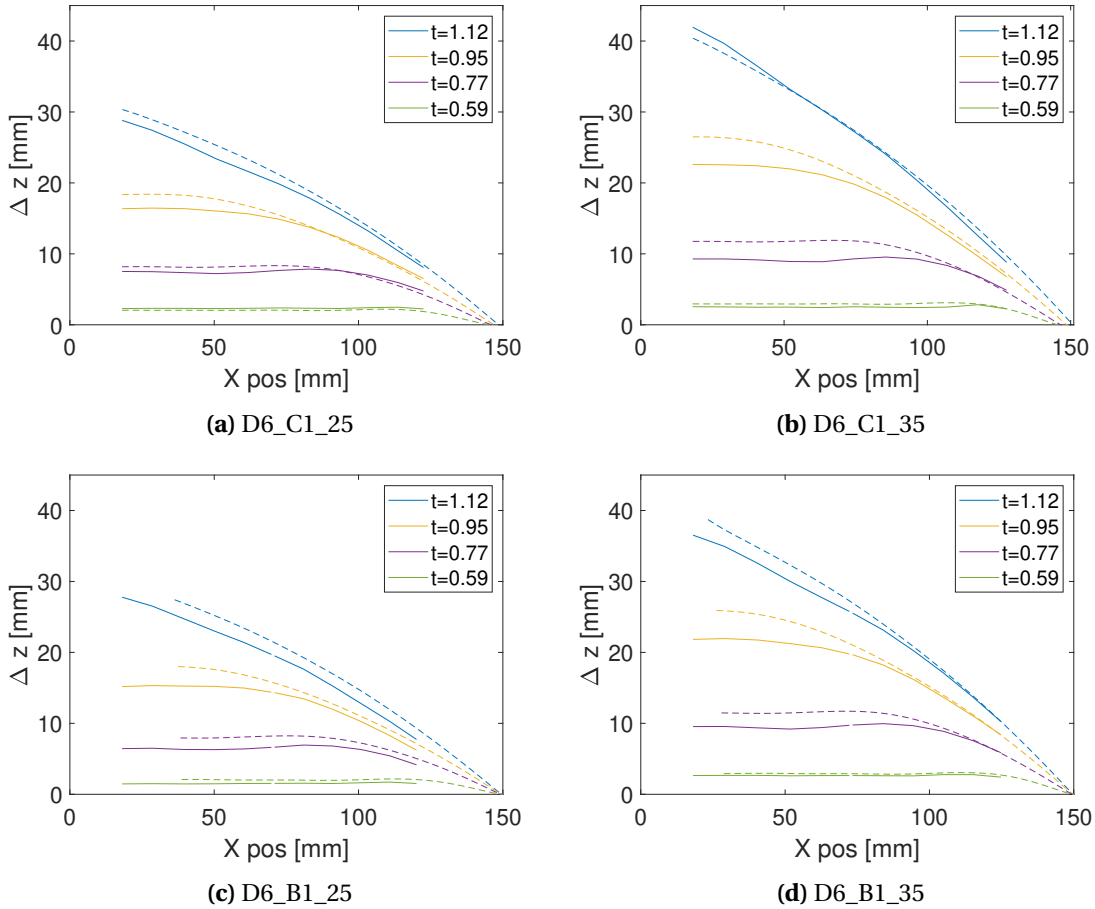

Figure .5: Zoom of all energies from figure .4.

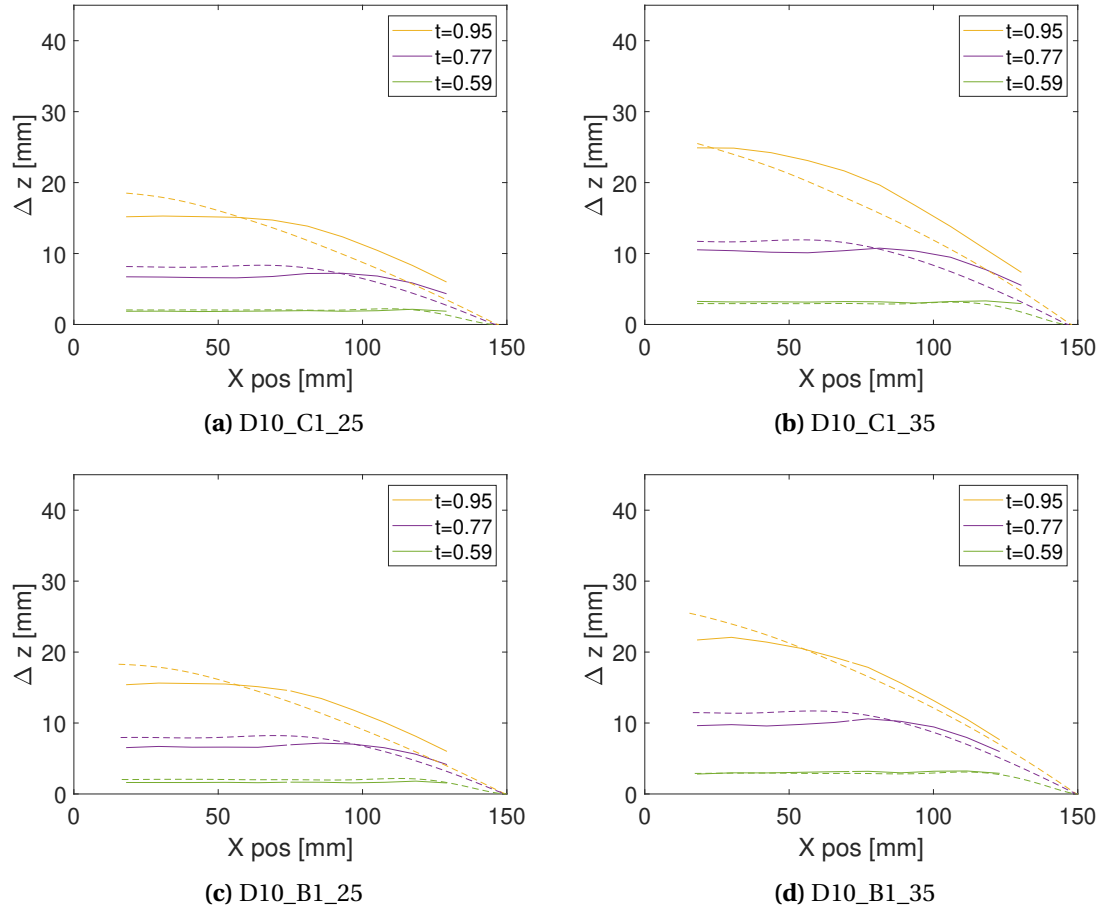# E   Comparison of Numerical and Experimental Deformation Profiles

The deformation profiles from the simulations are plotted against the ones obtained from DIC in figures .6, .7 and .8.

(a) D6_C1_25

(b) D6_C1_35

(c) D6_B1_25

(d) D6_B1_35

Figure .6: Comparison of D600 profiles. The dashed lines are the numerical results, and the continuous lines are the experimental results.

For the D600 configurations the simulated deflection behaviour of the plates gives a good approximation of the experimental data. The simulations in general yield slightly higher deformations than in the experiments for all time frames.

(a) D10_C1_25

(b) D10_C1_35

(c) D10_B1_25

(d) D10_B1_35

Figure .7: Comparison of D1000 profiles. The dashed lines are the numerical results, and the continuous lines are the experimental results.

In the deformation profile plots for D1000 the last time frame is left out as the B configurations experienced fracture that might influence the results. As mentioned in section 5.3.3 the simulations yielded lower maximum deflections than that obtained from DIC, and for the last time frame the C configuration plates had already experienced elastic rebound. This is consistent with the numerical results for the whole plates. For the three time frames presented the deformations are similar, however slightly higher for the simulated plate response.
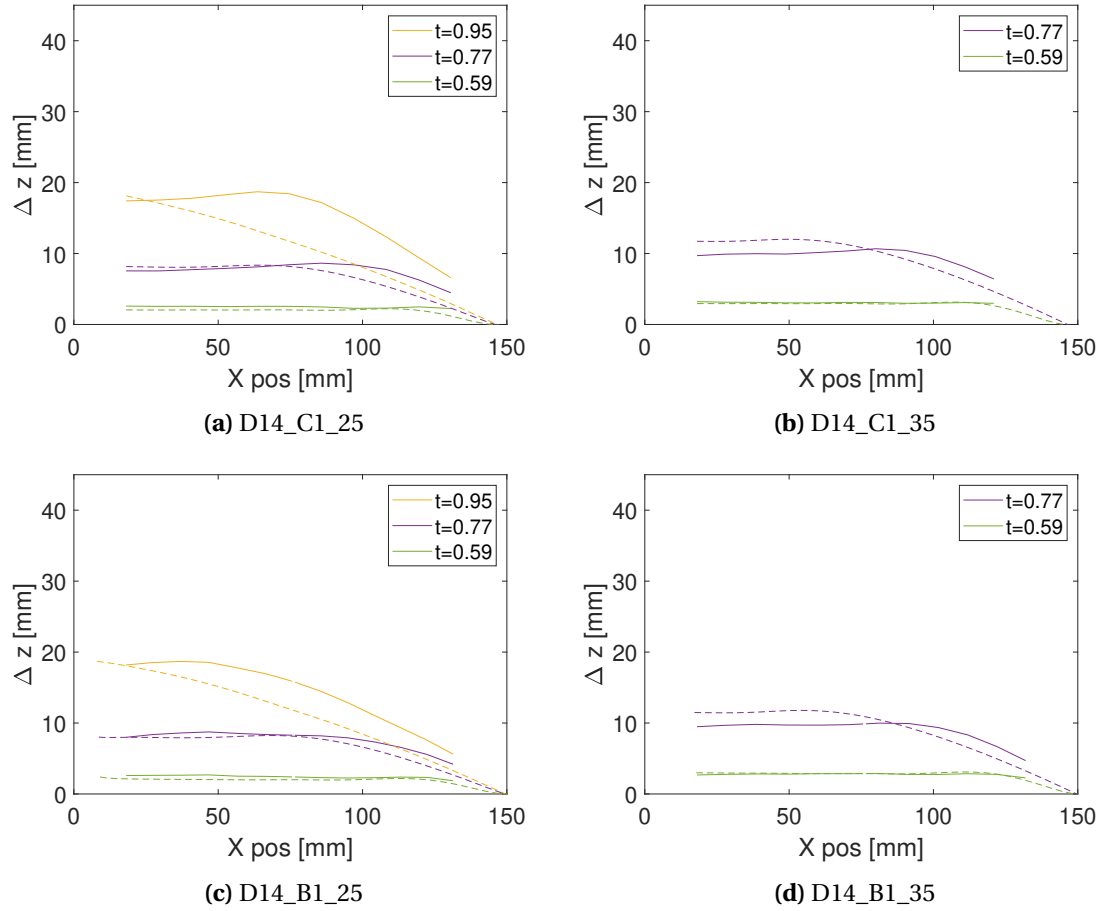
Figure .8: Comparison of D1400 profiles. The dashed lines are the numerical results, and the continuous lines are the experimental results.

All the simulations on D1400 plates lead to total failure.

F   Removal of Points in Point Cloud

Figure .9 shows which points are removed from the point clouds during post-processing using the code in listing 2. Figure .9a shows the point cloud before it is post-processed, and figure .9b shows the result after post processing. All dimensions in the point clouds are in mm.
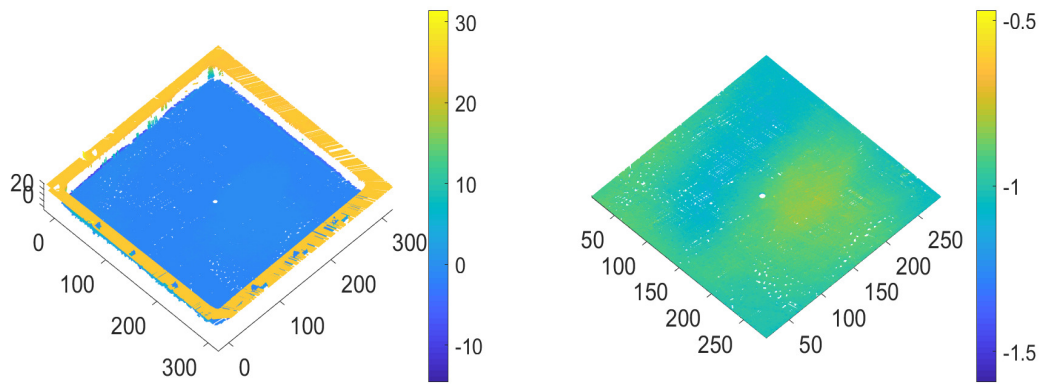
(a) The point cloud before points are removed.

(b) The point cloud after points are removed. The colour map shows out-of-plane position in mm.

Figure .9: Removal of unnecessary points for the D10_C1_25 before it is subjected to blast load. All measurements are in mm.

Anja Murud Gahre & Ragnhild Hembre Haug

Dynamic response of steel plates subjected to combined blast and impact loading

NTNU
Norwegian University of
Science and Technology